Imaging and Switching Individual Nanomagnets with Spin-Polarized Scanning Field Emission Microscopy

Dissertation
zur Erlangung des Doktorgrades
am Department Physik
der Universität Hamburg

vorgelegt von
Dipl.-Phys. Anika Schlenhoff
aus Freiburg im Breisgau

Hamburg
2013

Gutachter der Dissertation:
Prof. Dr. R. Wiesendanger
Prof. Dr. R. L. Johnson
Prof. Dr. H. Brune

Gutachter der Disputation:
Prof. Dr. R. Wiesendanger
Prof. Dr. H. P. Oepen

Datum der Disputation:
16.10.2013

Vorsitzender des Prüfungsausschusses:
Dr. M. Martins

Vorsitzender des Promotionsausschusses:
Prof. Dr. P. Hauschildt

Dekan der MIN-Fakultät:
Prof. Dr. H. Graener

Abstract

Electrons can be ripped out of a solid by a high electric field, thereby generating an emission current, which is spin-polarized when using a magnetic emitter. Although field emission is routinely used for microscopy purposes, the question remained open how it affects magnetism on the local scale. In this thesis, a novel spin-sensitive local probe technique called *spin-polarized scanning field emission microscopy* (SP-SFEM) is described that reveals the microscopic details of the interaction between spin-polarized field-emitted electrons and atomic-scale magnets.

Antiferromagnetic field emitter tips made of bulk Cr are used. They are characterized on the well-known system of the combined Fe mono- and double layer on W(110) by spin-polarized scanning tunneling microscopy and spectroscopy at variable temperature. The experiments reveal that these tips are typically sensitive to all the in-plane and out-of-plane components of surface magnetism over a wide bias voltage and temperature range.

By approaching a biased Cr tip to a surface down to nm distance in vacuo, a very local injection of field-emitted electrons is achieved, and scanning allows for magnetic imaging by spin-polarized field emission conductance measurements. Using this technique I investigate nanomagnets consisting of only about 50 Fe atoms on a W(110) substrate. Detailed lifetime analyses of their thermally-activated magnetization switching as a function of emission current display that spin-polarized field emission generates considerable Joule heating and spin-transfer torque in the nanomagnet. Comparative analyses with hot field-emitted and low-energy tunneling electrons reveal significant differences in the respective microscopic processes involved in heat dissipation and spin-transfer torque. A trend of higher spin-transfer torque switching efficiency per electron with increasing current is observed for field emission, presumably due to the emergence of Stoner excitations, that are inaccessible for low-energy tunneling electrons. On a quasistable nanomagnet, a spin-polarized emission current of a few nA already triggers magnetization reversal, thereby confirming the high impact of field-emitted spins on magnetism at the local scale.

This work demonstrates the capability of SP-SFEM for magnetic imaging and controlled magnetization switching on the atomic scale at nm distances.

Zusammenfassung

Wird ein hohes elektrisches Feld an eine scharfe Magnetnadel angelegt, so lösen sich Elektronen heraus, die einen spin-polarisierten Strom erzeugen. Obwohl feld-emittierte Elektronen in vielen Abbildungsmethoden routinemäßig zum Einsatz kommen, blieben ihre mikroskopischen Wechselwirkungen mit einem magnetischen Festkörper im Detail bislang ungeklärt. In dieser Arbeit wird eine neue ortsauflösende und magnetisch empfindliche Abbildungs- und Untersuchungsmethode beschrieben, die *spin-polarisierte Rasterfeldemissionsmikroskopie* genannt wird. Sie erlaubt einen detaillierten Einblick in die fundamentalen Wechselwirkungsprozesse eines Feldemissionsstromes mit einem Magneten auf atomarer Skala.

Als spin-polarisierte Elektronenquelle dient hierbei erstmals ein Emitter aus einem antiferromagnetischen Material, nämlich Cr. Diese Voll-Cr-Spitzen werden zunächst auf dem wohlverstandenen Materialsystem der kombinierten Fe-Mono- und -Doppellage auf W(110) mittels spin-polarisierter Rastertunnelmikroskopie und -spektroskopie bei variabler Temperatur charakterisiert. Es wird gezeigt, dass sie typischerweise auf alle Magnetisierungsrichtungen im Raum empfindlich sind, sowohl über einen großen Spannungs- als auch über einen großen Temperaturbereich.

Wird eine Cr-Spitze bei angelegter Spannung bis auf einen Abstand von einigen Nanometern an eine Oberfläche im Vakuum angenähert, so werden feld-emittierte Elektronen sehr lokal injiziert, und das kontaklose Führen der Spitze über die Oberfläche erlaubt ein magnetisches Abbilden über ortsaufgelöste Messungen der spin-abhängigen Leitfähigkeit. Es werden einzelne Nanomagnete untersucht, die nur aus etwa 50 Fe-Atomen auf einem W(110)-Substrat bestehen und thermisch aktiviert zwischen zwei magnetischen Orientierungen schalten. Die Analyse ihrer stromabhängigen Lebensdauern offenbart ein beträchtliches Joule'sches Aufheizen des Nanomagneten durch den Feldemissionsstrom, sowie ein Spinstromschalten durch den Spinübertrag der feld-emittierten Elektronen. Vergleichende Analysen der Lebensdauern unter dem Einfluss von niederenergetischen tunnelnden bzw. höherenergetischen feld-emittierten Elektronen decken fundamentale Unterschiede in den jeweiligen zugrundeliegenden mikroskopischen Prozessen auf. Dabei wird eine immer höhere Schalteffizienz pro Elektron durch Spinübertrag mit zunehmendem Feldemissionsstrom beobachtet, was sich durch die Ausbildung von Stoner-Anregungen erklären lässt, die für tunnelnde Elektronen unzugänglich sind. Ein quasistabiler Nanomagnet kann bereits mit einem Feldemissionsstrom von einigen nA zur Magnetisierungsumkehr gezwungen werden, wodurch der immense Einfluss feld-emittierter Elektronen-Spins auf den lokalen Magnetismus veranschaulicht wird.

Die vorliegende Arbeit demonstriert das Potential der spin-polarisierten Rasterfeldemissionsmikroskopie bezüglich des Abbildens und gezielten Manipulierens von Magnetismus auf atomarer Skala und in Abständen von einigen Nanometern.

Contents

Chapter 1

Introduction

As device technology like cameras, cell phones or tablet computers becomes ever-present in everyday life, the demand for ever smaller, more efficient electronics becomes critical. So-called spin-electronic devices, that are no longer based on the charge of the electric current but on the electron *spin* magnetic moment, provide an outlet for meeting these future technological demands. They can considerably increase the capacity of hard disks, enable small mobile devices and permit nonvolatile data storage. Still, the research field of spin-electronics is in its infancy, promising unique future applications and functionalities [1].

Nonequilibrium hot-electron spins interacting with magnetic solids play a key role in numerous spin-electronic applications [2–4]. They govern spin-dependent transport through spin-valve systems and magneto-tunnel junctions, resulting in the phenomena of giant [5] and tunneling magnetoresistance [6] (cf. Fig. 1.1(a)). In addition, hot-electron spins trigger ultrafast demagnetization in optical pump-

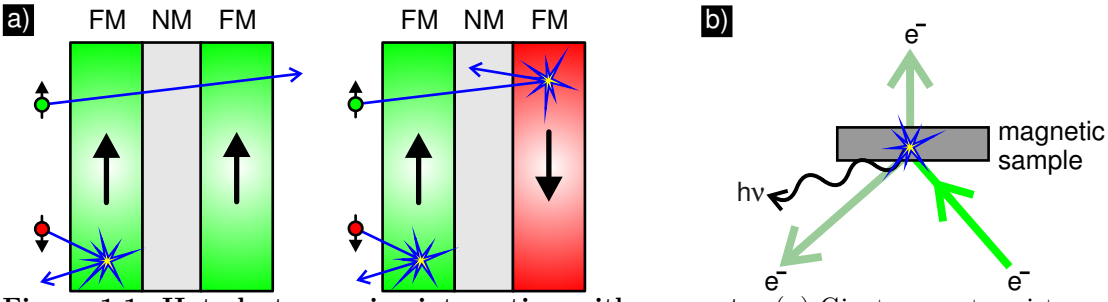

Figure 1.1: Hot-electron spins interacting with magnets. (**a**) Giant magnetoresistance effect: The conductance of a device consisting of two magnetic layers (FM) separated by a non-magnetic layer (NM) is higher for the parallel (left) than for the antiparallel (right) alignment of the magnetic layers, since electrons with a spin parallel to the layer magnetization pass through whereas electrons with an antiparallel spin are scattered. (**b**) In various spin-polarized electron spectroscopy and magnetic imaging techniques the transmittance, reflectance or interaction (e.g. by analyzing emitted photons hν) of a spin-polarized hot-electron beam (e^-) focused onto a magnetic sample is used.

probe experiments [7–10] and all-optical magnetic switching [11]. Several spin-polarized electron spectroscopy and magnetic imaging techniques are based on hot-electron spins [12–14], see Fig. 1.1(b). The basic behavior is governed by the interplay of hot-electron spins with the various degrees of freedom in a magnetic solid, including e.g. electrons, phonons or spin waves. Thus, a detailed understanding of these interactions is essential for a correct interpretation of many hot electron spin phenomena and characterization techniques, as well as for future spin-electronic devices and data storage technologies.

Time-resolved two-photon photoemission experiments have provided insight into the interaction of hot electrons with an underlying spin system by optically exciting electrons into image-potential states (IPS) creating electron-hole pairs that subsequently recombine [15, 16], as shown schematically in Fig. 1.2(a). However, since this technique averages laterally, it is not suitable for studying individual atomic-scale magnets. Another exciting question is how a spin system is affected by pumping IPS with spin-polarized hot electrons from an *external* source (cf. Fig. 1.2(b)).

Field emission from an atomically sharp needle can be used as a point-like source of hot electrons [17, 18]. Electrons are ripped out of the solid by the high electric field, thereby generating an emission current [19], which is spin-polarized when using a magnetic emitter [20, 21].

By approaching a needle to nm distances from a sample surface it is possible to achieve a very local injection of these hot electrons. Applying a bias voltage slightly higher than the work function of the sample results in the resonant injection of field-emitted electrons into the IPS at the sample. Being confined in the region between the bulk surface potential and the image potential on the vacuum

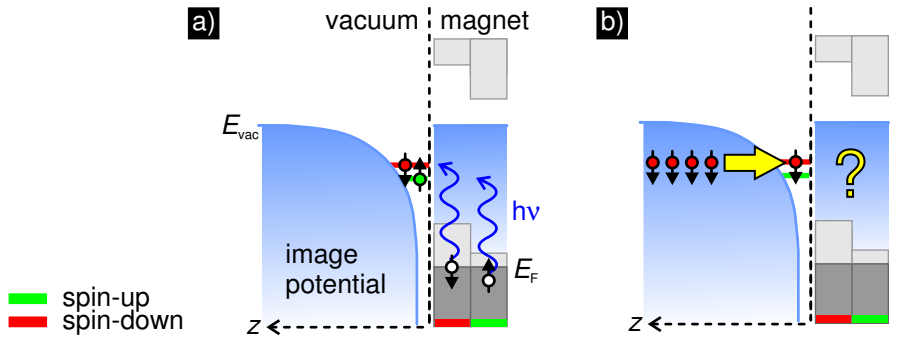

Figure 1.2: Hot-electron spins in image-potential states (IPS). IPS are empty states with energies close to the vacuum energy E_{vac} confined in the region between the bulk surface potential and the image potential on the vacuum side. (**a**) By optically exciting electrons from energies close to the Fermi energy E_{F} of the magnet into IPS in photoemission experiments, electron-hole pairs are created. (**b**) It is an open question how an atomic-scale magnet is affected by pumping its IPS with spin-polarized hot electrons from an external source.

side, the IPS experience a Stark shift due to the applied electric field between the tip and the sample and transform into field-emission resonance (FER) states [22].

It has been shown recently that magnetic imaging on a local scale is possible by exploiting the exchange splitting of the FER states on magnetic surfaces using a *spin-polarized scanning tunneling microscopy* (SP-STM) setup [23]. The spin-polarized emission conductance mediated by the exchange-split FER states depends on the relative orientation between the tip and the sample magnetization. Hence, raster-scanning a biased probe tip with a fixed magnetization over a surface with spatially varying magnetization results in a conductance that varies with the sample magnetization. This can be used to generate a magnetic map of the surface. This magnetic imaging technique will be called *spin-polarized scanning field emission microscopy* (SP-SFEM) in this thesis. It is based on the same imaging principle used in SP-STM, where the spatially varying spin-polarized conductance is also detected. The only difference is that hot field-emitted electrons are used instead of low-energy tunneling electrons.

The authors of Ref. [23] were the first to combine the advantages of an SP-STM setup for precise positioning of the probe tip and high lateral resolution with a spin-polarized field-emitter at increased tip-sample distance. In their initial SP-SFEM study the magnetic vortex structure of a *bulk-like* Fe surface was imaged. The question arises whether magnetic structures down to single atomic layers can be imaged by SP-SFEM. The evolution of the FER states above the sample in vacuo is purely a surface effect, and the exchange splitting is determined solely by the spin-dependent reflectivity of the surface [24, 25]. Hence, it should not matter, how thick the underlying magnetic material is.

Moreover, since these spin-polarized field-emitted electrons penetrate the magnetic surface at relatively high energies, the question arises whether it is possible to detect inelastic interactions of spin-polarized field-emitted electrons with magnets by SP-SFEM.

A fundamental requirement for SP-SFEM and SP-STM experiments is a magnetic probe tip generating a spin-polarized current. Although SP-STM is a well-established technique, finding suitable magnetic probe tips is an important task since they have to fulfill so many needs. The ideal probe tip exhibits a stable electronic and magnetic configuration being magnetically sensitive over wide bias voltage and temperature ranges. With such tips spatially-resolved magnetic maps, spin-polarized spectroscopy studies, and the study of temperature-dependent magnetic phenomena become possible. For practical reasons, a magnetic probe tip which does not need a preparation procedure under ultra-high vacuum conditions would be favorable. The ultimate goal would be a tip which always remains magnetically sensitive.

Commonly used magnetic probe tips for SP-STM do not fulfill these requirements. They are usually fabricated by coating a thin magnetic film on a non-magnetic tip and have to be prepared and inserted into the microscope under

ultra-high vacuum. A dedicated tip exchange mechanism is required in the microscope. Hence, recent efforts focus on the usability of tips made of a bulk magnetic material [26–30].

Since a magnetic probe tip should not interact with the magnetic sample under investigation, a tip magnetic stray field is unwanted, therefore, antiferromagnetic materials are preferred. Based on these requirements, chromium (Cr) which is antiferromagnetic at temperatures below $T_N = 311\,\mathrm{K}$ [31] seems to be a promising bulk tip material for SP-STM experiments.

Though spin-polarized field emission from ferromagnetic emitters is known since the 1960's [20], an electron spin-polarization in field emission from an *antiferromagnetic* emitter has not been reported yet. The question arises whether an antiferromagnetic probe tip like a bulk Cr tip can be used for spin-polarized field emission conductance measurements in SP-SFEM.

In this thesis, the fundamentals of SP-STM and SP-SFEM are introduced in Chapter 2 and Chapter 3, respectively. The experimental setup as well as the preparation of conventional Cr-coated W-tips and the W(110) substrate are described in Chapter 4. The morphology and magnetic properties of Fe/W(110) at low coverages are summarized in Chapter 5. After a short description of the preparation of bulk Cr tips in Chapter 6, the spatial magnetic characterization on the system of 1.5 ML of Fe/W(110) by SP-STM is described. In Chapter 7 the bulk Cr tips are used in SP-SFEM experiments performed on magnets consisting of only about 50 iron atoms on a W(110) surface. After studying the FER states above these nanomagnets and testing the imaging capabilities of SP-SFEM on these nanomagnets, the experiments focus on the interaction of individual thermally switching nanomagnets with hot spin-polarized field-emitted electrons in comparison to spin-polarized low-energy tunneling electrons. Finally, the effects of hot spin-polarized field-emitted electrons on thermally-stable nanomagnets are investigated, thereby also testing the capabilities of SP-SFEM for controlled magnetization switching. The experimental findings are summarized in Chapter 8.

Chapter 2

Spin-Polarized Scanning Tunneling Microscopy (SP-STM)

In scanning tunneling microscopy (STM), a biased, atomically sharp tip is piezoelectrically approached to a few Å from a surface until a tunnel current flows. This tunnel current, that occurs without mechanical contact between the electrodes, crucially depends on the tip-sample separation, and is used for imaging the surface topography. While raster-scanning over the surface, the current is kept constant at a pre-set value I_{set}. This is accomplished by a feedback control unit that adjusts the tip-sample distance, as depicted in Fig. 2.1. The distance regulation $\Delta z(x, y)$ as a function of tip position (x, y) is then used to generate a three-dimensional image of the surface topography.

In spin-polarized scanning tunneling microscopy (SP-STM), a magnetic probe tip generates a spin-polarized tunnel current. The dependence of the tunnel current on the relative orientation between the tip and the sample magnetization

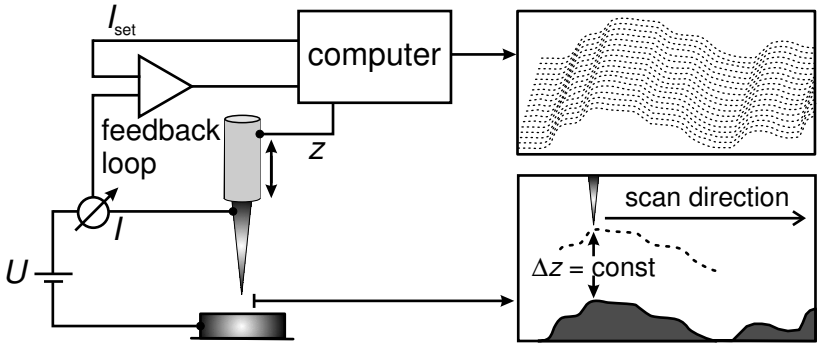

Figure 2.1: Imaging conducting surfaces on a local scale. Schematic of the experimental realization in a scanning tunneling microscopy setup.

is used for imaging the magnetic surface properties, combining the high lateral resolution with spin-sensitivity [32].

2.1 The tunnel effect

Consider an electron of energy E arriving at a rectangular potential barrier of height V_0 and width d. In classical physics, for an energy $E < V_0$ the electron can not penetrate the barrier, and is totally reflected at the potential step, as depicted in Fig. 2.2(a). However, in quantum mechanics, the electron may penetrate the forbidden region provided $V_0 < \infty$, and for $d < \infty$ it has a finite transmission probability. This phenomenon is called *tunneling*. Consequently, the electrons are partially reflected at the potential step, as depicted in Fig. 2.2(b).

Due to the wave-particle duality in quantum mechanics, the electron is described by a wavefunction $\psi(z)$ that obeys the time-independent Schrödinger equation

$$\left(-\frac{\hbar^2}{2m}\frac{\mathrm{d}^2}{\mathrm{d}z^2} + V(z)\right)\psi(z) = E\psi(z), \tag{2.1}$$

with m being the electron mass and $\hbar = h/2\pi$ being the reduced Planck constant. As depicted in Fig. 2.2(c), the potential $V(z)$ is given by

region I: $z < 0$, $V(z) = 0$, in front of the barrier,
region II: $0 \leq z \leq d$, $V(z) = V_0$, inside the barrier,
region III: $d < z$, $V(z) = 0$, behind the barrier.

The corresponding solutions of Eq. 2.1 are

region I: $\psi_1 = \mathrm{e}^{\mathrm{i}kz} + A\mathrm{e}^{-\mathrm{i}kz}$
region II: $\psi_2 = B\mathrm{e}^{\kappa z} + C\mathrm{e}^{-\kappa z}$
region III: $\psi_3 = D\mathrm{e}^{\mathrm{i}kz}$,

where $k^2 = 2mE/\hbar^2$ and $\kappa^2 = 2m(V_0 - E)/\hbar^2$.

In region I, the incoming electron wave ($\mathrm{e}^{\mathrm{i}kz}$) traveling to the right is superimposed on a reflected wave ($A\mathrm{e}^{-\mathrm{i}kz}$), traveling to the left. In region III, there is only a right traveling wave ($D\mathrm{e}^{\mathrm{i}kz}$) without a reflected one. Within the potential barrier (region II), the electron is described by a right traveling, exponentially damped wave ($B\mathrm{e}^{\kappa z}$), superimposed on a wave reflected at $z = d$ ($C\mathrm{e}^{-\kappa z}$). κ may be interpreted as the *inverse decay length*, as $\psi(z_\kappa = \kappa^{-1}) = 1/\mathrm{e} \cdot \psi(z = 0)$. The coefficients A, B, C, D are determined by the *wave-matching method*, meaning that the overall wavefunction has to be continuous and continuously differentiable at the points of discontinuity of the potential ($z = 0, d$).

The ratio of the incident probability current

$$j_1 = \frac{\hbar k}{m} \tag{2.2}$$

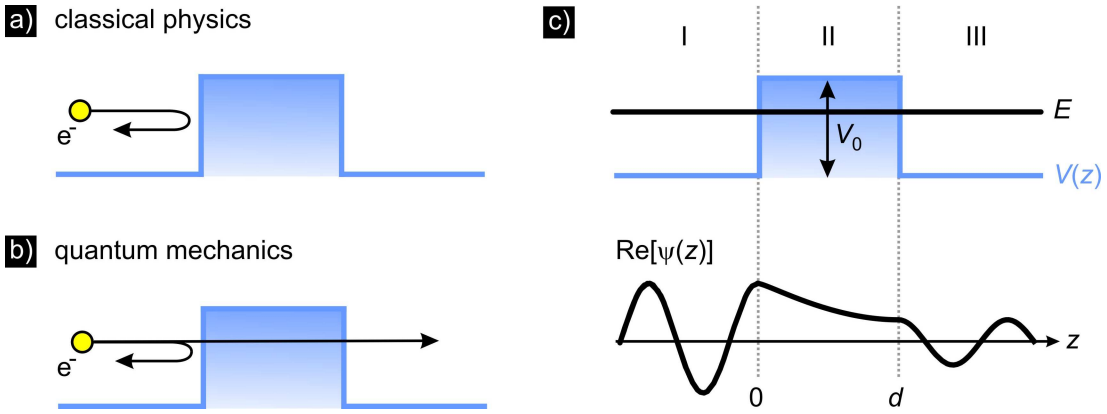

Figure 2.2: The tunnel effect. (**a**) In classical physics, an electron is reflected at a potential barrier if its energy is less than the height of the barrier. (**b**) In quantum mechanics, the electron has a finite probability to be found behind the barrier of finite thickness. (**c**) Quantum-mechanically the electron is described by a wave function $\psi(z)$ that obeys the time-independent Schrödinger equation for all three regions (I,II,III) of the potential $V(z)$ and needs to fulfill continuity conditions at $z = 0$, d. Illustration concept adapted from [33].

to the transmitted probability current

$$j_3 = -\frac{\mathrm{i}\hbar}{2m}\left(\psi_3^*(z)\frac{\mathrm{d}\psi_3(z)}{\mathrm{d}z} - \psi_3(z)\frac{\mathrm{d}\psi_3^*(z)}{\mathrm{d}z}\right) = \frac{\hbar k}{m}\,|D|^2 \tag{2.3}$$

defines the transmission coefficient

$$T = |D|^2 = \frac{1}{1 + \frac{(k^2+\kappa^2)^2}{4k^2\kappa^2}\sinh(\kappa d)}. \tag{2.4}$$

It predicts what portion of the electrons arriving a the potential barrier will be found behind it.

In the limiting case of a decay length being small compared to the barrier width d ($\kappa d \gg 1$), the transmission coefficient can be approximated by

$$T \approx \frac{16k^2\kappa^2}{(k^2+\kappa^2)^2} \cdot \mathrm{e}^{-2\kappa d}. \tag{2.5}$$

Consequently, the transmission probability and thereby the tunnel current $I \propto T$ is dominated by the exponential factor, whose argument is proportional to $\left(d \cdot \sqrt{V_0 - E}\right)$ with $V_0 - E$ being the effective barrier height and d being the barrier width. This simple model reproduces the experimentally observed distance dependence of the tunnel current and illustrates its high sensitivity to the tip-sample distance d in an STM.

2.2 The tunnel effect in the STM

In an STM, electrons tunnel between two metallic electrodes, namely the tip and the sample. Here, the potential barrier is given by the vacuum between tip and sample, and its width corresponds to the tip-sample distance. Hence, the STM is an example of metal-vacuum-metal-tunneling.

If we first consider only one, undisturbed electrode at $T = 0\,\mathrm{K}$, electrons occupy electronic states up to the Fermi level E_F, as depicted in Fig. 2.3(a). At the surface, there is a potential barrier higher than E_F in order to keep the electrons within the metal. The height of this barrier is called work function and denoted by ϕ. It is the energy that is needed to bring an electron from E_F of the surface to the vacuum at infinite distance, represented by the vacuum level $E_\mathrm{vac} = E_\mathrm{F} + \phi$.

When bringing a second electrode very close to the first, the vacuum potential barrier in between is of finite thickness thereby allowing electrons to tunnel from one side to the other until the Fermi levels are equal. If the work function of the tip and the sample electrode differ ($\phi_\mathrm{t} \neq \phi_\mathrm{s}$), the potential barrier shape becomes rather trapezoidal than rectangular, as depicted in Fig. 2.3(b). As soon as the Fermi levels are equal, the same number of electrons tunnel from the left to the right and vice versa. Consequently, there is no net current.

The situation changes on applying a small sample bias voltage U between the electrodes, as shown schematically in Fig. 2.3(c). Now, the Fermi levels of tip and sample are shifted relative to each other by eU and electrons can tunnel from occupied states of the negatively biased electrode into unoccupied states of the positively biased electrode. A net tunnel current flows.

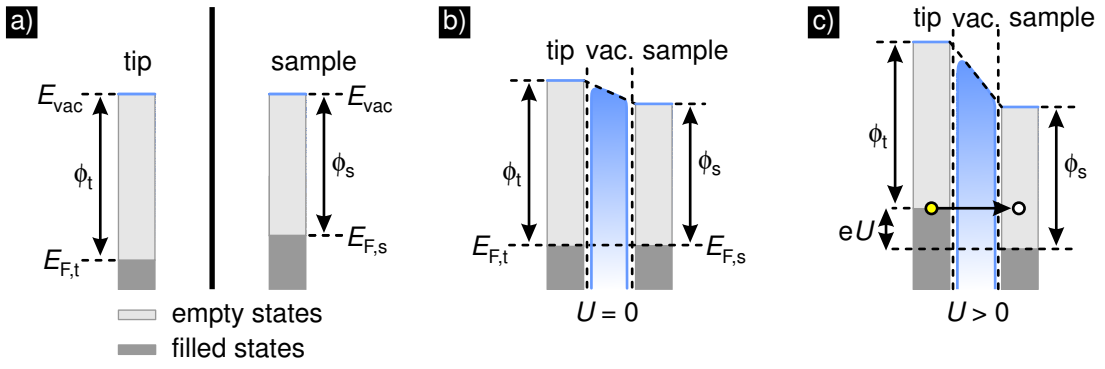

Figure 2.3: The tunnel effect in the STM. Schematic sketch of the energy level diagrams. (**a**) Independent tip and sample electrodes. E_vac: vacuum level, $E_\mathrm{F,t}$, $E_\mathrm{F,s}$: Fermi level and ϕ_t, ϕ_s work function of tip and sample, respectively. (**b**) Tip and sample separated by a small vacuum gap in electronic equilibrium. As $E_\mathrm{F,t} = E_\mathrm{F,s}$, there is no net current. (**c**) Applying a positive sample bias U results in electron tunneling from occupied tip states into unoccupied sample states.

Adopting the simple model of Sec. 2.1, the height of the tunneling barrier V_0 is determined by the work functions of the tip and the sample and the width d by the tip-sample separation. In a typical STM experiment, $\phi \approx 4\,\mathrm{eV}$ and $d \approx 5\,\text{Å}$, resulting in $\kappa \approx 1\,\text{Å}^{-1}$. As a consequence, when increasing the tip-sample distance by about 1 Å, the tunnel current decreases by about one order of magnitude. This leads to the high vertical resolution of the STM. Additionally, imagine a probe tip exhibiting a micro-protrusion – also known as a *nanotip* – at the tip apex. If this nanotip is about 2 Å closer to the sample surface, the tunnel current will almost exclusively flow through this outermost atom or atomic cluster, providing high lateral resolution [34].

2.2.1 Topography

While the simple model in Sec. 2.1 describes the exponential distance dependence of the tunnel current, it ignores the influence of the electronic structure of the tip and the sample.

Instead of solving the stationary Schrödinger equation for the combined system of tip, vacuum barrier and sample, in 1961 Bardeen calculated the tunnel current by the overlap of the undisturbed wavefunctions of two planar, weakly coupled electrodes within the framework of time-dependent first-order perturbation theory [35]. In the 1980's Tersoff and Hamann refined Bardeen's formalism in order to appropriately describe the tunneling process in the STM geometry [36, 37]. The authors approximated the tip as being locally spherical and allowed only s-type wave functions to contribute to the tunneling matrix elements. Their model geometry is depicted in Fig. 2.4. Here, R is the effective tip radius, $\vec{r}_0$ is the center of curvature of the tip, and d is the tip-sample distance.

In the limiting case of low temperatures and small bias voltages U, so that only states at E_F have to be accounted for, the current is given by

$$I \propto U \cdot \rho_\mathrm{t}(E_\mathrm{F}) \cdot \mathrm{e}^{2\kappa R} \cdot \sum_\nu |\psi_\nu(\vec{r}_0)|^2 \cdot \delta(E_\nu - E_\mathrm{F}) \tag{2.6}$$

with $\rho_\mathrm{t}(E_\mathrm{F})$ being the tip density of states at the Fermi level. Analog to the one-dimensional tunneling shown in Sec. 2.1, the decay rate κ is proportional to the square root of the effective local potential barrier height $\bar{\phi} = E_\mathrm{vac} - E_\mathrm{F}$, which is to a good approximation equal to the average of the tip and sample work functions. The quantity

$$\rho_\mathrm{s}(E_\mathrm{F}, \vec{r}_0) = \sum_\nu |\psi_\nu(\vec{r}_0)|^2 \cdot \delta(E_\nu - E_\mathrm{F}) \tag{2.7}$$

can be interpreted as the surface local density of states (LDOS) at the Fermi level, evaluated at the center position $\vec{r}_0$ of the tip. As the sample wave functions ψ_ν decay exponentially into the vacuum

$$|\psi_\nu(\vec{r}_0)|^2 \propto \mathrm{e}^{-2\kappa s} \,\text{with}\, s = d + R, \tag{2.8}$$

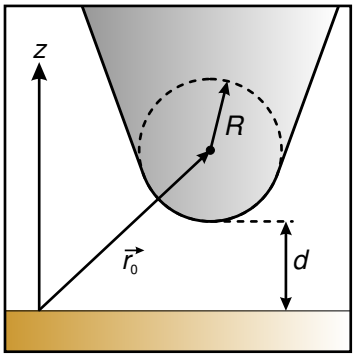

Figure 2.4: The tunneling geometry in the Tersoff-Hamann model. Sketch of tip and sample: $\vec{r}_0$ is the center of curvature of the tip, R is its effective radius, and d denotes the tip-sample distance.

the tunnel current depends exponentially on the tip-sample distance.

The Tersoff-Hamann model assumes a constant tip density of states, thereby reducing the role of the tip simply to that of a probe. As a result, the tunnel current is governed only by the sample properties. According to Eq. 2.6 it is directly proportional to the LDOS of the sample at the position of the tip. Hence, the STM data $z(x,y)|_{I=\text{const.}}$, that are acquired when recording the z component as a function of the lateral position (x,y) while scanning with the tip across a sample surface at a fixed tunnel current I, can be interpreted as traces of constant LDOS at E_F above the surface at the location of the tip. Generally, the LDOS follows the surface geometry (like step edges, defects, and surface reconstructions) thereby allowing constant-current STM images to be interpreted as the surface topography to a good approximation. However, there are some exceptional cases where the LDOS does not follow the surface topography. For example, some types of atoms or molecules sitting on top of flat surfaces locally reduce the LDOS, thereby appearing as depressions in the topography image [38–40]. This eventuality has to be kept in mind when interpreting constant-current STM 'topography' images.

2.2.2 Spectroscopy

In the previous section the tunneling process was described in the limit of low bias voltages U. When U is increased, the Tersoff-Haman model can be extended to the case of a tunnel current integrated over a range of energies

$$I \propto \int_0^{eU} \rho_\text{t}(E_\text{F} - \text{e}U + E) \cdot \rho_\text{s}(E_\text{F} + E) \cdot T(E_\text{F} - \text{e}U + E, E_\text{F} + E)\text{d}E, \qquad (2.9)$$

with a transmission factor

$$T(E_\text{F} - \text{e}U + E, E_\text{F} + E) = \exp\left[-s \cdot \sqrt{\frac{4m}{\hbar^2}\left(\phi_\text{t} + \phi_\text{s} + eU - 2(E_\text{F} + E)\right)}\right], \qquad (2.10)$$

with ϕ_t and ϕ_s being the work functions of tip and sample, respectively.

According to Eq. 2.9, for a given bias voltage $U > 0$ electrons from occupied states of the tip in the energy interval from $(E_F - eU)$ to E_F tunnel into unoccupied states of the sample, as sketched in Fig. 2.3(c). For $U < 0$ the situation is reversed and electrons from occupied sample states tunnel into unoccupied states of the tip. Note, that according to Eq. 2.10, the current mainly originates from electrons tunneling from the Fermi level E_F since they experience the lowest energy barrier.

With the assumption of ρ_t being constant in energy, differentiation of Eq. 2.9 with respect to the applied bias voltage U results in the *differential conductance*

$$\mathrm{d}I/\mathrm{d}U(U) \propto \rho_t(E_F) \cdot \rho_s(E_F + eU) \cdot T(E_F, E_F + eU) \tag{2.11}$$

Assuming T varies monotonically with U, $\mathrm{d}I/\mathrm{d}U$ is a good measure of ρ_s at an energy equal to eU [41–43].

Consequently, measuring $\mathrm{d}I/\mathrm{d}U(U)$ at constant tip-sample separation gives an approximate measure of the LDOS as a function of energy eU at a constant height above the surface. This is realized by stabilizing the tip above the surface at I_{stab} and U_{stab}. Then, the tip-sample distance is fixed by switching the feedback loop off. While the voltage is swept from an initial to a final bias voltage, the tunnel current $I(U)$ is measured. Numerical differentiation of $I(U)$ yields the respective $\mathrm{d}I/\mathrm{d}U$ signal. In this thesis, the lock-in technique was used to determine $\mathrm{d}I/\mathrm{d}U$: A small ac modulation voltage ($U_{mod} = 40\,\mathrm{mV}$) is added to the bias voltage at a high reference frequency ($f = 4.333\,\mathrm{kHz}$), and the in-phase current modulation (i.e. $\mathrm{d}I/\mathrm{d}U$) is analyzed with a lock-in amplifier.

Investigating the electronic properties of a sample at one particular energy eU_0 with lateral resolution is achieved by obtaining so-called $\mathrm{d}I/\mathrm{d}U$ *maps*. In contrast to a full $\mathrm{d}I/\mathrm{d}U(U)$ spectrum, where the feedback loop is switched off during voltage ramping, the $\mathrm{d}I/\mathrm{d}U$ signal at fixed bias voltage U_0 can be recorded with the feedback loop on. Hence, simultaneously to the constant-current topographic $z(x, y)$ data, the lock-in technique derives the $\mathrm{d}I/\mathrm{d}U(x, y, \mathrm{e}U_0)$ signal at the voltage U_0 at each position (x, y) on the surface. This allows for the direct correlation of topographic and spectroscopic sample properties.

Note, that Eq. 2.11 was deduced assuming a constant tip density of states. However, the electronic structure of the tip may also change with energy and applied bias voltage. This has to be kept in mind when analyzing scanning tunneling spectroscopy data.

2.3 Spin-polarized scanning tunneling microscopy

SP-STM is based on the electron tunneling between two *magnetic* electrodes. In this case, the tunnel current is not only governed by the electronic properties of the junction but also by its magnetic properties.

Within the Stoner model for ferromagnets, owing to the exchange interaction the density of states at the Fermi level is expected to split into spin-up states and spin-down states, the former being energetically lowered while the latter are raised in energy. As states are filled up to the Fermi level, this results in a larger occupation number for spin-up states than for spin-down states, therefore being also called *majority* spins and *minority* spins. The ferromagnet's magnetization is then determined by the difference of the respective occupation numbers and its magnetization direction defines a quantization axis for the electron spin magnetic moment. Moreover, the exchange splitting of the spin-up and spin-down band result in a spin-polarization at the Fermi level

$$P(E_\mathrm{F}) = \frac{\rho^\uparrow(E_\mathrm{F}) - \rho^\downarrow(E_\mathrm{F})}{\rho^\uparrow(E_\mathrm{F}) + \rho^\downarrow(E_\mathrm{F})}, \tag{2.12}$$

with $\rho^{\uparrow,\downarrow}$ being the spin-dependent density of states.

The fundamental concept of spin-polarized tunneling based on electron spin and energy conservation is depicted in Fig. 2.5 for (a) parallel and (b) antiparallel configuration of the magnetic electrodes. Each of the magnets is characterized by its exchange-split density of states $\rho_\uparrow(E)$ and $\rho_\downarrow(E)$. For positive bias voltage U, a spin-up electron from the tip can only tunnel into an unoccupied spin-up state of the sample. Since the tunneling probability depends on the number of electronic states available, the spin-polarized current will be larger for the parallel configuration of the magnetic electrodes than for the antiparallel configuration. This phenomenon is known as the *spin-valve* or *tunneling magnetoresistance* (TMR) effect.

A theory of spin-polarized tunneling between two planar magnetic electrodes has been developed by Slonczewski in 1989 [44]. In the limiting case of vanishing bias voltage U and a free-electron-like behavior of the conduction electrons, the spin-polarized tunnel current I_sp between two spin-polarized electrodes is described by

$$I_\mathrm{sp} = I_0[1 + P_1 \cdot P_2 \cdot \cos(\angle(\vec{m}_1, \vec{m}_2))], \tag{2.13}$$

where I_0 is the spin-averaged current, P_i is the spin polarization, and $\vec{m}_i$ is the magnetic moment of the electrodes [44].

According to Eq. 2.13 the spin-polarized tunnel current depends on the cosine of the angle θ between the magnetic moments of the two electrodes, which has been observed experimentally already in 1975 by Jullière [45]. In 1990, Wiesendanger *et al.* demonstrated the TMR effect in an STM geometry [46].

In 2001, Wortmann *et al.* extended the Tersoff-Hamann theory for the spin-polarized case of STM imaging [47]. Assuming a spin-up and spin-down tip density of states being constant in energy, the spin-dependent differential conductance is given by

$$\mathrm{d}I/\mathrm{d}U(\vec{r}_0, U) \propto \underbrace{\rho_\mathrm{t} \cdot \rho_\mathrm{s}(\vec{r}_0, E_\mathrm{F} + eU)}_{\text{spin-averaged}} + \underbrace{\vec{m}_\mathrm{t} \cdot \vec{m}_\mathrm{s}(\vec{r}_0, E_\mathrm{F} + eU)}_{\text{spin-dependent}}, \tag{2.14}$$

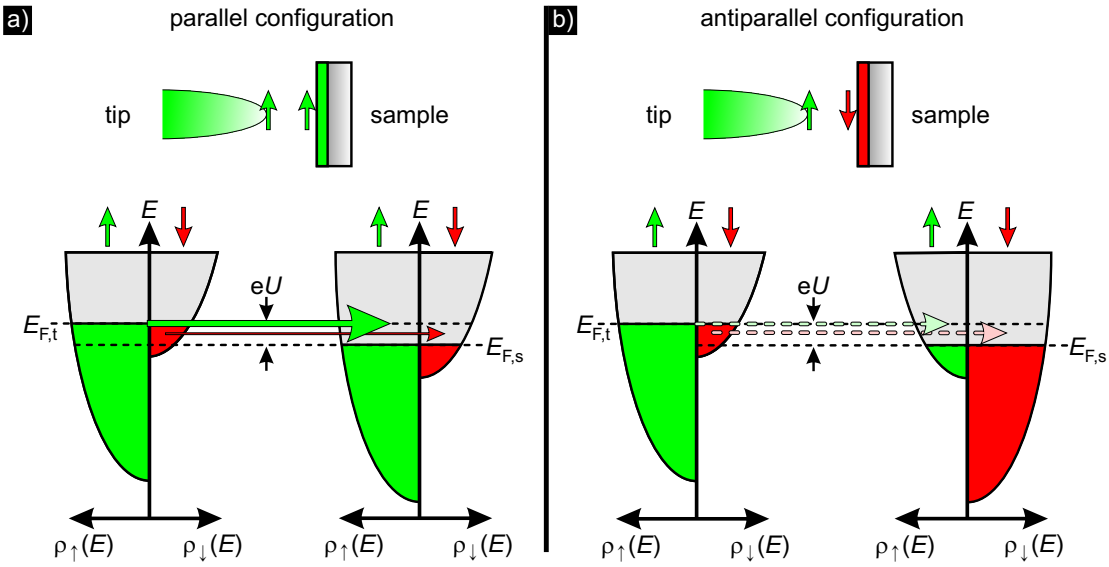

Figure 2.5: Spin-polarized scanning tunneling microscopy. Schematic sketch of the exchange-split densities of states $\rho_{\uparrow\downarrow}$ as a function of energy E for tip and sample electrode in the case of a positive sample bias U for (**a**) parallel and (**b**) antiparallel configuration of tip and sample magnetization. Compared to the parallel configuration the number of unoccupied spin-up states of the sample is decreased in the antiparallel configuration, leading to a reduced tunnel current, as indicated by the arrows.

where $\vec{r}_0$ denotes the position of the tip apex and $\vec{m}_{\mathrm{t,s}}$ is the local tip and sample magnetization equal to $(\rho^{\uparrow} - \rho^{\downarrow})\vec{e}_{\mathrm{t,s}}$ with $\vec{e}_{\mathrm{t,s}}$ being the respective magnetization axis. According to Eq. 2.14 also the differential conductance is composed of a spin-averaged and a spin-dependent contribution, the latter depending on the relative orientation of tip and sample magnetization. Combining Eq. 2.12 with Eq. 2.14 results in

$$\mathrm{d}I/\mathrm{d}U(\vec{r}_0, U, \theta) \propto \mathrm{C}[1 + P_{\mathrm{t}}P_{\mathrm{s}}(\vec{r}_0, E_{\mathrm{F}} + \mathrm{e}U)\cos\left(\theta(\vec{r}_0)\right)]\,, \tag{2.15}$$

with $C = \rho_{\mathrm{t}}\rho_{\mathrm{s}}(\vec{r}_0, E_{\mathrm{F}} + \mathrm{e}U)$ being a constant. Hence, the spin-polarized part of the differential conductance depends on the cosine of the angle θ between the tip and sample magnetization direction. If tip and sample are parallel or antiparallel magnetized, $\mathrm{d}I/\mathrm{d}U$ exhibits a maximum or minimum value. For a perpendicular magnetization orientation the spin-polarized contribution to $\mathrm{d}I/\mathrm{d}U$ vanishes.

In SP-STM experiments, a probe tip of fixed magnetization direction scans across a magnetic surface while recording the differential conductance $\mathrm{d}I/\mathrm{d}U$. A laterally varying sample magnetization direction results in a laterally varying $\theta(x, y)$. As a consequence, color-coding the variation of the measured $\mathrm{d}I/\mathrm{d}U(x, y)$ signal as a function of lateral tip position (x, y) results in a map that represents the magnetic structure of the sample.

Chapter 3

Spin-Polarized Scanning Field Emission Microscopy (SP-SFEM)

In the previous chapter, tunneling electron transfer from one electrode to another has been introduced. Alternatively, electrons can be transfered by means of an electric field. It rips out electrons of the emitter electrode and accelerates them towards the collector electrode. As will be shown in this chapter, the emission current can be used for imaging purposes.

3.1 Surface barrier potential

As already discussed in Sec. 2.2, in a metal at $T = 0\,\mathrm{K}$, electrons occupy electronic states up to the Fermi level E_F. At the surface, a potential barrier higher than E_F keeps the electrons within the metal. The height of this barrier is called the work function ϕ. It is the energy that is needed to bring an electron from E_F of the surface to the vacuum level E_vac at infinity.

Generally, the potential at the surface exhibits a smooth transition between the inner potential of the bulk and the vacuum level. Here, the evolution of the barrier potential with distance z from the surface is expected to be determined by the exchange-and-correlation interaction of an electron in front of the surface with the bulk electrons. The simplest barrier describing a planar metal-vacuum interface is the so-called *image potential* barrier:
It is a main characteristic of metals that they possess charge carriers, normally electrons, that are free to move. As a result, in electrostatics a metal surface represents an equipotential surface where the component of the electric field parallel to the surface vanishes. The presence of an electron at a distance $+z$ in front of the surface results in a rearrangement of the electrons within the metal. Hence, the electron induces a polarization charge within the near surface region of the metal. An electric field is formed that is identical to the classical Coulomb field: Here, the effect of the polarization of the metal in the near-surface region is the

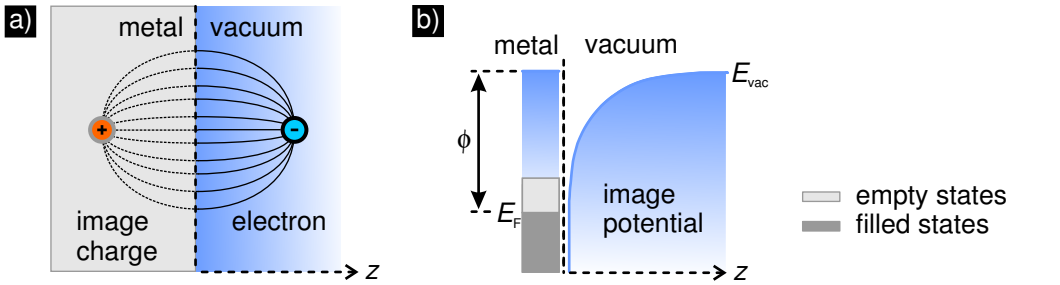

Figure 3.1: Surface barrier potential. (**a**) Electric field induced by an electron in front of a metal and its equivalent dipole-field with a positive (image) charge at a distance $-z$ to the surface. **b**) Schematic of the related image potential. E_F: Fermi level, E_{vac}: vacuum level, ϕ: work function.

same as that of an opposite charge located at the distance $-z$ from the surface, as depicted in Fig. 3.1(a). Consequently, it can be described by a virtual *image charge*.

An electron in front of the metal feels an attractive force

$$F(z) = -\frac{e^2}{4\pi\epsilon_0(2z)^2}\,, \tag{3.1}$$

with z the coordinate perpendicular to the surface, e the elementary charge, and ϵ_0 is the vacuum permittivity. Eq. 3.1 is the classical Coulomb force between two charges with opposite polarity at a distance $2z$. The image force depends only on the z-coordinate. Moving the electron perpendicular to the surface by Δz results in a shift of the image charge by $-\Delta z$. However, moving the electron parallel to the surface needs no effort. So it is a one-dimensional problem.

Eq. 3.1 corresponds to the attractive *image potential*

$$V(z) = E_{vac} - \frac{e^2}{4\pi\epsilon_0}\frac{1}{4z} \quad \text{for } z > 0\,, \tag{3.2}$$

with the vacuum energy E_{vac} as a reference level. Hence, the Coulomb-like image potential converges to the vacuum level with increasing distance from the surface, as depicted in Fig. 3.1(b).

3.2 Field emission

The vacuum potential in front of a surface can be considered as an infinitely wide potential barrier preventing the electrons to escape from the surface. In the presence of a negative electric field, the original surface barrier potential is modified by an electric field potential resulting in a triangular barrier of finite thickness, as depicted in Fig. 3.2. The triangular potential barrier is thereby

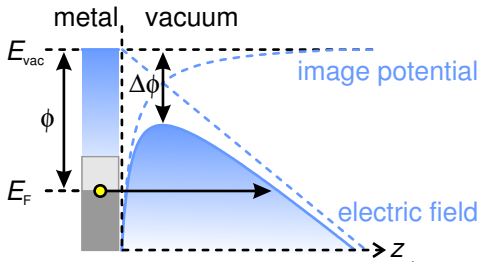

Figure 3.2: Field emission. Schematic of the influence of a (negative) applied electric field on the surface barrier. It effectively reduces the potential barrier by $\Delta\phi$ thereby allowing electrons to tunnel into vacuum.

lowered and rounded at its tip due to the image force. The shape of the potential barrier in front of the surface is thus determined by E_{vac}, the applied external electric potential and the image charge potential

$$V(z) = E_{\mathrm{vac}} - \mathrm{e}Fz - \frac{1}{4\pi\epsilon_0}\frac{\mathrm{e}^2}{4z} \quad \text{for } z > 0\,, \tag{3.3}$$

with F being the external electric field [48]. Consequently, owing to the influence of an applied electric field the potential barrier at the surface is bent down to a finite thickness and an electron within the metal can then tunnel through the classically forbidden barrier into the vacuum. The reduction of the image potential barrier owing to the electric field is

$$\Delta\phi = \sqrt{\frac{\mathrm{e}^3 F}{4\pi\epsilon_0}} = 3.79 \cdot 10^{-2}\sqrt{F}\,, \tag{3.4}$$

and is known as the *Schottky effect* [48].

Electron emission from a cold metal surface in the presence of a strong electric field on the order of 1-10 GV/m was discovered by Wood in 1897 and is called *field emission* [49]. In 1923, Schottky attempted to explain the phenomenon based on classical theory [48]. He tried to describe field emission by means of electrons thermally excited over a potential barrier at a surface, whose width is reduced by the applied electric field. However, the experimentally determined fields capable of initiating electron emission were up to 50 times lower than predicted by this theory. In 1926 Milikan, Eyring and Lauritsen observed that the emission current depends exponentially on the applied potential [50, 51], and two years later Fowler and Nordheim developed a first theory of field emission based on quantum mechanical tunneling of electrons through a surface barrier at a metal-vacuum interface [19]. Therefore, field emission is sometimes called *Fowler-Nordheim tunneling*.

In the original work, Fowler and Nordheim carried out an exact solution of the Schrödinger equation for a simple triangular barrier. In their calculations free electrons arrive according to Fermi-Dirac statistics at a surface $z = 0$ at which

their potential energy is suddenly increased according to Eq. 3.3 when omitting the last term representing the image potential. Hence, the surface potential is assumed to be a step function plus the applied electric field. The probability of penetrating the potential barrier is then predicted by solving the Schrödinger equation by means of the wave function matching method (cf. Sec. 2.1) [52]. As a result, the emission current density is given by

$$j(F) = \mathrm{a}\phi^{-1}F^2\exp\left(-\mathrm{b}\frac{\phi^{3/2}}{F}\right), \tag{3.5}$$

where the external electric field F is taken as a positive quantity, and a and b are universal constants given by

$$\mathrm{a} = \frac{\mathrm{e}^3}{8\pi h} = 1.541434 \cdot 10^{-6}\,\mathrm{AeVV}^{-2}, \tag{3.6}$$

$$\mathrm{b} = \frac{4}{3}\frac{\sqrt{2m}}{\mathrm{e}\hbar} = 6.830888 \cdot 10^{9}\,\mathrm{eV}^{-3/2}\mathrm{Vm}^{-1}, \tag{3.7}$$

with m being the electron mass, h being the Planck constant and $\hbar = h/2\pi$ being the reduced Planck constant [53].

Standard Fowler-Nordheim theory is based on the assumptions that (i) the electrons of the metal conduction band can be described as free particles, (ii) the electrons are in thermodynamic equilibrium and obey Fermi-Dirac statistics, (iii) the metal is at $T = 0\,\mathrm{K}$, (iv) it exhibits a smooth flat surface, (v) has a local work function that is uniform across the emitting surface and is independent of the external field, and (vi) there is a uniform electric field above the emitting surface [52]. Whereas the original work of Fowler and Nordheim assumed that (vii) exchange-and-correlation effects may be neglected in a first approximation, subsequent analytical treatments [54–56] have used the more realistic barrier given by Eq. 3.3, thereby assuming that the exchange-and-correlation interaction between the field-emitted electron and the surface can be represented by a classical image potential. Then they used the JWKB [57, 58] approximation to obtain an expression for the barrier transmission coefficient.

Let $n(W)$ be the number of electrons per second with energies between W and $W + \mathrm{d}W$, incident on $1\,\mathrm{cm}^2$ of the barrier surface from within the metal, and W be the part of the energy for the motion normal to the surface:

$$W = \frac{p_z^2}{2m} + V(z), \tag{3.8}$$

with p_z being the momentum component normal to the surface, and $V(z)$ being the potential barrier given by Eq. 3.3. The current density j through the barrier is then given by

$$j(F) = \mathrm{e}\int_0^\infty n(W)D(W,F)dW, \tag{3.9}$$

where $D(W,F)$ is the transmission probability for an electron of energy W to tunnel through the potential barrier[52, 54, 59]. Within the JWKB approximation [57, 58], the transmission coefficient for a particle of energy W traversing a barrier extending from z_1 to z_2 is given by

$$D(W,F) = \exp\left(-\int_{z_1}^{z_2} dz \sqrt{\frac{8\mathrm{m}}{\hbar^2}\left(V(z)-W\right)}\right) . \tag{3.10}$$

z_1 and z_2 are the classical turning points, where p_z^2 becomes zero. Note, that the WKB transmission coefficient is valid only for $W < V_{\max}$, the potential maximum [60]. Hence, $D(W,F)$ is assumed to be unity for $W > V_{\max}$ [61]. Performing the integral results in

$$D(W,F) = \exp\left(-\frac{4}{3}\left(\frac{2m}{\hbar^2}\right)^{1/2}\frac{\left(E_{\mathrm{vac}}-W\right)^{3/2}}{\mathrm{e}F}v(y)\right) , \tag{3.11}$$

where $v(y)$ is a so-called Nordheim function, that depends on the relative reduction of the barrier $y = \Delta\phi/\left(\phi + E_{\mathrm{F}} - W\right)$ through the image charge (cf. Eq.3.4) [52]. It is tabulated and can be found in Ref. [60, 62]. When the influence of the image charge is neglected, $v(y)$ is set to unity. Otherwise, $v(y) < 1$ and gets the smaller, the more the barrier is lowered due to image charge effects. Consequently, $v(y)$ reduces the exponent thereby increasing the tunneling probability as the image potential removes a part of the barrier present in the pure triangular model.

Note, that the exponential decrease of the tunneling probability with increasing binding energy of the electrons (i.e. increasing $E_{\mathrm{vac}} - W$) according to Eq. 3.11 along with a low occupation probability of electronic states above E_{F} for temperatures below $T \leq 300\,\mathrm{K}$ result in a sharp energy distribution of the field-emitted electrons [52]. Hence, most of the field-emitted electrons will come from a narrow range of energy about E_{F} with a width of only a few 100 meV [60, 63].

Eq. 3.9 and Eq. 3.11 result in the standard Fowler-Nordheim equation [53]

$$j(F) = \mathrm{a}t^2(y_0)\phi^{-1}F^2\exp\left(-\mathrm{b}v(y_0)\frac{\phi^{3/2}}{F}\right) , \tag{3.12}$$

with $t(y_0)$ and $v(y_0)$ being the Nordheim functions depending on the relative reduction of the barrier $y_0 = \Delta\phi/\phi$ through the image charge (cf. Eq.3.4). Also $t(y)$ is tabulated and can be found in Ref. [60, 62]. It is close to unity and varies weakly with argument. According to Eq. 3.12, the applied electric field and the work function uniquely determine the field emission current density. Note that increasing the applied electric field by only a factor of 2 from e.g. $F = 1\,\mathrm{GV/m}$ to $2\,\mathrm{GV/m}$ increases the current density by 14 orders of magnitude, i.e. from 10^{-19} to $10^{-5}\,\mathrm{A/cm^2}$, which is due to the rapid variation of the exponential function.

The Fowler-Nordheim theory was experimentally confirmed for the first time by Müller [64] and Haefer [65], after the invention of the field emission microscope by Müller [66]. The experiments were performed with metallic tips, which strongly enhance the local electric field at the tip apex. For plane metal cathodes the Fowler-Nordheim theory could first not be confirmed, as field emission started already at electric field strengths on the order of 1-10 MV/m, which is up to 1000 times smaller than predicted by FN theory [67–69]. Schottky suggested the existence of micro-protrusions on the surface, that locally enhance the external electric field [48]. Now, it is widely recognized that emission does not take place over the whole electrode surface, but is restricted to some micron-sized sites. Experimentally, enhanced field emission from an individual site follows Fowler-Nordheim theory, provided the macroscopic field F in Eq. 3.12 is modified by a so-called field enhancement factor β to the microscopic value $\beta \cdot F$ [68]. The modified Fowler-Nordheim equation for the emission current is

$$I(F) = \frac{\mathrm{a}S(\beta F)^2}{\phi t^2(y)} \exp\left(-\frac{\mathrm{b}\phi^{3/2} v(y)}{\beta F}\right), \tag{3.13}$$

with S being the effective emitting surface through which the emission current I flows. Generally, β lies in the range $50 < \beta < 1000$ and S values in the range of $1\,\mathrm{nm}^2 < S < 1000\,\mu\mathrm{m}^2$ [70].

In 1988, Fink reported on the fabrication of ultrasharp emitter tips with an atomic arrangement that confined most of the electric field to the very end of the tip [17]. He claimed that they were 'a realization of a point source in the sense that [...] electrons are produced sequentially at one well-defined physical point in space, namely, the very end of the tip'. Serving as point-like field emitter, the angular divergence from the normal direction of electron emission was only 0.5° for single atom W-tips and 2° for W_6-clusters at the tip apex. In standard field emission the electric field is expected to be uniformly distributed over the entire curved end of the relatively blunt tips with typical radii of 100 nm, as shown schematically in Fig. 3.3(a). This results in opening angles in the order of 35 to 50° [71].

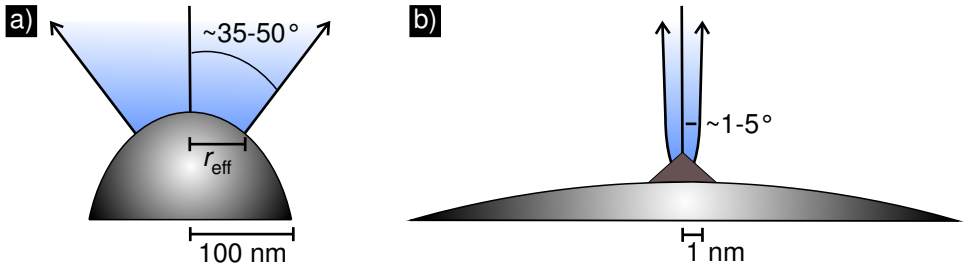

Figure 3.3: Comparison of a standard field emitter with a point-like emitter. Field emission from (**a**) a typical metal tip used in standard field emission experiments and (**b**) a nanotip. Illustration concept adapted from [71].

In contrast, in field emission from nanotips (with typical radii $r < 10\,\mathrm{nm}$), the electric field is concentrated to the very end of the tip, as depicted in Fig. 3.3(b). Hence, at the vicinal regions of the nanoprotrusion, the electric field is low and the corresponding tunneling barrier potential is too wide, so that transmission is unlikely. This results in opening angles being of the order of a few degrees, as found experimentally in Ref. [71–73]. In this case however, the one-dimensional model of a planar field-emitter as applied in the Fowler-Nordheim theory (cf. Eq. 3.13) does not hold any more. Instead, a three-dimensional description accounting for the actual emitter geometry is required [61, 74–79].

The opening angle of the electron beam and the concomitant beam width is a crucial property as it limits the lateral resolution of every imaging technique, where the field emission current is focused onto a sample and its transmittance, reflectance or interaction is used to gain information on the sample.

3.2.1 Spin-polarized field emission

As discussed in Sec. 3.2, the electrons field-emitted from a metal stem from a narrow energy window around E_F. Since ferromagnets exhibit a spin-dependent density of states at E_F [80], the field emission current from a magnetic emitter is expected to be spin-polarized.

Already in 1930, Fues and Hellmann suggested that application of a strong electric field to a ferromagnet should produce spin-polarized electrons [81]. However, the early field emission experiments with iron tips remained unsuccessful [82, 83], and it was not until 1967 that electron spin-polarization in field emission (from Gd) was observed [20].

In the 1970's, a strong effort was being made to produce spin-polarized electron beams by field emission [84–92]. Spin polarization was found in field emission from single-crystal tips of the 3d ferromagnets (Fe, Co, and Ni) [91, 92], thick films of the 3d and rare earth elements on W tips [90], and W tips coated with Eu-based compounds [85, 87, 89]. Usually in these experiments strong magnetic fields ($\approx 1.5\,\mathrm{T}$) had been applied parallel to the emitter axis to saturate its magnetization, and a moderate applied field was maintained during measurement to define a longitudinal quantization axis. Also, the measurements were performed at low temperature ($10 - 85\,\mathrm{K}$). The experimentally determined electron spin-polarizations ranged from a few percent up to $\approx 25\,\%$ [93]. Only spin-polarized field emission from the Eu chalcogenide films on W tips held at 10 K gave high values exceeding 90% [87]. However, the polarization and emitted current dropped drastically when the temperature was increased by only 7 K.

In the last decade, spin-polarized field emission regained attention, including emission from thin-film coated Co/W(111) [94], Co/W(001) [95], Fe/W(111) [95], Fe/W(001) [96], Fe/W(110) [97], and Co_2MnSi/W(001) [98, 99] tips. Unlike the earlier pioneering work, these new experiments investigated the polarization direc-

tion of spontaneously or remanently magnetized tips in the absence of a magnetic field at room temperature. Generally, it was found, that the transverse spin polarization directions and other aspects of field emission from the thin-film coated tips correlate with the magnetization characteristics of the respective ultrathin films on macroscopic surfaces of the same orientation [94–96, 98, 99].

Interestingly, the authors of Ref. [94–96] found spontaneous fluctuations in the spin-polarization direction between symmetry-equivalent transverse orientations of electrons emitted from W(001) and W(111) tips, that had been coated with a few ML of Fe or Co and were held at $T \geq 300\,\mathrm{K}$. The authors explained their observations by superparamagnetic fluctuations of the tip magnetization. At marginally larger thickness ($\gtrsim 15\,\mathrm{ML}$), long-term stability of the polarization magnitude and direction was observed. The authors concluded that the superparamagnetic limit can be overcome by cooling or by increasing the volume of the emitting domain by varying the film thickness [95].

3.3 Image-potential states

So far, only the role of the surface potential barrier when *extracting* electrons from the surface has been considered. Now, it will be discussed, what happens, when *bringing* an electron from the vacuum *into* the surface.

According to Eq. 3.1 and Eq. 3.2 an electron approaching a metal surface experiences the attractive force of the polarization charge that it induces in the surface near region. Hence, its potential energy is reduced when approaching the metal surface. Assuming to a first approximation an infinite high potential at the surface, the electron cannot penetrate into the metal. The electron gets reflected at the surface and travels back into vacuum, where it is reflected at the image potential thereby turning back to the surface, where it is reflected again and so on. Consequently, the electron is confined in a potential well perpendicular to the surface, given by the surface potential on the bulk-side and the Coulomb-like image potential on the vacuum side. In this one-dimensional potential well a Rydberg-like series of bound quantum states evolve, as depicted in Fig. 3.4(a). They are called *image-potential states* (IPS). Their existence at metal surfaces was predicted by Echenique and Pendry in 1978 [100] and a few years later confirmed in inverse photoemission experiments [101, 102].

The Schrödinger equation for this one-dimensional potential problem is

$$\left(-\frac{\hbar^2}{2m}\frac{\mathrm{d}^2}{\mathrm{dz}^2} - \frac{\mathrm{e}^2}{4\pi\epsilon_0}\frac{1}{4z}\right)\psi(z) = (E - E_{\mathrm{vac}})\,\psi(z)\,, \tag{3.14}$$

with solutions:

$$E_n = E_{\mathrm{vac}} - \frac{m}{32}\left(\frac{\mathrm{e}^2}{4\pi\epsilon_0\hbar^2}\right)^2\frac{1}{n^2} = E_{\mathrm{vac}} - \frac{\mathrm{Ry}}{16}\frac{1}{n^2}\,, \tag{3.15}$$

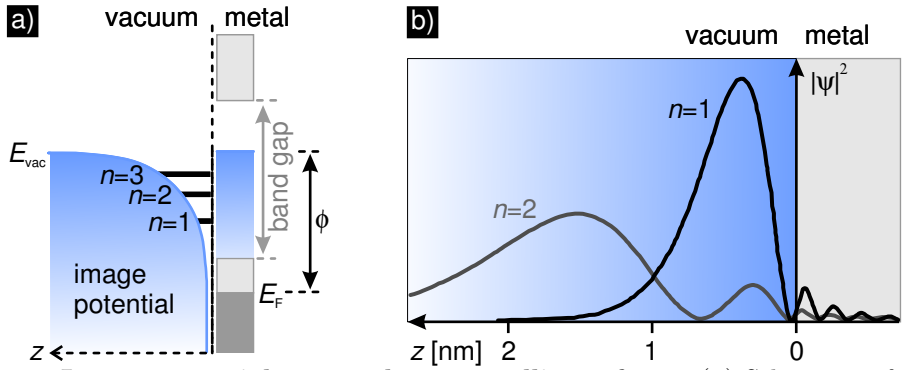

Figure 3.4: Image-potential states above metallic surfaces. (**a**) Schematic of the energetic positions in the quantum well formed by the image potential and the gap in the surface band structure. (**b**) The probability density $|\psi_n(z)|^2$ for the first two image-potential states.

with Ry = 13.6 eV being the Rydberg energy and $n = 1, 2, 3, ..$ being the quantum number. According to Eq. 3.15 the IPS are energetically located within ≈ 1 eV below the vacuum level. Hence, they are unoccupied. The energetic distance between successive IPS decreases with order n. The maximum of the probability density $|\psi_n(z)|^2$ lies a few Ångstrom above the surface, as depicted in Fig. 3.4(b), with the distance increasing quadratically with the quantum number n.

Note, that Eq. 3.14 is the same equation as for the radial part of the wavefunction when solving the Coulomb-problem of the hydrogen atom for s-wavefunctions (with an angular momentum quantum number $l = 0$) [103]. (Here the zero point of energy is chosen at infinity, $E_{vac} = 0$.) The only difference is the factor 4 in the denominator of the potential. This results in a reduction of the energy scale by a factor of 16 and an extension of the length scale by a factor of 4 compared to the hydrogen atom. Consequently, the IPS binding energy is reduced by a factor of 16 compared to the binding energy Ry = 13.6 eV of the hydrogen atom (cf. Eq. 3.15). In comparison to the radial part of the hydrogen wave function, the IPS wavefunction is expanded by a factor of 4 [102, 104]. As a result, the maximum of the probability density $|\psi_n(z)|^2$ is about 2 Å and 10 Å above the surface for the $n = 1$ and $n = 2$ state, respectively.

So far, we have assumed the potential inside the metal to be infinite, thereby preventing the electron to penetrate into the metal. However, there is a finite probability for the electron to escape into the bulk. The periodic potential within the crystal may result in electronic band gaps in certain directions. Such a band gap is already sufficient for the evolution of bound IPS above the surface. In the band gap the solution of the Schrödinger equation is an exponentially decaying wave function, as depicted in Fig. 3.4(b).

The finite penetration of the IPS wavefunction into the bulk changes its binding energy. This modification can be obtained within the phase shift model [100, 104, 105]. Here, the electron wavefunction is assumed to be repeatedly reflected at

the crystal- and surface-potential barrier with an energy-dependent phase shift. A solution is obtained only for energies, where the sum of the two phase shifts equals an integer multiple of 2π. Eq. 3.15 is then written as

$$E_n = E_{\text{vac}} - \frac{0.85\,\text{eV}}{(n+a)^2} \text{ with } n = 1, 2, 3, \ldots \tag{3.16}$$

with 0.85 eV being Ry/16 and a being a quantum defect. The latter accounts for the finite penetration of the wave function into the metal. It describes the reflectivity of the crystal, which depends on the energetic position of the IPS within the band gap: The value of a rises from 0 at the top of the band gap to 0.5 at the bottom of the band gap [106].

As $a \geq 0$ the quantum defect reduces the binding energy of the IPS compared to the ideal case of an infinite potential at the surface boundary $z = 0$ (cf. Eq. 3.15). Whereas for the ideal case of a 'hard wall' the wavefunction vanishes, $\psi(0) = 0$, for a finite potential there is a finite electron probability at $z = 0$. This shifts the maxima of the probability densities $|\psi_n(z)|^2$ further away from the surface. As a result, the binding energy is reduced, being taken into account by the quantum defect in Eq. 3.16.

Note, that IPS exist also above surfaces without a projected band gap around the vacuum level, as experimentally verified by inverse photoemission [107]. In this case, the states possess a propagating component in the bulk, but still the amplitude of the wave function at and outside the surface is enhanced (*resonant surface image states*). In contrast, for an IPS within a projected bulk band gap, the whole wave function is built up at and outside the surface and is exponentially damped within the bulk (*pure image state*) [108].

Parallel to the surface the IPS electrons can move freely, undisturbed by the surface corrugation, with an effective mass close to the free-electron value [109]. Consequently, taking the lateral dimensions into account, every IPS with quantum number n being discrete perpendicular to the surface corresponds to a two-dimensional image-potential band.

Extensive reviews on the physics of IPS may be found in e.g. Ref. [104, 110, 111].

3.3.1 Spin-dependent image-potential states

In a ferromagnet the electronic bands are exchange-split, and it was expected that the interaction of the IPS with the surface of the ferromagnet lifts the spin degeneracy of these states [112]. In a phase shift model [100, 104, 105] spin-up and spin-down electronic states can be treated separately as two subsystems, and the different positions of the spin-up and spin-down bulk band edges yield a spin-dependent crystal barrier. Hence, a spin-dependent quantum defect $a^{\uparrow\downarrow}$ is needed

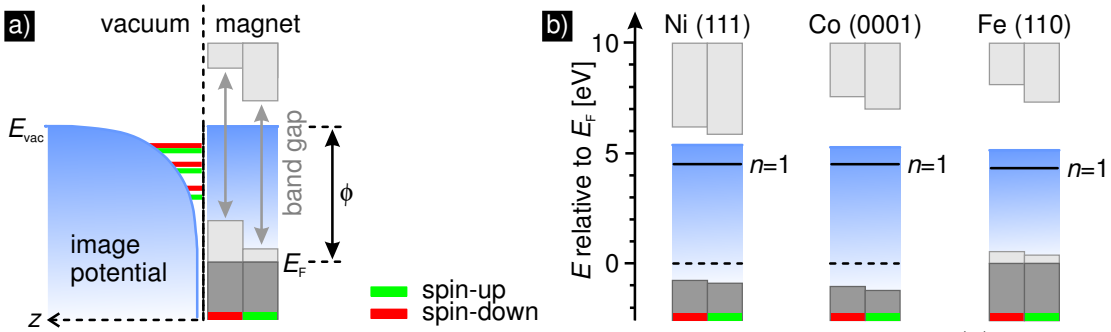

Figure 3.5: Spin-dependent image-potential states above ferromagnets. (**a**) Sketch of the surface potential and spin-dependent band structure of a ferromagnet. The spin-dependent energetic positions of the first three image-potential states are indicated. **b**) Schematic of the particular band-gap situation at $k_{||} = 0$ for three ferromagnetic surfaces. The position of the $n = 1$ image state is indicated.

to calculate the binding energy of the IPS in front of a ferromagnetic metal

$$E_n^{\uparrow\downarrow} = E_{\text{vac}} - \frac{0.85\,\text{eV}}{(n + a^{\uparrow\downarrow})^2} \text{ with } n = 1, 2, 3, \ldots \tag{3.17}$$

This results in an exchange splitting

$$\Delta E_n^{\downarrow\uparrow} = E_n^{\downarrow} - E_n^{\uparrow} = 2 \cdot 0.85\,\text{eV} \frac{a^{\uparrow} - a^{\downarrow}}{n^3} + \mathcal{O}\left(\frac{1}{n^4}\right) . \tag{3.18}$$

In other words, as the ferromagnet exhibits a spin-dependent band structure, a spin-up electron in an IPS is reflected at a different band gap than a spin-down electron, as depicted in Fig. 3.5(a). This results in different binding energies for spin-up and spin-down electrons and is taken into account by the spin-dependent quantum defect describing the spin-dependent reflectivity of the crystal. The latter depends on the energetic position of the spin-up (spin-down) IPS within the respective spin-up (spin-down) band gap.

The first experimental verification with spin-resolved inverse photoemission revealed an exchange splitting of (18 ± 3) meV for the $n = 1$ state on Ni(111) [113]. For Ni(001) an exchange splitting of (13 ± 13) meV was found [114]. Whereas on Fe(110) an exchange splitting of (57 ± 5) meV was observed [115], Cobalt surfaces exhibit the largest exchange-splittings found so far: (125 ± 24) and (96 ± 30) meV for Co($10\bar{1}0$), respectively [116, 117] and (78 ± 7) meV for Co(0001) [118].

Interestingly, as discussed in Ref. [24, 25], the exchange splittings of the IPS on Ni, Co and Fe surfaces do not follow the respective exchange splittings of the d-bands, that are smallest for Ni (≈ 0.3 eV) [119] and largest for Fe (≈ 2 eV) [120, 121]. One might naively expect the same scaling for the exchange splitting of the IPS. However, the energetic position relative to the band edges determines the penetration of the wave function into the solid and, thereby, their overlap with

bulk states. The binding energy of an IPS increases monotonically as it moves higher in the supporting bulk band gap. Since the spin-down gap lies higher than the spin-up gap, the spin-down IPS lies lower in its respective band gap, and its binding energy is slightly lower. As a consequence, the exchange splittings of IPS are *not only* influenced by the exchange splittings of the bulk bands *but also* by the particular band-gap situation.

In Fig. 3.5(b) the particular band-gap situation at $k_{||} = 0$ for the $n = 1$ IPS on Ni(111), Co(0001) and Fe(110) is shown [24, 113, 122]. The position of the $n = 1$ image state within the respective band gap is indicated [24, 113, 122]. Within the phase shift model, the exchange splitting of the $n = 1$ IPS can be roughly estimated to be of the order of $E_{\mathrm{B}}\delta E_{\mathrm{ex}}/E_{\mathrm{gap}}$, where E_{B} is the binding energy of the IPS ($\approx$ 1Ry/16), δE_{ex} is the exchange splitting at the top edge of the gap, and E_{gap} is the width of the gap [24]. As shown in Fig. 3.5(b) the exchange splitting at the top edge of the gap increases from Ni to Co and Fe. It is $\delta E_{\mathrm{ex}} = 0.2\,\mathrm{eV}$ for Ni(111), $\delta E_{\mathrm{ex}} = 0.74\,\mathrm{eV}$ for Co(0001) and $\delta E_{\mathrm{ex}} = 1.26\,\mathrm{eV}$ for Fe(110) [24]. This results in the smallest splitting for the IPS on Ni(111). However, in comparison to Fe(110), the IPS on Co(0001) lies higher in the supporting bulk band gap, thereby resulting in the highest exchange splitting of the IPS although the exchange splitting of the bulk band is smaller than for Fe(110). Consequently, the ratio of the bulk exchange splitting to the band gap is relevant for the IPS exchange splitting.

According to Eq. 3.18, the exchange splitting of the IPS is expected to scale with n^{-3} with increasing quantum number n. Hence, it is highest for the $n = 1$ IPS and decreases rapidly for higher order states. Its rapid decrease results from the fact, that the distance of the maximum of the probability density $|\psi_n(z)|^2$ from the surface increases with n. So only the lowest states have a significant overlap with the spin-dependent bulk potential.

3.3.2 Field states

A positive electric field modifies the electronic confinement potential in front of the surface (cf. Eq. 3.2) by a linear contribution, as depicted in Fig. 3.6(a). As a result, the IPS experience a Stark shift [123] and are transformed into so-called *field states* [108]: The electric field continuously shifts and expands the IPS spectrum, possibly pushing the states above the vacuum level, as depicted in Fig. 3.6(a). Hence, the Stark-shifted IPS no longer converge towards the vacuum level for $n \to \infty$. In conjunction with the Stark shift to higher energies a shift of the maximum of the probability density $|\psi_n(z)|^2$ towards the metal surface occurs. As a result, the overlap of the IPS wavefunctions with the bulk potential increases with increasing field strength, thereby reducing their electron lifetimes [22].

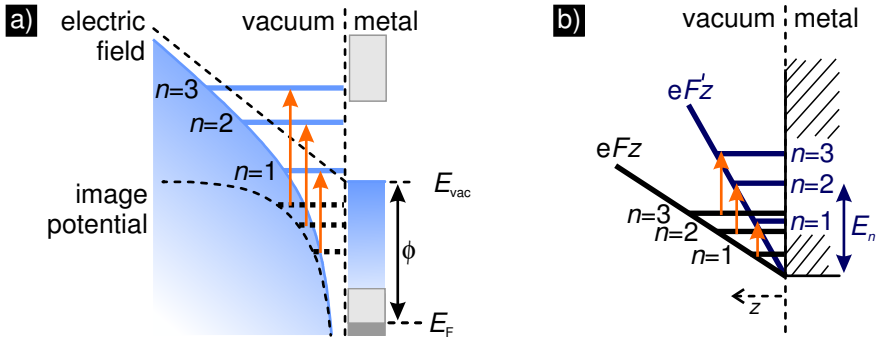

Figure 3.6: Field states. (**a**) The influence of a (positive) applied electric field on the surface barrier and the states confined within. The image-potential states are Stark-shifted to higher energies (indicated by arrows), transforming into field states. (**b**) A triangular potential well. Energetic positions E_n for the first three states are indicated. With increasing electric field F they are shifted to higher energies, whereas the absolute shift is larger for higher n states, as indicated by the arrows.

For the limiting case of large electrode separations and/or high voltages the confinement potential results in a triangular potential:

$$V(z) = \begin{cases} \infty & \text{for} \quad z \leq 0 \\ \mathrm{e}Fz & \text{for} \quad z > 0\,, \end{cases} \tag{3.19}$$

with the origin of the z-coordinate being located at the interface between the metal and the vacuum, as depicted in Fig. 3.6(b). Here, for simplicity an infinitely high potential barrier on the bulk side is assumed. The solutions of the Schrödinger equation for the quantum-mechanical problem of this triangular potential well are Airy functions, whose eigenvalues are given asymptotically for high n by [124]:

$$E_n = \left(\frac{\hbar^2}{2m}\right)^{\frac{1}{3}} \left[\frac{3\pi \mathrm{e}F}{2}(n - \frac{1}{4})\right]^{\frac{2}{3}} . \tag{3.20}$$

For the exact eigenvalues the expression $(n-\frac{1}{4})$ in Eq. 3.20 has to be replaced by a numerical factor. It is 0.7587, 1.7540, and 2.7575 for $n = 1$, 2, and 3, respectively. With an electric field strength $F = 2\,\mathrm{V/nm}$, the exact eigenvalue $E_{n=1}$ with the numerical factor 0.7587 is 730 meV, whereas the approximation with $(1-\frac{1}{4}) = 0.75$ results in 725 meV. Consequently, for $n = 1$ the deviation of the approximate eigenvalue to the exact one is less than 1 %, and gets even smaller for higher n. Hence, the approximation in Eq. 3.20 is enough good and can be used even for the low n states with $n = 1, 2, 3 \ldots$.

According to Eq. 3.20, the energies of the field states rise with increasing field strength F like $E_n \propto F^{\frac{2}{3}}$. The same scaling with $F^{\frac{2}{3}}$ is observed in more complex calculations including the image potential [125]. Additionally Eq. 3.20 shows that the state energy increases with order n like $E_n \propto n^{\frac{2}{3}}$. Hence, the absolute shift

in energy for a given field F is higher for states with high n than for states with small n, as depicted by the arrows in Fig. 3.6(b).

Within this simple model, the influence of the image potential can be compared to the influence of an applied electric field: The energies in a pure image potential develop with order n like n^{-2} (cf. Eq. 3.16), while they evolve with n like $n^{\frac{2}{3}}$ in a pure triangular electric field potential. Hence, for $n \longrightarrow \infty$ the influence of the electric field dominates and the image potential can indeed be neglected to a first approximation.

3.3.3 Spin-dependent field states

As discussed in Sec. 3.3.2, under the influence of an applied electric field the IPS experience a Stark-shift to higher energies and transform into field states. Their energetic shift is thereby larger the higher the electric field. Hence, the energetic position of the field states within the projected bulk band structure depends on the electric field strength. As shown in Sec. 3.3.1, above ferromagnetic surfaces the quantum defect $a^{\uparrow\downarrow}$ depends on the relative energetic position of the states within the band gap. Hence, $a^{\uparrow\downarrow}$ is expected to depend on the electric field strength and accordingly the exchange splitting (cf. Eq. 3.18) of the Stark-shifted IPS.

Hanuschkin *et al.* have performed first principle calculations to study the field-dependence of the spin-dependent binding energies and the corresponding exchange splitting of field states above Fe(110) [125]. The authors found, that the exchange splitting $\Delta E_n^{\uparrow\downarrow}$ does not exhibit the strongly decaying $1/n^3$-behavior of the field-free case (cf. Eq. 3.18). In contrast, it increases with increasing electric field strength. This is explained by the fact that the electric field pushes the maximum of the state density probability closer to the surface, thereby significantly increasing the overlap with the spin-dependent bulk crystal potential, which causes an increased exchange splitting.

Consequently, the exchange splitting of the field states may be tuned by an external electric field. So far, spin-dependent IPS have been almost exclusively investigated by spin-resolved photoemission experiments [25, 110]. Based on the photo-electric effect, these experiments analyze photoelectrons emitted from the IPS in front of a surface. As a consequence, the experimental setup do not allow the application of an external positive electric field, as it hinders the electron extraction. Owing to the small exchange splitting of the higher Rydberg states in the field-free case and the limited experimental energy resolution, generally only the first two states have been studied.

3.4 Field-emission resonances studied in an STM setup

The field emission current generated from a sharp metallic tip in front of a conducting surface has been used to image the surface topography by an instrument that was called the 'topografiner'. It was invented by Young *et al.* ten years before the invention of the STM [126, 127]. Here, the probe tip was piezoelectrically positioned close to the surface and a bias voltage was applied between the tip and the surface, as depicted in Fig. 2.1. The resulting field emission current was detected. As demonstrated in Sec. 3.2 the emission current depends on the electric field between the tip and the sample. A feedback control unit kept the current constant by adjusting the tip-sample displacement while raster-scanning laterally over the surface. This tip-sample distance regulation was then recorded to generate a three-dimensional image of the surface topography. Typical sample bias voltages applied in the topografiner were $\approx 50\,\mathrm{V}$ and tip-sample separations were in the range of 20 to 130 nm [127].

The field emission characteristics of the topografiner are well described by the Fowler-Nordheim theory, as well as a more general theoretical description conducted by Simmons [128]. As discussed in Sec. 3.2 the classical Fowler-Nordheim theory is based on calculating a transmission coefficient $D(W)$ for a particle of energy W traversing a triangular barrier that extends from z_1 to z_2, with z_1 and z_2 being the classical turning points (cf. Eq. 3.10), as depicted in Fig. 3.7(a). According to the JWKB approximation, the transmittivity of the barrier monotonically increases with increasing energy $W = eU$ of the tunneling electron and hence, with increasing sample bias voltage U.

In 1966 Gundlach [129] calculated the transmission coefficient for the *whole* barrier between the two electrodes, as shown in Fig. 3.7(a). Hence, he included the part of the potential barrier, where the energy W of the electrons is larger than their potential energy $V(z)$, thereby possessing positive kinetic energy. The exact treatment showed that the transmission coefficient $D(U)$ exhibits superposed periodic oscillations with sample bias U. It means that the electron emission probability oscillates as a function of energy W of the field-emitted electrons. These so-called *Gundlach oscillations* are caused by partial reflection and interference of the electron waves in the part of the barrier, where the electrons have positive kinetic energy:
After tunneling through the potential barrier ranging from z_1 to z_2, the electrons are accelerated towards the surface by the electric field. In this region between the electron's classical turning point z_2 and the anode surface, the electrons can be described by traveling waves. ling waves. Being partially reflected at the surface, they travel back into the vacuum, where they are reflected at z_2 and turn back towards the surface to be again partially reflected, and so on. Depending on the width and depth of the potential well, these multiple reflections can be

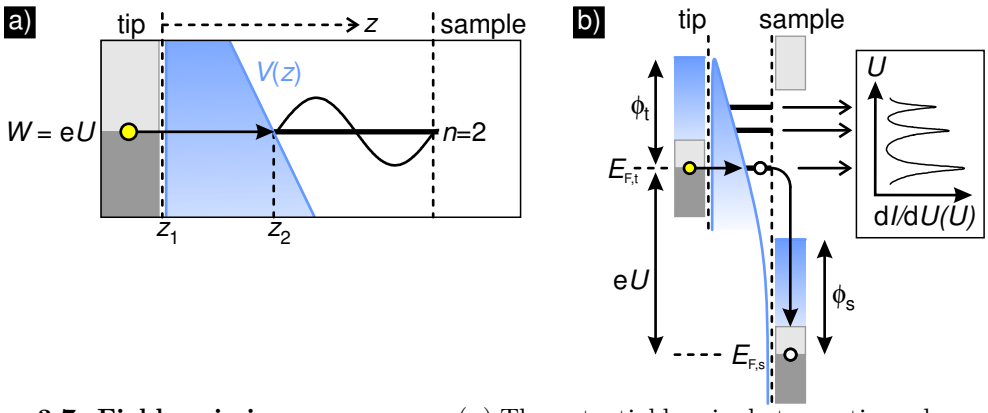

Figure 3.7: Field-emission resonances. (**a**) The potential barrier between tip and sample in field emission. Electrons tunnel through a potential barrier ranging from z_1 to z_2 and transmit afterwards a region where their energy W is higher than the potential energy $V(z)$. When the resonance condition for standing waves is fulfilled in this region, the field emission transmittivity increases. (**b**) Physical picture of resonantly injecting field-emitted electrons into a sample. Inset: When ramping the sample bias U the transmittivity and corresponding emission conductance $\mathrm{d}I/\mathrm{d}U(U)$ oscillates indicating the energetic positions of the field-emission resonance states. $E_{\mathrm{F,t}}$, $E_{\mathrm{F,s}}$: Fermi level and ϕ_{t}, ϕ_{s}: work function of tip and sample, respectively, U: sample bias voltage.

constructive or destructive. Hence, at certain electron energies $W = \mathrm{e}U$ and corresponding bias voltages U resonance conditions are fulfilled and standing waves are formed. These discrete energetic states associated with the standing waves correspond to the field states discussed in Sec. 3.3.2. As a result, they are also called *field-emission resonance* (FER) states [108, 130].

At the energetic positions of the FER states, the wavefunction in front of the collector surface is enhanced, leading to a larger overlap in the tunneling barrier with the wavefunctions of the emitter electrode, which results in an increase of the tunnel current. Gundlach calculated that the corresponding emission current $I(U)$ exhibited significant superposed oscillations.

In 1985, Binnig *et al.* and Becker *et al.* were able to experimentally detect oscillations in the field emission conductance $\mathrm{d}I/\mathrm{d}U$ as a function of sample bias voltage U using an STM setup [108, 131]. By applying bias voltages U slightly higher than the work function of the sample, the authors performed STM in the field emission mode. Here, electrons from the probe tip tunnel through a reduced potential barrier between the tip and the sample and then enter a region where they have a positive kinetic energy, as depicted in Fig. 3.7(b). The FER states in front of the sample then give rise to the observed Gundlach oscillations in the current $I(U)$ and conductance $\mathrm{d}I/\mathrm{d}U(U)$, as shown in the inset in Fig. 3.7(b). Each successive oscillation in $\mathrm{d}I/\mathrm{d}U(U)$ incorporates an additional FER state in the gap.

So far, we have only considered one-dimensional geometry. As discussed in Sec. 3.3, the discrete state in the z-direction corresponds to a two-dimensional free-electron band parallel to the surface. Considering all three dimensions, each peak in the $\mathrm{d}I/\mathrm{d}U(U)$-curve corresponds to the onset of a FER band. However, tunneling of electrons with $\left|k_{||}\right| > 0$ through a potential barrier is generally strongly suppressed [132]. Consequently, the contributions of electrons tunneling with $k_{||} \neq 0$ into FER states are expected to be negligible and only the one-dimensional description will be used in this thesis.

According to Eq. 3.20, the energetic distance of successive FER states decreases with energy and order n. Consequently, in the limiting case of high bias voltages and/or large tip-sample separations the FER spectrum is expected to be quasi-continuous. Compared to conventional field emission experiments, the STM setup provides the relatively low bias voltages and small tip-sample separations that are needed to resolve individual FER states. However, FER phenomena have been also observed in field ionization energy distributions [133], in metal-metal interfaces [134], and in semiconductor devices consisting of planar metal-insulator-semiconductor junctions [135, 136] and semiconductor-insulator-semiconductor heterostructures [137]. In contrast to experiments performed under ultra high vacuum conditions in an STM setup, the latter experiments suffer from a limited dynamic range due to nonadjustable emitter-collector spacing, and from a loss of coherence due to inhomogeneities in the gap spacing owing to ill-defined interfaces. In addition, the STM setup allows for a very local investigation of FER phenomena [130]: Since their first detection in the 1980's [108, 131, 138], FER states in an STM setup have been mainly used to study electron scattering properties of surfaces and interfaces [139, 140], local changes of surface work functions [141–144], hot electron dynamics [145–147] and quantum size effects above nanostructures [148, 149]. Recently, FER states on graphene [150, 151] and carbon nanotubes [152] have attracted attention. In 2001 it was demonstrated, that atomic-scale imaging of insulating diamond can be achieved in an STM setup by resonantly injecting electrons into FER states [153].

3.4.1 Spin-polarized scanning field emission microscopy

It was known since the 1960's that a magnetic field-emitter generates a spin-polarized field emission current (cf. Sec. 3.2.1). However, the combination with a magnetic collector for spin-polarized field emission conductance measurements has not been proven until 2007. Kubetzka *et al.* performed a first spin-polarized scanning field emission microscopy and spectroscopy study on a bulk-like Fe island on W(110) [23]. Such Fe islands are about 8 nm high and $200 - 300$ nm wide [154]. Hence, on top of these islands the surface is expected to be a *bulk-like* Fe(110) surface. The magnetic structure on the Fe island is a vortex [155]. This means that the magnetization rotates continuously from the surface plane to the sur-

face normal in the center. The authors were able to image this magnetic vortex with spin-polarized field-emitted electrons. They used a conventional SP-STM setup and applied a sample bias of 5 V, resulting in a spin-polarized field emission current.

The basic principle of the magnetic imaging technique is illustrated in Fig. 3.8. A magnetic tip is approached to nm distances from a magnetic surface and an electric field is generated between the tip and the sample by applying a sample bias voltage U, that is slightly higher than the work function ϕ_s of the sample. Spin-polarized electrons from the tip tunnel into the exchange-split FER states in front of the surface and afterwards they penetrate into the sample and relax to the Fermi level. Here, the emission conductance – mediated by the spin-dependent FER states – depends on the relative orientation of tip and sample magnetization, being high for the parallel and low for the antiparallel configuration.

The exchange-split FER states are expected to overlap energetically, as their intrinsic linewidths are larger than their exchange splitting [23, 115]. Hence, for a fixed energy both FER states are accessible by the respective spin-polarized electrons, as depicted in Fig. 3.8. Similar to the case of spin-polarized tunneling through a potential barrier ranging over the *full* region between the tip and the sample (cf. Sec. 2.3), for tunneling through a *reduced* barrier into the exchange-split FER states, the transmittivity and conductance depend on the number of initial and final states. For simplicity, we consider a tip with a spin-polarization of $P = 1$ (cf. Eq. 2.12), as depicted in Fig. 3.8. Here, only spin-up electrons are injected into the sample. In this case, the parallel alignment of the tip and the sample magnetization represents a highly efficient transmission junction. In contrast, in an antiparallel alignment a spin-up electron would not find any final spin-up state, if the sample electrode also had a spin-polarization of $P = 1$. Hence,

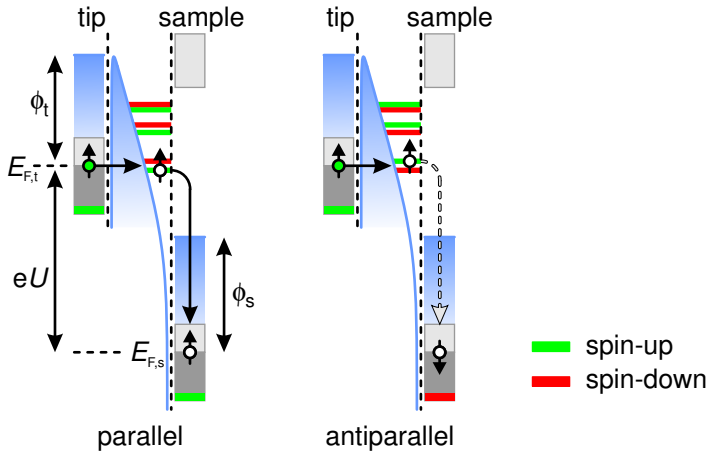

Figure 3.8: Resonantly injecting spin-polarized field-emitted electrons into a magnet. Physical picture for the parallel (left) or antiparallel (right) alignment of tip and sample magnetization.

it could not be injected into the sample. Only for a sample spin-polarization $P < 1$ can a spin-up electron penetrate into the magnet, either as minority spin of the sample or when flipping its spin magnetic moment by interacting with the sample's majority spins. As a result, the conductance in the case of an antiparallel alignment of tip and sample magnetization is expected to be significantly lower than for the parallel alignment.

Analog to SP-STM, scanning a magnetic tip over a surface with laterally varying magnetization results in a spin-polarized field emission conductance $\mathrm{d}I/\mathrm{d}U(x, y)$ that changes with tip position (x, y). The $\mathrm{d}I/\mathrm{d}U(x, y)$ signal can then be used for generating a magnetic map of the surface. This magnetic imaging technique will be called spin-polarized scanning field emission microscopy (SP-SFEM) in this thesis.

Chapter 4

Experimental Setup and Preparation

To perform SP-STM and SP-SFEM experiments of high reproducibility, the experimental setup has to ensure the preparation of clean and well-defined sample systems. Under ambient conditions, metallic tips and samples are covered instantaneously by water and insulating oxide layers, making SP-STM and SP-SFEM experiments impossible. At a vacuum base pressure of $p \approx 10^{-6}$ mbar, a clean surface is covered completely by adsorbates from the residual gas within a few sec [156]. To keep a surface clean for hours, the pressure has to be further reduced by orders of magnitude. Therefore, all experiments in this thesis are carried out under ultra-high vacuum (UHV) conditions with base pressures $p \leq 2\times10^{-10}$ mbar which permit the preparation of clean tips and samples and significantly reduce their subsequent contamination.

4.1 The UHV system

The experiments are performed in a UHV chamber system that is based on a commercial design of Oxford Instruments [157] (formerly known as Omicron [158]). It is shown in Fig. 4.1. The system consists of four chambers separated by manually operated UHV valves: (i) a load-lock with a dedicated pumping system, that allows the transfer of a tip or a sample into the system, (ii) a chamber for annealing samples under O_2 atmosphere, (iii) a chamber for the preparation of tips and samples, and (iv) an analysis chamber that is equipped with low-energy electron diffraction (LEED) and Auger electron spectroscopy (AES). A satellite of the analysis chamber contains the variable temperature STM for SP-STM and SP-SFEM investigations. In each of the two main chambers (the preparation and analysis chamber) a base pressure below 2×10^{-10} mbar is realized by an ion-pump and a titanium sublimation pump. Tips and samples are transferred between the chambers using rotatable linear manipulators and a wobble stick.

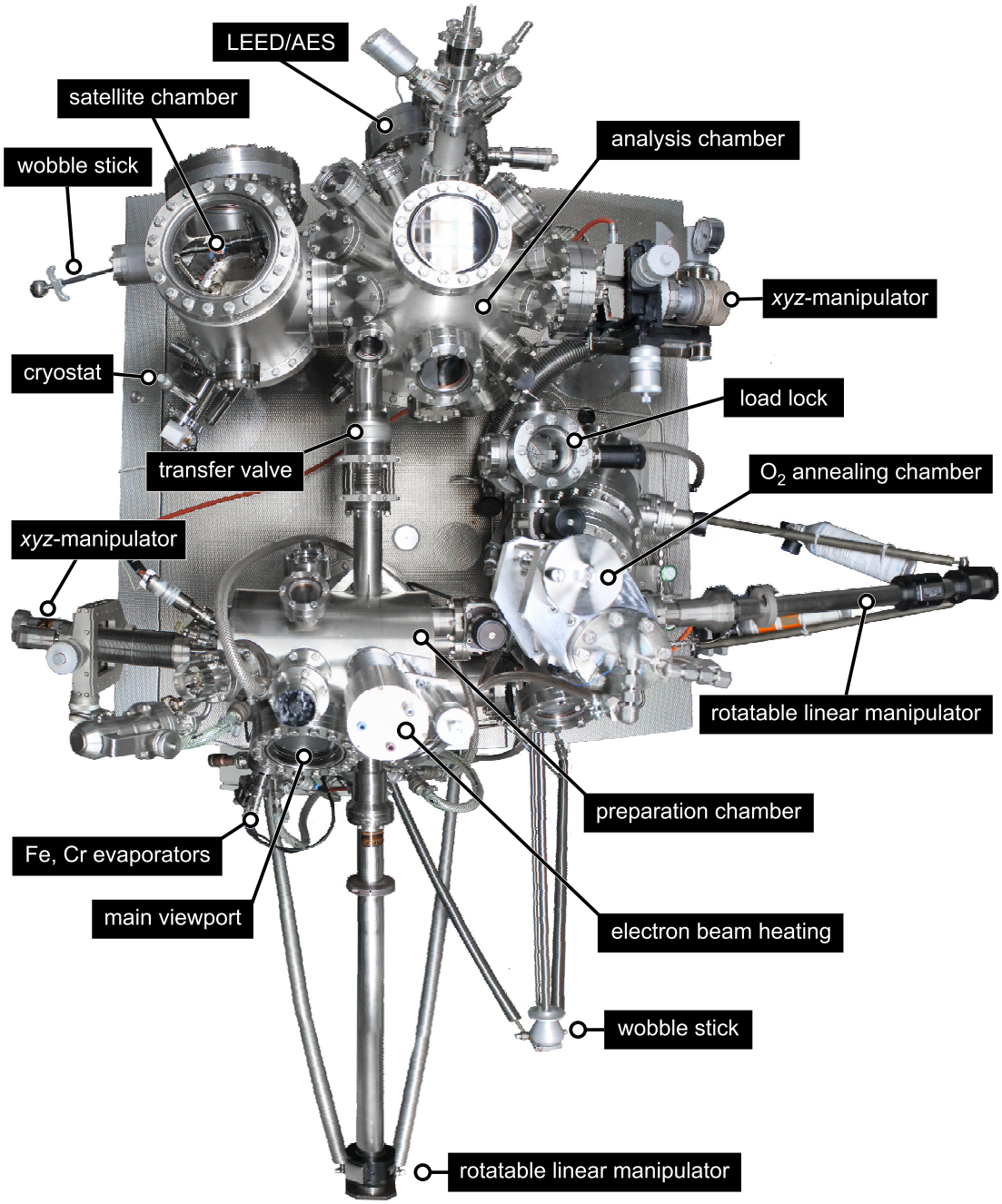

Figure 4.1: Fish-eye photograph of the UHV chamber system. It consists of four chambers separated by UHV valves. The main facilities used in this thesis are denoted.

An electron beam heating, Cr and Fe evaporators, an xyz-manipulator equipped with a resistive heater, and a O_2 dosing valve are used for the preparation of tips and samples. All these devices are contained in the preparation chamber, as shown

in Fig. 4.1. The home-built electron beam heater is used to heat tips and samples to temperatures up to $T = 2400\,\mathrm{K}$ by electron bombardment. Here, two parallel tungsten wires serve as a stage for tip and sample holders. The wire stage can be connected to a high voltage ($U_{\mathrm{HV}} < 2000\,\mathrm{V}$), and a tungsten filament powered by a dc current ($I_{\mathrm{fil}} \approx 3.5\,\mathrm{A}$) serves as a cathode. The electrons thermally emitted from the heated filament are accelerated by the high voltage towards the tip or sample holder. This electron bombardment leads to a heating of tip or sample, and the temperature is measured by an infrared pyrometer through a viewport.

For material deposition, tip and sample are positioned with an xyz-manipulator in front of electron beam evaporators equipped with flux monitors. The evaporator material is heated by electron bombardment from a tungsten filament coated with Thorium which reduces the work function of the filament and increases the emissivity. Fe was evaporated at a rate of 1.2 ML/minute from a wire and Cr was evaporated from a crucible at 9 ML/min. To avoid heating the surroundings which may result in impurities in the beam and the deposited film the housings of the evaporators have water cooled copper shields. During or after material deposition, the film on the tip or the sample can be annealed by means of a resistive heater in the xyz-manipulator. Temperatures ranging from room temperature up to $T = 1150\,\mathrm{K}$, measured indirectly with a chromel/alumel thermocouple, can be chosen.

4.2 The variable-temperature scanning tunneling microscope

The variable-temperature STM (VT-STM) is specifically designed for the investigation of temperature-dependent magnetic phenomena by SP-STM. It allows for operation from $T = 20$ to $300\,\mathrm{K}$. A major difference to standard variable-temperature instruments is, that the whole microscope including *both* the tip and the sample is cooled, which results in a reduced thermal drift and an improved energy resolution for spectroscopy at low temperatures. A larger variety of magnetic materials can be used for the thin-film coating of SP-STM tips (cf. Sec. 4.3), since Curie- or Néel-temperatures of many ultra-thin films are below room temperature. The microscope is manufactured from materials which have to fulfill a compromise of several requirements, for example similar thermal expansion coefficients and UHV compatibility. A detailed description of the VT-STM can be found in the Ph.D. thesis of Torben Hänke [159].

The microscope design including a fast tip exchange mechanism is based on the developments by D. Haude [160]. Photographs of the STM are shown in Fig. 4.2 and Fig. 4.3 shows technical drawings of the instrument.

For an isolation from mechanical noise sources, the instrument is mounted on a low resonance frequency damping stage. It consists of a massive copper base

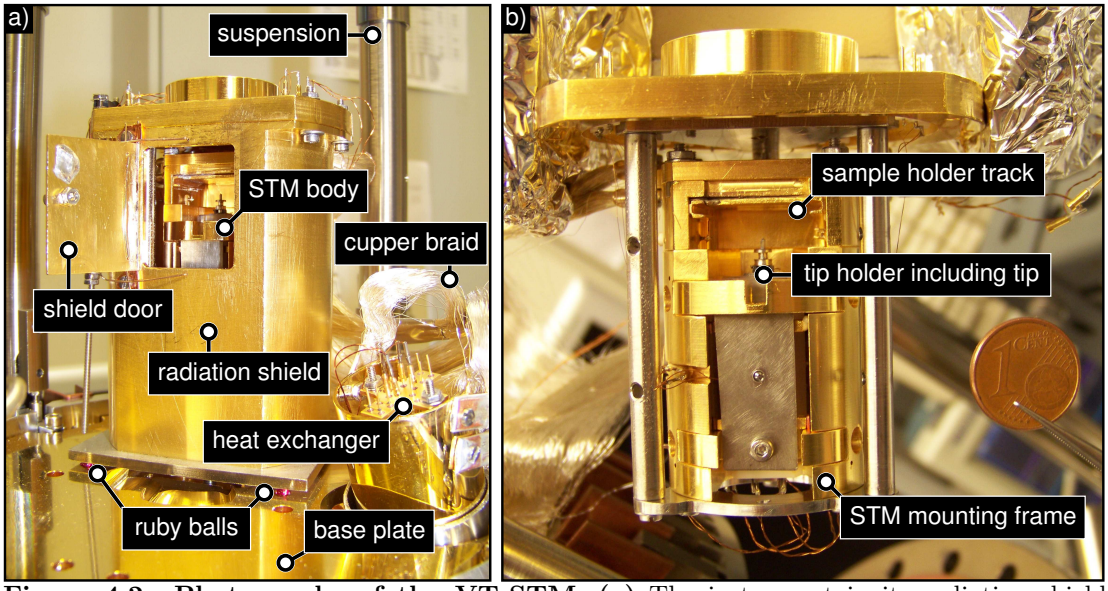

Figure 4.2: Photographs of the VT-STM. (a) The instrument in its radiation shield mounted on top of the base plate. **(b)** The STM body. The one euro cent coin gives a notion of the instrument's size.

plate that is suspended from four metal springs and equipped with an eddy current damping. Along with a high resonance frequency of the STM, this design results in an effective filter against mechanical noise.

For a protection against thermal radiation of the surroundings, the STM is mounted within a shield. Small ruby balls are clamped between the base plate and the STM housing (cf. Fig. 4.2) as well as between the microscope and the top of the radiation shield (cf. Fig. 4.3) thereby realizing point contacts with minimal thermal transmission.

A door within the radiation shield gives access to the microscope for inserting the tip or the sample by means of a wobble stick. The sample is mounted upside down in the sample holder and the tip approaches the sample from the bottom. For the coarse approach a stepper motor is used. The tip is mechanically clamped inside a piezoelectric tube scanner which is glued into a sapphire prism of the coarse approach mechanism. Both the stepper motor for the coarse approach as well as the tube scanner for the precise tip positioning during experiments are based on the inverse piezoelectric effect: When applying a voltage to a piezoelectric material, it deforms. A piezoelectric tube scanner has four quadrant electrodes (x_+, y_+, x_-, y_-) on the outside and a connection on the inside (z). Applying a dc voltage between the inner and all of the outer electrodes, results in a contraction or elongation of the whole tube scanner depending on the polarity. This effect is used to move the probe tip in the z direction. When the voltage is applied between opposite outer electrodes (e.g. x_+ and x_-), the piezoelectric

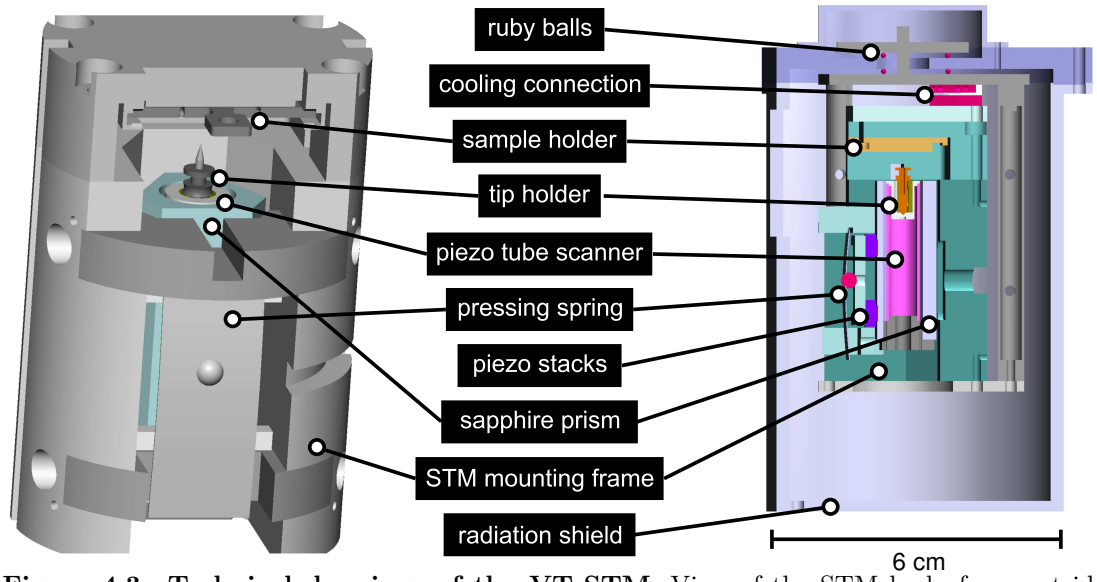

Figure 4.3: Technical drawings of the VT-STM. View of the STM body from outside (left) and cross-sectional view of the instrument in its radiation shield (right).

material is elongated at one electrode and contracts at the other, which results in a bending of the tube. By this means, the tip is moved along the x direction. The same principle is used to move the tip along the y direction.

As the piezo tube usually has a z range well below a micrometer, a coarse approach of the probe tip is needed. In this setup, a stepper motor is realized in the *walker* design [161]. It consists of six shear piezos glued on the inside of the microscope body, holding a sapphire prism, in which the tube scanner for the tip is glued (cf. Fig. 4.3). When applying an asymmetrical saw-tooth voltage to the piezos a so-called stick-slip motion is achieved. During the slow voltage slope the piezos shear slowly and the prism follows the motion (*stick*). On the steep voltage slope the piezos relax too fast for the prism to follow, and the piezos *slip* along its surface. Here, the amplitude and frequency of the saw-tooth voltage determines step size and travel time. In this particular setup the voltage ramp with an amplitude of $\pm 120\,\mathrm{V}$ is repeated at a frequency of 0.5 to 1 kHz.

The maximum travel realized by this particular stepper motor is about 20 mm. This long travel allows for a fast in-situ exchange mechanism of the probe tip. The empty tube scanner is retracted downwards by the coarse approach allowing for the insertion of the tip-holder containing the tip with a specially designed shuttle into the sample holder track. Then, the tube scanner is moved upwards again, thereby gradually enclosing the tip-holder with the tip. When the tip-holder is enclosed by the tube scanner, the shuttle is removed and the sample holder track is free again for the prepared sample.

To perform SP-STM and SP-SFEM measurements at variable currents, a commercial current-to-voltage amplifier (FEMTO DLPCA-200) [162] with variable gain is used. In this thesis currents of up to $I_{\max} \in \{100\,\mathrm{nA},\ 1\,\mu\mathrm{A}\}$ were used with amplification ranges between $10^8\,\mathrm{V/A}$ (for low current) and $10^7\,\mathrm{V/A}$ (for high current).

Cooling the VT-STM is realized by a commercial liquid He flow cryostat from the CryoVac company [163]. The temperature is controlled by two manually operated mechanical valves regulating the amount of liquid He flowing through the cryostat. The He flows through a heat exchanger which is thermally connected to the STM by copper braids (cf. Fig. 4.2(a)). These braids consist of about 800 silver-plated copper wires, each of them with a diameter of $\approx 0.05\,\mathrm{mm}$. They are fed through small openings in the radiation shield and are screwed to the microscope. Since they are highly flexible the transmission of vibrations to the STM is prevented. In addition, the radiation shield surrounding the STM is cooled via a second copper braid by the exhaust from the flow cryostat. At the heat exchanger the temperature T_{ex} is measured with a Si-diode and stabilized by a PID-temperature controller. The STM temperature T_{STM} is measured with a GaAs/GaAlAs diode mounted close to the sample holder on the STM body. T_{STM} is slightly higher than the heat exchanger temperature ($T_{\mathrm{STM}} - T_{\mathrm{ex}} \approx 10 - 15\,\mathrm{K}$). When cooling from room temperature the lowest base temperature of approximately 18 K at the sample is reached within two hours [164].

4.3 Preparation of conventional probe tips

An essential requirement for SP-STM as well as SP-SFEM measurements is a magnetic probe tip generating a spin-polarized current. The most common way to produce an electronically and magnetically stable probe tip for SP-STM is the preparation of a magnetic thin-film tip. Here, a non-magnetic tip is coated with a magnetic material which is either ferromagnetic (e.g. Fe, Gd) or antiferromagnetic (e.g. Cr). For studies on ferromagnetic samples generally antiferromagnetic tips are preferred since the absence of tip stray fields avoids unwanted magnetic interactions between the tip and the sample [165].

The magnetic film thickness can determine whether the tip is sensitive to in-plane or out-of-plane surface magnetization [166]. For example, 25-45 atomic layers of Cr deposited onto a W tip result in an out-of-plane magnetic sensitivity, whereas thicker Cr films of several 100 atomic layers give in-plane sensitivity. In this thesis, for the combined SP-STM and SP-SFEM experiments, an in-plane sensitive magnetic probe tip without any significant stray field is required. Hence, I prepared W tips coated with an antiferromagnetic Cr film of at least 100 atomic layers.

W tips were prepared *ex situ* by electrochemical ac-etching of a polycrystalline tungsten wire (ø 0.75 mm) in a sodium hydroxide solution (8g NaOH per 100 ml H_2O, $U_{\text{etch}} = 5\,\text{V}$). Next, a tip was clamped in a tip holder and transferred inside the tip shuttle into the UHV preparation chamber. Under UHV conditions, the tip is heated for a few seconds to a temperature of $T = 1500\,\text{K}$ by means of electron bombardment to remove the oxide layer on the tip. The short heating also improves the adhesion of the magnetic films. SEM images show that the heating melts the apex of the tip which becomes round with a radius on the order of 500 nm [167].

A few hundred atomic layers of chromium are deposited on the clean W tip, which is subsequently annealed at $T = 550\,\text{K}$ for $t = 240\,\text{s}$, resulting in a thin stable magnetic film on the tip. In the STM, the tip can be further prepared when in tunneling contact with the sample. For instance, short bias voltage pulses of up to 10 Volt can be applied, leading to atomic rearrangements at the apex of the tip.

4.4 Preparation of W(110) substrates

The W(110) surface is a suitable substrate for the preparation of thin films and epitaxially grown nanostructures since intermixing is often negligible and adlayers can be easily removed after the experiment by thermal desorption. Its high melting point is beneficial in terms of cleaning and preparing thin-film samples. In this thesis, all experiments were performed on the W(110) surface serving as substrate.

The substrate preparation was performed *in situ* in the preparation chamber at a base pressure of $p \leq 2\times10^{-10}\,\text{mbar}$. The W(110) surface was cleaned by cycles of annealing ($T \approx 1500\,\text{K}$ for about 30 min) in O_2 atmosphere and a subsequent high-temperature flash ($T \approx 2300\,\text{K}$ for 15 s) [168]. Here, the oxygen partial pressure is gradually reduced from $p_{O_2} = 2 \times 10^{-6}\,\text{mbar}$ in the first annealing cycle to $p_{O_2} = 4 \times 10^{-8}\,\text{mbar}$ in the last cycle. During the annealing process carbon (the major impurity in tungsten) segregates to the surface. Exposed to oxygen at the surface, it reacts to CO and CO_2 and desorbs. As a result, a carbon depletion layer is formed below the surface. Simultaneously, the annealing under O_2 atmosphere leads to an oxidation of the tungsten surface. The tungsten oxides are removed by thermal desorption during the high temperature flash.

An STM topography image of the bare W(110) surface as prepared for my experiments is shown in Fig. 4.4(a). Several tungsten terraces separated by monatomic step edges running along the [001] direction can be seen. The simultaneously recorded $\mathrm{d}I/\mathrm{d}U$ map is shown in Fig. 4.4(b). Here, residual impurities on the surface are more visible. On the terraces, $N_{\text{impurity}} \approx 300$ adatoms can be found. Calculating the overall number of W atoms $N_{\text{W}} \approx 1.7 \cdot 10^5$ in this surface area results in an impurity density below 0.2 %.

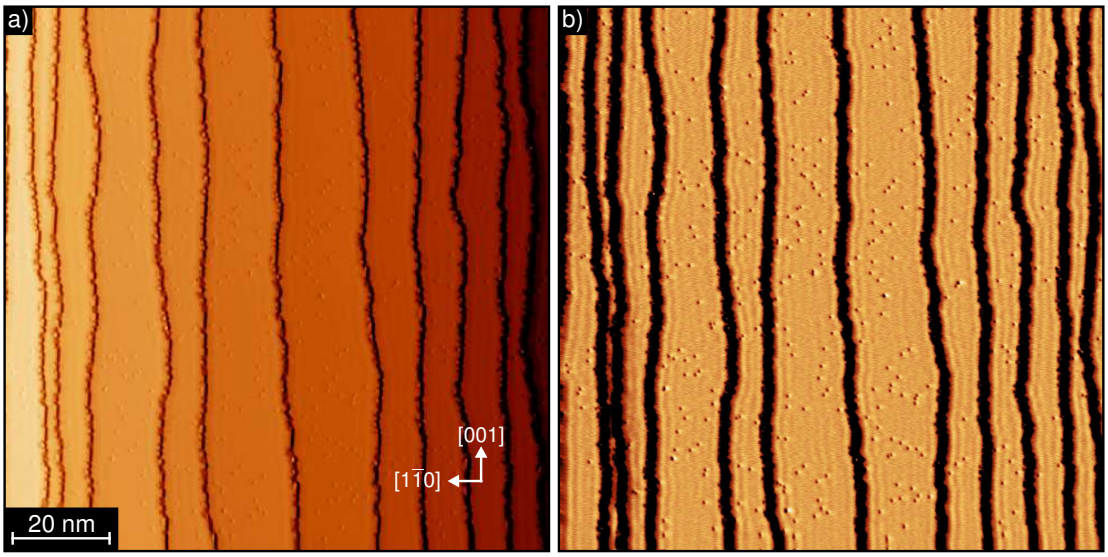

Figure 4.4: The W(110) substrate (a) STM topography image and **(b)** simultaneously recorded $\mathrm{d}I/\mathrm{d}U$ map of a typical W(110) surface as used as substrate in this thesis. $I = 2\,\mathrm{nA}$, $U = -200\,\mathrm{mV}$, $T = 45\,\mathrm{K}$, W-tip.

On closer inspection Fig. 4.4(b) reveals periodic variations of the $\mathrm{d}I/\mathrm{d}U$ signal mainly along the step edges. This indicates a spatial modulation of the local density of states (cf. Sec. 2.2.2). A combined study of tunneling spectroscopy measurements and density functional theory calculations has revealed that this interference pattern only appears on very clean W(110) surfaces as it originates from a surface resonance band of $p_z d_{xz}$-type character, which is absent on contaminated surfaces [168].

Once a clean crystal has been achieved using this procedure, it is usually sufficient to flash the crystal between sample preparations to obtain a clean substrate (at least when iron has been deposited). However, in the course of time the substrate accumulates impurities that may originate e.g. from inside the bulk segregating to the surface, from the experimental environment, or the deposited material. When a critical impurity concentration of $\gtrsim 1\,\%$ is reached, the surface resonance vanishes, and the W(110) surface has to be cleaned in oxygen again.

Chapter 5

Fe/W(110) at low coverages

Iron on tungsten exhibits a rich variety of structural, electronic, and magnetic properties, especially in the low coverage regime. Being extensively studied both experimentally as well as theoretically, Fe/W(110) has become a very well-characterized system. Hence, it is a suitable reference system to investigate physical aspects that go beyond material-dependent structural, electronic, and magnetic properties. This chapter focuses on aspects of the morphology and magnetic properties of the Fe/W(110) monolayer and double layer.

5.1 Growth and magnetism

The topographic structure of Fe on W(110) depends on diverse parameters such as the Fe coverage, the growth temperature, and the miscut of the W(110) surface.

Both bulk iron and tungsten have a body-centered cubic crystal structure with lattice constants $a_{\mathrm{Fe}} = 2.867\,\text{Å}$ and $a_{\mathrm{W}} = 3.165\,\text{Å}$, respectively [169]. Hence, the crystallographic unit cell of the (110)-surface is a rectangle with two atoms, as illustrated in Fig. 5.1(a). Despite the large lattice mismatch of $(a_{\mathrm{W}} - a_{\mathrm{Fe}})/a_{\mathrm{W}} = 9.4\,\%$ that is expected to induce considerable strain in the film, Fe grows pseudomorphically in the monolayer (ML) regime [170], i.e. it reproduces the surface lattice structure of the underlying W(110) substrate (see Fig. 5.1(b)).

The growth mode strongly depends on the substrate temperature. At room temperature the iron forms ML islands and patches on the tungsten terraces and decorates step edges, while coalescence is inhibited up to a coverage of ≈ 0.6 atomic layers [171, 172]. According to Ref. [172] the strain in the islands and patches induced by the large lattice mismatch can be lowered by an inward bending of the island rim atoms. However, coalescence would reduce this possibility of stress-lowering and hence it is avoided up to a critical coverage. At higher coverages, bridges emerge between adjacent islands until a closed ML film is formed at a nominal coverage of 1 atomic layer.

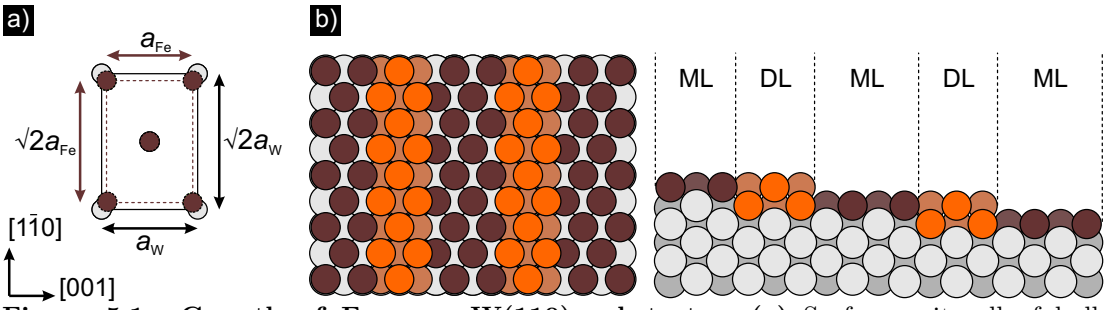

Figure 5.1: Growth of Fe on a W(110) substrate. **(a)** Surface unit cell of bulk Fe(110) (brown) and W(110) (grey). The large lattice mismatch induces stress in the pseudomorphic growing Fe film on W(110). **(b)** Sketch of the atomic coordination of a step-flow grown Fe film on three terraces of a W(110) (grey) surface with a coverage of one (brown, ML) and two (orange, DL) Fe layers in a top-view (left) and a side view (right).

At elevated temperatures iron stripes emerge along the tungsten step edges in a step-flow growth mode [172, 173] until a closed ML film is formed. The first ML is always completed fully before the second atomic layer starts to grow. This wetting layer behavior arises from the free surface energy of the substrate (2.9 J/m^2 for W) being larger than that of the film (2.0 J/m^2 for Fe), increased by the interface energy [174, 175]. Hence, it is energetically favorable for an iron atom to adsorb on the substrate rather than on the first ML. The wetting ML is stable up to a temperature of $T = 1100$ K when the iron starts to desorb from the substrate [174].

The growth behavior of the second atomic layer of Fe on W(110) is similar to that of the ML. At room temperature, the iron decorates step edges and forms free second-layer islands that are preferentially elongated along the [001]-direction [172, 176, 177]. With increasing coverage the island sizes increase, and finally the islands coalesce into a network.

At elevated substrate temperatures, double layer (DL) stripes emerge at the step edges, that are separated by ML stripes [178], as shown in Fig. 5.1(b). Growing preferentially along the crystallographic [001]-direction, the shape of the DL stripes depends on the orientation of the step edges: along the [001]-direction step-flow growth of well-defined stripes aligned along the step edges occurs [179, 180], whereas the stripe edges become frayed for step edges along [1$\bar{1}$0] direction [181, 182].

The second layer grows pseudomorphic, resulting in a closed double-layer film at a nominal coverage of 2 atomic layers with sporadic dislocation lines running along the [001]-direction to relieve the strain in the film [172].

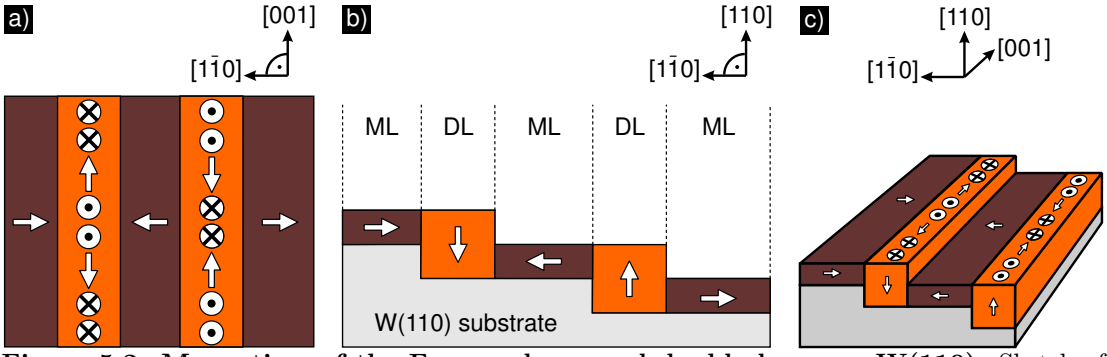

Figure 5.2: Magnetism of the Fe monolayer and double layer on W(110). Sketch of the magnetic configuration of the Fe monolayer (brown, ML) and double layer (orange, DL) on a W(110) substrate (grey) in a top-view **(a)** and a side view **(b)**. The ML consists of magnetic domains with the easy axis lying in the surface plane and pointing in the [1$\bar{1}$0]-direction. The DL exhibits an inhomogeneous cycloidal spin spiral with domains pointing out of the surface plane (and in the surface plane, respectively) and domain walls rotating around the [1$\bar{1}$0]-direction, lying locally in the [001]-direction. (c) Three-dimensional sketch: Within the ML domains, the DL domains, and domain walls magnetization directions spanning the three-dimensional space are provided, as indicated by the arrows.

Magnetism

The sample system Fe/W(110) exhibits a variety of interesting magnetic properties, which are strongly connected to the temperature- and coverage-driven morphology, governed by lattice mismatch and relaxation with increasing film thickness [155, 165, 174, 178, 181–188].

The magnetization of the iron ML is driven by its uniaxial anisotropy with the easy axis of magnetization pointing along the [1$\bar{1}$0]-direction [189], as depicted in Fig. 5.2. Its in-plane ferromagnetic order is stable up to a Curie-temperature of $T_c = 225\,\mathrm{K}$ [171, 174]. Adjacent antiparallel magnetized ML domains are separated by domain walls whose widths presumably depend on the impurity level of the film. Whereas typical widths of $w_{ML} \approx 2\,\mathrm{nm}$ are observed on monolayers of high cleanliness [190], atomic-scale domain walls with widths of only $w_{ML} \approx 0.6\,\mathrm{nm}$ are observed on films with a considerable impurity density [191]. On narrow substrate terraces (typically about 10 nm) the magnetic domains of adjacent ML stripes are found to couple antiparallel [173].

In contrast to the ML, the iron DL exhibits a uniaxial anisotropy with the magnetic easy axis pointing out of the film plane, i.e. in the [110]-direction [178]. Its magnetization structure is a cycloidal spin-spiral [182]. The magnetization rotates around the [1$\bar{1}$0]-direction, lying locally in the [001]-direction, as depicted in Fig. 5.2. A unique sense of rotation was observed that is attributed to the influence of the Dzyaloshinskii-Moriya interaction [165, 182, 192]. As the spin spiral is inhomogeneous, antiparallel magnetized out-of-plane 'domains' are separated

by Néel-type 'domain walls' rotating through the [001]-direction, as depicted in Fig. 5.2. The domain wall width is found to be $w_{\mathrm{DL}} \approx 7\,\mathrm{nm}$ [193].

Consequently, the system with iron mono- and double layers exhibits magnetization directions that span the three-dimensional space, as indicated in Fig. 5.2(c).

5.2 Thermally switching iron nanomagnets

Evaporating nominally 0.14 atomic layers of iron onto a clean W(110) substrate held at room temperature leads to the formation of pseudomorphically grown ML nanoislands with typical diameters between 2 nm and 6 nm, consisting of about 30 to 100 atoms. An SP-STM topography image of an ensemble of iron nanomagnets on a flat W(110) substrate at $T = 41\,\mathrm{K}$ is shown in Fig. 5.3(a). Simultaneously to the constant current topography image, a small ac modulation voltage ($U_{\mathrm{mod}} = 40\,\mathrm{mV}$, $f = 4.333\,\mathrm{kHz}$) was added to the applied bias voltage U in order to record the spatially-resolved differential conductance $dI/dU(\vec{r})$ using the lock-in technique. This map shown in Fig. 5.3(b) is correlated to the magnetization of the sample, since $dI/dU(\vec{r})$ scales with the cosine of the angle between the magnetization of the tip and the sample at the location $\vec{r}$ (see Chap. 2). It reveals two stages of contrast on the iron islands (dark or bright). These Fe/W(110) nanomagnets are known to be monodomain particles with a uniaxial anisotropy

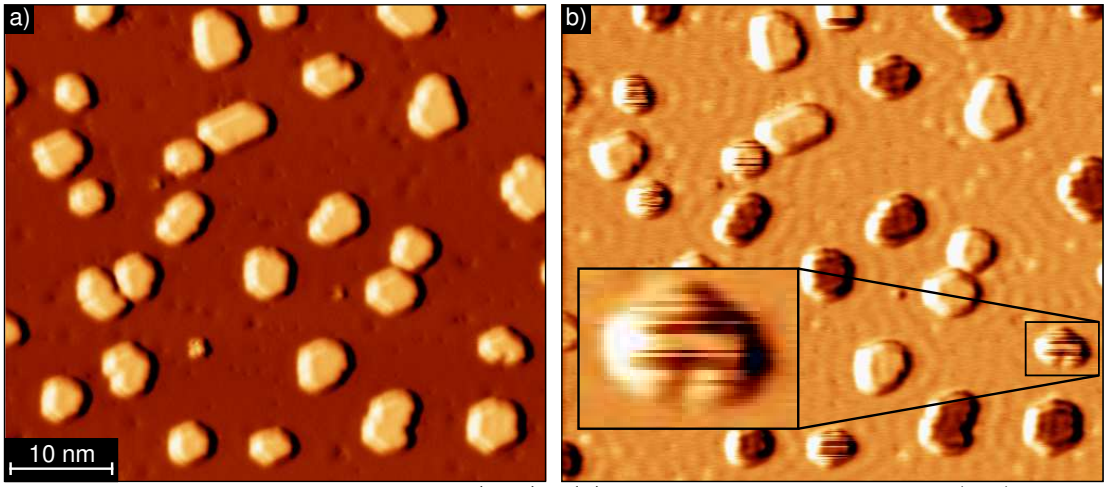

Figure 5.3: Fe nanomagnets on W(110). **(a)** SP-STM topography of a W(110) surface decorated with iron monolayer islands. **(b)** Corresponding magnetic $\mathrm{d}I/\mathrm{d}U$ map. A bright or dark signal on the nanomagnet represents a parallel or antiparallel magnetization with respect to the tip magnetization. Most of the nanomagnets appear homogeneously bright or dark, respectively, indicating stable magnetization. Smaller nanomagnets exhibit a characteristic stripe pattern (see inset) due to thermally-induced magnetization switching when imaged line by line. The fast scanning direction of the tip is horizontal. $I = 2\,\mathrm{nA}$, $U = -200\,\mathrm{mV}$, $T = 41\,\mathrm{K}$, Cr/W-tip.

lying in the surface plane [190]. Consequently, imaged with an in-plane sensitive Cr/W-tip, the dark and bright $\mathrm{d}I/\mathrm{d}U$ signal reflects the two possible magnetic configurations of the nanoislands with respect to the tip magnetization. A standing wave pattern can be observed between the nanomagnets in the $\mathrm{d}I/\mathrm{d}U$ map. This non-magnetic feature is due to a surface resonance band only observable on extremely pure tungsten substrates (see Chap. 4). In the magnetic $\mathrm{d}I/\mathrm{d}U$ map shown in Fig. 5.3(b), most of the nanomagnets appear homogeneously bright or dark. This indicates that the magnetic configuration is stable during scanning. In contrast, the smaller nanomagnets are not completely bright or dark, but exhibit a characteristic stripe pattern: As the SP-STM image is recorded line by line with the fast scanning direction along the horizontal, the small nanomagnets appear bright for some lines and dark for others in the $\mathrm{d}I/\mathrm{d}U$ map. Consequently, the $\mathrm{d}I/\mathrm{d}U$ signal on the small nanomagnets changes with time. As the $\mathrm{d}I/\mathrm{d}U$ signal reflects the magnetic orientation relative to the stable tip magnetization, the stripe pattern indicates thermally-activated magnetization switching of the nanomagnets [33, 194]. Note, that the nanomagnets are in the single domain state between two consecutive switching events. As the switching frequency depends on the island size and shape [190, 195–198], each nanomagnet exhibits its own characteristic stripe widths: a pattern of multiple, thin stripes indicates a higher switching frequency than a pattern with only a few very broad stripes.

It has been shown that the superparamagnetic switching behavior of these Fe/W(110) nanomagnets can be described by the so-called macrospin model, as illustrated in Fig. 5.4. As demonstrated theoretically [199, 200] and verified experimentally [201], the model is the adequate to describe the intrinsic switching behavior of a superparamagnetic particle with a uniaxial anisotropy at a given temperature T. Here, the particle magnetization has to overcome an energy barrier E_b to reverse its orientation. All magnetic moments inside the particle rotate

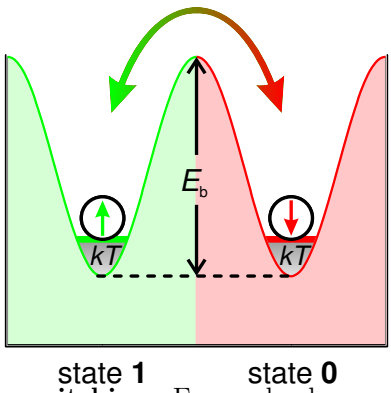

Figure 5.4: Superparamagnetic switching. Energy landscape of a magnet with uniaxial anisotropy. Due to thermal agitation at temperature T, the magnetization may overcome the effective activation barrier E_b between the two states **1** and **0**.

coherently, thereby behaving like one giant spin, and E_b is given by the total magnetic anisotropy of the particle. The mean lifetime $\bar{\tau}$ between two consecutive switching events as a function of T is then given by

$$\bar{\tau} = \nu_0^{-1} \exp\left(\frac{E_\mathrm{b}}{k_\mathrm{B}T}\right), \tag{5.1}$$

with ν_0 being the attempt frequency and k_B the Boltzmann constant. The two possible magnetization orientations are labeled state **1** and state **0**, respectively. Temperature-dependent SP-STM studies on individual Fe/W(110) nanoislands revealed that the magnetization reversal is realized by nucleation and propagation of a domain wall rather than by coherent rotation [190]. However, the macrospin ansatz has been shown to describe the switching behavior adequately as long as E_b is interpreted as the effective activation energy barrier for magnetization reversal.

According to Ref. [190] E_b and ν_0 strongly depend on the size and shape of the nanomagnet, resulting in different switching frequencies and therefore different stripe patterns for different nanomagnets at the same temperature, as observed in Fig. 5.3(b).

Chapter 6

Bulk Cr Tips with Full Spatial Magnetic Sensitivity

In spin-polarized scanning tunneling microscopy, biasing a magnetic probe tip generates a spin-polarized tunnel current that depends on the relative orientation between the tip and the sample magnetization (see Sec. 2.3). Hence, probing a surface of spatially varying magnetization with a fixed tip magnetization allows for generating magnetic maps of the surface. As described in Sec. 4.3, magnetic probe tips are conventionally realized by coating a non-magnetic tip with a magnetic material which is either ferromagnetic or antiferromagnetic. A disadvantage of magnetic thin-film tips is their requirement of *in situ* preparation and a tip exchange mechanism in the microscope. Recent efforts focus on tips made of bulk magnetic material [26–30], because they do not need extensive preparation procedures.

Generally, antiferromagnetic probe tips are preferred since they are expected to have no stray field that may interact with the sample magnetization [165]. One promising tip bulk material is chromium (Cr), being antiferromagnetic at temperatures below $T_{\mathrm{N}} = 311\,\mathrm{K}$ [31].

Whereas it is known that bulk Cr tips allow for atomic resolution as proved on the Si(111) 7×7 surface [202], only recently magnetic contrast was achieved using such tips on a Cr(001) surface [30]. As Cr(001) is a topological antiferromagnet with the easy axis of magnetization lying in the surface plane [203, 204], it does not permit a complete tip characterization, including the out-of-plane component of surface magnetization.

As shown in Chap. 5, the well-known system of the combined Fe mono- and double layer on W(110) provides magnetization directions, that span the three-dimensional space, and hence is suitable for the magnetic characterization of bulk Cr tips. After a short description of the preparation procedure, this chapter presents the magnetic characterization of bulk Cr tips on the system of 1.5 monolayers of Fe/W(110) using SP-STM at low temperatures.

6.1 Preparation

A polycrystalline Cr bar with a cross section of approximately $(1 \times 1)\,\mathrm{mm}^2$ was cut from a 99.99 % Cr foil [30]. As illustrated in Fig. 6.1(a), the Cr rod and a carbon cathode were then dipped into an etching solution (i.e. NaOH or HCl) and a 5 V dc voltage was applied. The Cr rod serves as an anode, is electrochemically etched and a tip is formed.

The rod was first etched for 10 to 20 minutes to achieve an approximately circular cross section and to reduce the diameter, as depicted in Fig. 6.1(b), so that the probe tip fits into the tip holder. Cleaning in an ultrasonic bath of distilled water and isopropanol removes the chemical debris [29, 205].

The actual tip was etched using the so-called drop-off method [29, 206], as shown in Fig. 6.1(c): the Cr rod is covered by some insulating material (i.e. polymer tubes or Parafilm®), thereby physically restricting the active etching region to the meniscus [29]. Here, the etching process induces a constriction that becomes more and more pronounced within a few minutes until the lower part of the Cr rod drops off under the influence of its own weight. This part is used as probe tip. Its macroscopic shape is thereby strongly dependent on the meniscus, specifically on the height of the wetting area of the etchant on the rod [206].

After removal of the protecting material and rinsing with distilled water and isopropanol, the fabricated tip is clamped into a tip holder and inserted into the UHV chamber. Finally, inside the VT-STM, a few short voltage pulses up to 10 V are applied between the tip and the sample to remove the Cr oxides. These short

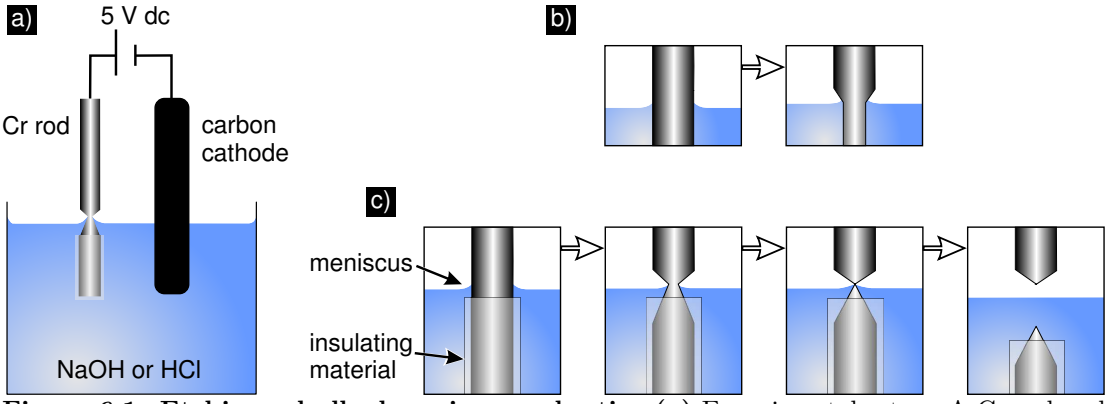

Figure 6.1: Etching a bulk chromium probe tip. **(a)** Experimental setup. A Cr rod and a carbon cathode are dipped into an etching solution and a dc voltage is applied. **(b)** First, the rod is etched for $10 - 20$ minutes to achieve a nearly circular cross section and to reduce the diameter. **(c)** Drop-off method: Being covered by insulating material, the rod in the solution is only etched at the meniscus. The lower part of the Cr rod which drops off is used as the probe tip.

voltage pulses are also applied for *in situ* preparation, resulting in changes in the morphology, the electronic properties, or magnetic orientation of the tip.

6.2 Magnetic imaging with bulk Cr tips

As shown in Chap. 5, the well-known system of the combined Fe mono- and double-layer on W(110) provides a variety of magnetization directions: Whereas the monolayer (ML) has a ferromagnetic order with the easy axis pointing along the $[1\bar{1}0]$-direction [189], the double layer (DL) exhibits an easy axis along the [110]-direction, with Néel-type domain walls rotating through the [001]-direction [165, 182]. Hence, this system is ideal for the magnetic characterization of bulk Cr tips.

A large-scale topography image obtained with a bulk Cr tip is shown in Fig. 6.2(a). Approximately 1.5 atomic layers of iron were deposited on a clean W(110) substrate by molecular beam epitaxy, with subsequent annealing at 550 K for four minutes, resulting in a step-flow growth of the Fe double layer on the wetting monolayer. Regions of pseudomorphic ML and DL coverages coexist, and dislocation lines run along the [001]-direction (cf. Chap. 5).

Simultaneously to the constant-current topography image, the spatially resolved differential conductance $\mathrm{d}I/\mathrm{d}U$ was recorded using the lock-in technique. This map is shown in Fig. 6.2(b). It reveals the magnetization of the sample, since $\mathrm{d}I/\mathrm{d}U$ scales with the cosine of the angle between the magnetization of the tip and the sample (see Sec. 2.3). Dark vertical lines on the DL appear in the magnetic $\mathrm{d}I/\mathrm{d}U$ map. These are dislocation lines that are formed to relieve the strain in the film (cf. Chap. 5). Two different types of domains appearing bright

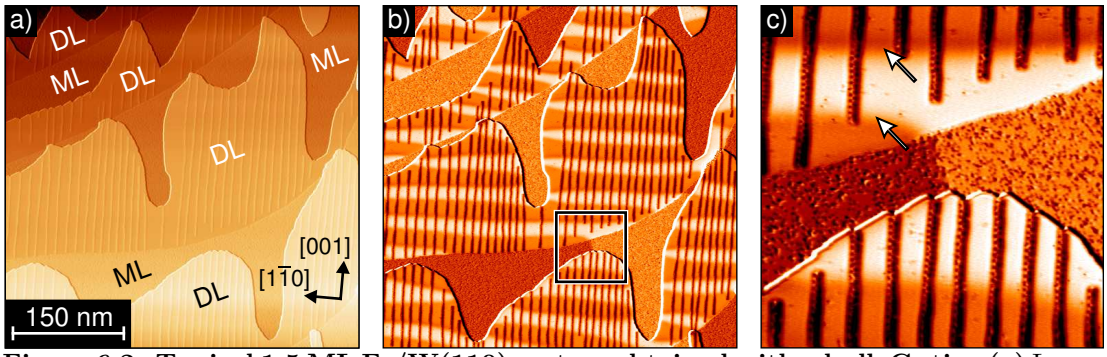

Figure 6.2: Typical 1.5 ML Fe/W(110) system obtained with a bulk Cr tip. (a) Large-scale topography image. Monolayer (ML) and double layer (DL) areas are visible. **(b)** Simultaneously recorded $\mathrm{d}I/\mathrm{d}U$ map, revealing magnetic contrast on the ML domains and the DL domains. **(c)** Zoom of (b) as indicated by the box. It reveals a magnetic contrast on the DL domain walls, appearing bright or dark, respectively (marked by arrows). $U = -200\,\mathrm{mV}$, $I = 2\,\mathrm{nA}$, $T = 41\,\mathrm{K}$.

and dark are observed on the ML as well as on the DL. A magnified region shown in Fig. 6.2(c) reveals that the DL domains are separated by alternating bright or dark domain walls.

Bright and dark domains on the ML have been observed in previous investigations with magnetic thin-film tips (e.g. Fe/W- and Cr/W-tips), which were sensitive to the in-plane component of surface magnetization [190, 191]. Hence, the domain pattern on the ML in Fig. 6.2(b) can be attributed to the magnetic structure of the ML which is known to have a uniaxial anisotropy lying in the surface plane (see Chap. 5). The domain pattern on the DL has been observed previously with magnetic thin-film tips (e.g. Gd/W-tips), that are sensitive to the magnetization pointing out of the surface plane [207]. Hence, the DL domains in Fig. 6.2(b) reveal regions of the DL where the surface magnetization is directed out of the surface. The interjacent DL domain walls appear bright and dark when imaged with an in-plane sensitive tip, as is also known from previous studies [207]. As discussed in Chap. 5, in these Néel-type domain walls the magnetization rotates around the $[1\bar{1}0]$-direction, locally pointing along the in-plane [001]-direction. The domain walls in Fig. 6.2(c) indicate regions of the DL where the magnetization lies in the surface plane.

Consequently, all magnetic features that are to be found on the ML and the DL areas are clearly visible when imaged with a bulk Cr tip. Hence, the bulk Cr tip is sensitive to the in-plane ML domains, the in-plane DL domain walls and the out-of-plane DL domains. This is significantly different from the magnetic sensitivity of magnetic thin-film tips, that are usually exclusively sensitive to the surface magnetization direction lying in the plane *or* pointing out of the surface plane [207]. Previously the magnetic features of the iron ML and DL were observed with different tips, whereas here all of the magnetic features are imaged simultaneously with one and the same tip.

Constant height spectroscopy

A topography image of the 1.5 ML Fe/W(110) system is shown in Fig. 6.3(a). Again, regions of pseudomorphic ML and DL coverages coexist, and dislocation lines running along the [001] direction are found. In the corresponding magnetic $\mathrm{d}I/\mathrm{d}U$ map shown in Fig. 6.3(b), again two different types of domains on the ML as well as on the DL are observed, the latter separated by alternating domain walls. The magnetization structure on the ML and the DL are indicated on the map and in the zoom inset of Fig. 6.3(b). All of the magnetic features that are found on the ML and the DL areas are clearly visible, indicating that the bulk Cr tip is sensitive to all of the in-plane as well as to the out-of-plane component of the sample magnetization.

Constant height spectroscopy has been performed to characterize the tip-sample tunnel junction. The tip has been stabilized above the surface at $I = 2\,\mathrm{nA}$

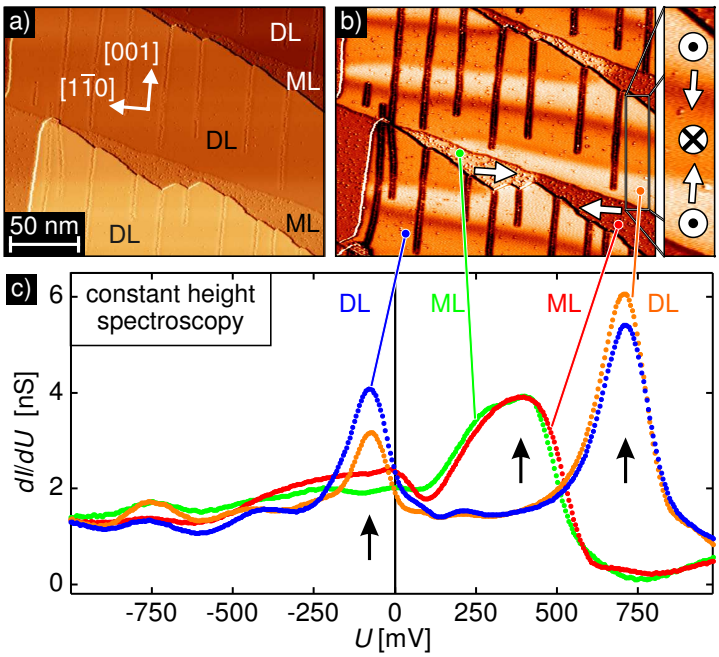

Figure 6.3: Characterization of a bulk Cr tip on the 1.5 ML Fe/W(110) system. **(a)** Topography image, taken at $U = +100\,\mathrm{mV}$. Monolayer (ML) and double layer (DL) areas are visible. **(b)** Simultaneously recorded $\mathrm{d}I/\mathrm{d}U$ map, revealing magnetic contrast on the ML domains, the DL domains, and the DL domain walls. The magnetization structure on the ML and the DL is marked on the map and the zoom inset. **(c)** Constant height spectroscopy above two different ML and two different DL domains (stabilization parameters: $I = 2\,\mathrm{nA}$, $U = -1000\,\mathrm{mV}$). A peak at $U \approx +400\,\mathrm{mV}$ is visible for the ML, and two peaks at $U \approx -80\,\mathrm{mV}$ and $U \approx +700\,\mathrm{mV}$ are resolved on the DL (positions marked by arrows). $T = 41\,\mathrm{K}$.

and $U = -1000\,\mathrm{mV}$. To fix the tip-sample distance, the feedback loop is then switched off. The tunnel current is measured while the sample bias is ramped from the initial voltage to the final voltage $U = +1000\,\mathrm{mV}$, and simultaneously the differential conductance $\mathrm{d}I/\mathrm{d}U(U)$ is determined by means of the lock-in technique. In this way the surface local density of states at an energy equal to eU and at a certain distance to the surface is revealed (cf. Sec. 2.2.2) [41–43].

Figure 6.3(c) shows the $\mathrm{d}I/\mathrm{d}U$ spectroscopy curves recorded at constant height above two different ML and DL domains. A typical empty-state peak at $U \approx +400\,\mathrm{mV}$ is observed for the ML, which is in agreement with previous investigations using different tip materials [184]. On the DL two peaks at $U \approx -80\,\mathrm{mV}$ and $U \approx +700\,\mathrm{mV}$ are resolved, which is also consistent with previous studies using different tip materials [184, 188]. Comparison with theory has revealed that these peaks are caused by two d_{z^2}-like states [188].

Despite these sample-related peaks the spectroscopy curves reveal no dominant features. This indicates that the local density of states of the tip is very

homogeneous. Over a wide bias voltage range, there are no prominent tip-related electronic features which could obscure the sample-related electronic structure of interest (cf. Sec. 2.2.2). Hence, bulk Cr tips are suitable for spectroscopic investigations on unknown sample systems.

6.3 Characterization on the iron monolayer

The magnetic map in Fig. 6.3 has been obtained at a sample bias voltage $U = +100\,\mathrm{mV}$. The question arises how the magnetic contrast depends on the applied sample bias. A magnified region of the magnetic map of Fig. 6.3(b) is shown in Fig. 6.4(a), focusing on the Fe ML regime at a W step edge.sing on the Fe ML regime at a W step edge. When the Fe coverage exceeds a single atomic layer, the impurities in the Fe accumulate on the wetting monolayer, as is known from previous studies [191]. The differential conductance on such an impurity differs from that on the Fe because of their different electronic nature. In Fig. 6.4(a) the impurities appear as dark spots on the ML. Two oppositely magnetized domains on the ML are visible. A line section taken across these two respective bright and dark domains is shown in Fig. 6.4(b). To quantify the magnetic contrast, a mean $\mathrm{d}I/\mathrm{d}U$ signal ('$\mathrm{d}I/\mathrm{d}U_{\mathrm{bright}}$' and '$\mathrm{d}I/\mathrm{d}U_{\mathrm{dark}}$') is determined by averaging over the data points of the respective domain in Fig. 6.4(b). This allows the determination of the normalized magnetic asymmetry $A_{\mathrm{d}I/\mathrm{d}U}$ which is defined as

$$A_{\mathrm{d}I/\mathrm{d}U} = \frac{\mathrm{d}I/\mathrm{d}U_{\mathrm{bright}} - \mathrm{d}I/\mathrm{d}U_{\mathrm{dark}}}{\mathrm{d}I/\mathrm{d}U_{\mathrm{bright}} + \mathrm{d}I/\mathrm{d}U_{\mathrm{dark}}}, \tag{6.1}$$

where $\mathrm{d}I/\mathrm{d}U_{\mathrm{bright}}$ ($\mathrm{d}I/\mathrm{d}U_{\mathrm{dark}}$) is the magnetic $\mathrm{d}I/\mathrm{d}U$ signal on a magnetic feature appearing 'bright' ('dark') at $U = +100\,\mathrm{mV}$, respectively. $A_{\mathrm{d}I/\mathrm{d}U}$ is a quantitative measure of the magnetic contrast. Here, $A_{\mathrm{d}I/\mathrm{d}U}$ of the ML domains at $U =$

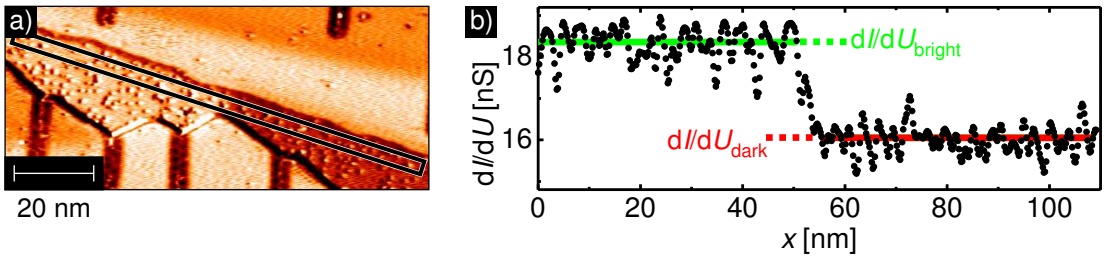

Figure 6.4: Magnetic contrast on the iron monolayer. (a) Magnetic $\mathrm{d}I/\mathrm{d}U$ map obtained at $U = +100\,\mathrm{mV}$ showing two oppositely magnetized ML domains. **(b)** Line section (black data points) across the two domains, averaged over the area marked in (a). The mean $\mathrm{d}I/\mathrm{d}U$ signal averaged over the data points of the respective domain is indicated by the green and red lines. $I = 2\,\mathrm{nA}$, $T = 41\,\mathrm{K}$.

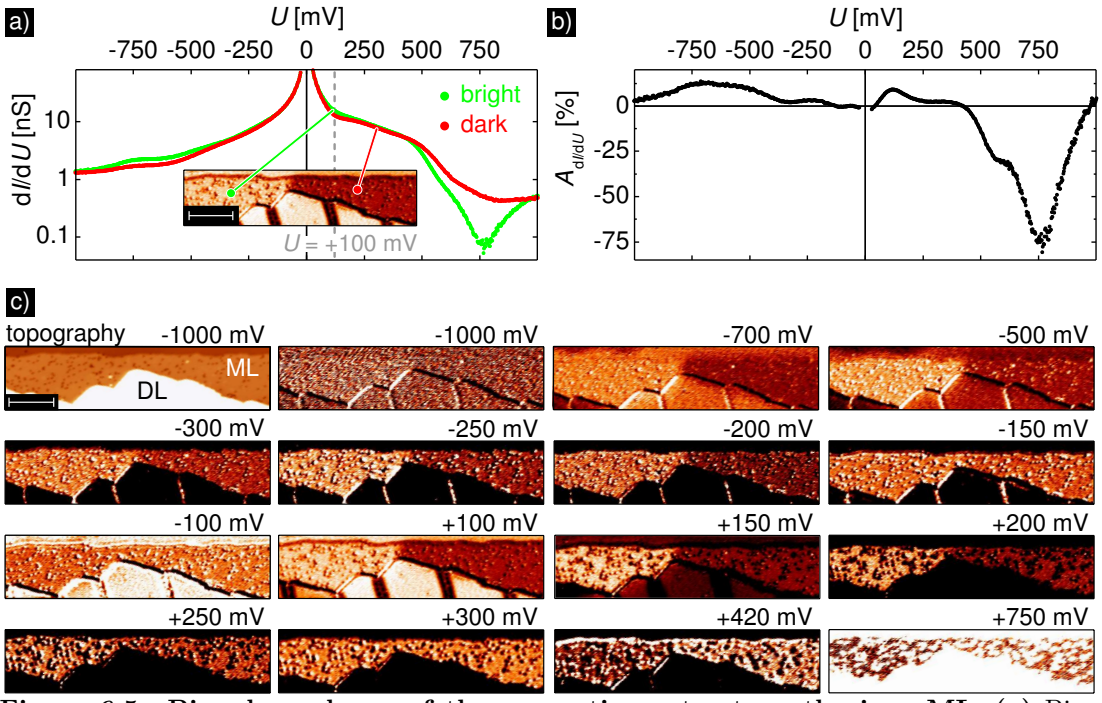

Figure 6.5: Bias dependence of the magnetic contrast on the iron ML. (a) Bias-dependent magnetic $\mathrm{d}I/\mathrm{d}U$ signal taken on two different ML domains. Inset: a typical magnetic map. **(b)** Corresponding magnetic asymmetry $A_{\mathrm{d}I/\mathrm{d}U}$. **(c)** Bias-dependent series of magnetic $\mathrm{d}I/\mathrm{d}U$ maps. The contrast has been adjusted to the ML magnetic features. The image in the upper left shows the topography. Length of the scale bar: 20 nm. $I = 2\,\mathrm{nA}$, $T = 41\,\mathrm{K}$.

+100 mV is 7 %, which is comparable to values I also observed with Cr-coated W-tips.

At different bias voltages, different electronic states (*s*-, *p*-, and *d*-like states) with a different degree of spin polarization contribute to the spin-polarized tunnel current [208]. Hence, the spin-polarization of the tunnel current is expected to depend on the bias voltage [166] and accordingly the magnitude of the magnetic contrast. To study the bias dependence of the magnetic contrast on the ML systematically, the magnetic $\mathrm{d}I/\mathrm{d}U$ signal has been recorded as a function of sample bias U at constant current (closed feedback loop) above the two different ML domains. In Fig. 6.5(a) and (b) the bias-dependent magnetic $\mathrm{d}I/\mathrm{d}U(U)$ signal and the normalized magnetic asymmetry $A_{\mathrm{d}I/\mathrm{d}U}(U)$ are shown. Magnetic $\mathrm{d}I/\mathrm{d}U$ maps for different bias voltages are shown in Fig. 6.5(c).

As indicated by the variation of $A_{\mathrm{d}I/\mathrm{d}U}$ with bias voltage, the magnitude of the magnetic contrast in the corresponding $\mathrm{d}I/\mathrm{d}U$ maps varies. It is remarkable, that $A_{\mathrm{d}I/\mathrm{d}U}$ is quite large over a wide bias range between $U \approx -750\,\mathrm{mV}$ and $+250\,\mathrm{mV}$ and only vanishes for $-100\,\mathrm{mV} < U < 0$ and $U \approx +300\,\mathrm{mV}$. At higher positive bias values, $A_{\mathrm{d}I/\mathrm{d}U}$ becomes negative, indicating an inversion of the magnetic contrast,

that can be observed when changing U to +750 mV in Fig. 6.5(c). However, the strong asymmetry of $\approx 75\%$ at $U = +750$ mV determined from spectroscopy cannot be confirmed by the magnetic contrast of the $\mathrm{d}I/\mathrm{d}U$ map and is presumably attributed to the strong influence of the impurities at this particular sample bias.

In conclusion, analyzing the bias-dependent magnetic asymmetry from constant-current spectroscopy as well as from the corresponding constant-current $\mathrm{d}I/\mathrm{d}U$ maps reveals that the bulk Cr tip is sensitive to the $[1\bar{1}0]$ in-plane magnetization direction on the ML over a wide bias range.

6.4 Characterization on the iron double layer

As discussed for the ML, owing to different contributing electronic states at different bias voltages, the spin-polarization of the tunnel current is expected to depend on the bias voltage [166] and the magnitude of the magnetic contrast will also change. The magnetic contrast on the Fe DL has been analyzed quantitatively as a function of the bias voltage as on the Fe ML. A systematic constant-current spectroscopy study has been performed for the DL regime: The magnetic $\mathrm{d}I/\mathrm{d}U$ signal has been recorded as a function of the sample bias U at constant current (closed feedback loop) above two domains and two different domain walls, respectively. These constant-current spectroscopy curves are shown in Fig. 6.6(a). For a quantitative measure of the magnetic contrast, the respective normalized magnetic asymmetries $A_{\mathrm{d}I/\mathrm{d}U}$ have been determined according to Eq. 6.1. They are shown in Fig. 6.6(b).

$A_{\mathrm{d}I/\mathrm{d}U}$ on the DL domains reveals a broad maximum located around $U \approx -700$ mV and becomes negative at $U = -100$ mV, indicating a magnetic contrast reversal. The magnetic maps in Fig. 6.6(b) reveal that the magnetic contrast on the DL domains flips when changing the sample bias from $U = -700$ mV to $U = -100$ mV. In general, $A_{\mathrm{d}I/\mathrm{d}U}$ on the DL domain walls looks similar to $A_{\mathrm{d}I/\mathrm{d}U}$ on the DL domains and is slightly decreased for negative bias. For both, DL domain walls as well as DL domains, $A_{\mathrm{d}I/\mathrm{d}U} \neq 0$ over a wide bias voltage range. Consequently, the bulk Cr tip is sensitive to both the [110] out-of-plane magnetization direction of the DL domains as well as the [001] in-plane magnetization direction of the DL domain walls over a wide bias range. This is confirmed by magnetic $\mathrm{d}I/\mathrm{d}U$ maps for different bias voltages, that are shown in Fig. 6.6(c). Bright and dark magnetic domains and domain walls are clearly visible in the magnetic $\mathrm{d}I/\mathrm{d}U$ maps at various bias voltages.

Interestingly, the magnetic domains and in particular the domain walls look different at different bias voltages. For example, going from the bottom to the top of the magnetic map at $U = -200$ mV in Fig. 6.6(c) a bright domain, a bright domain wall, a dark domain, a dark domain wall, and a bright domain are visible. (The walls are marked by arrows.) This magnetic contrast is consistent with

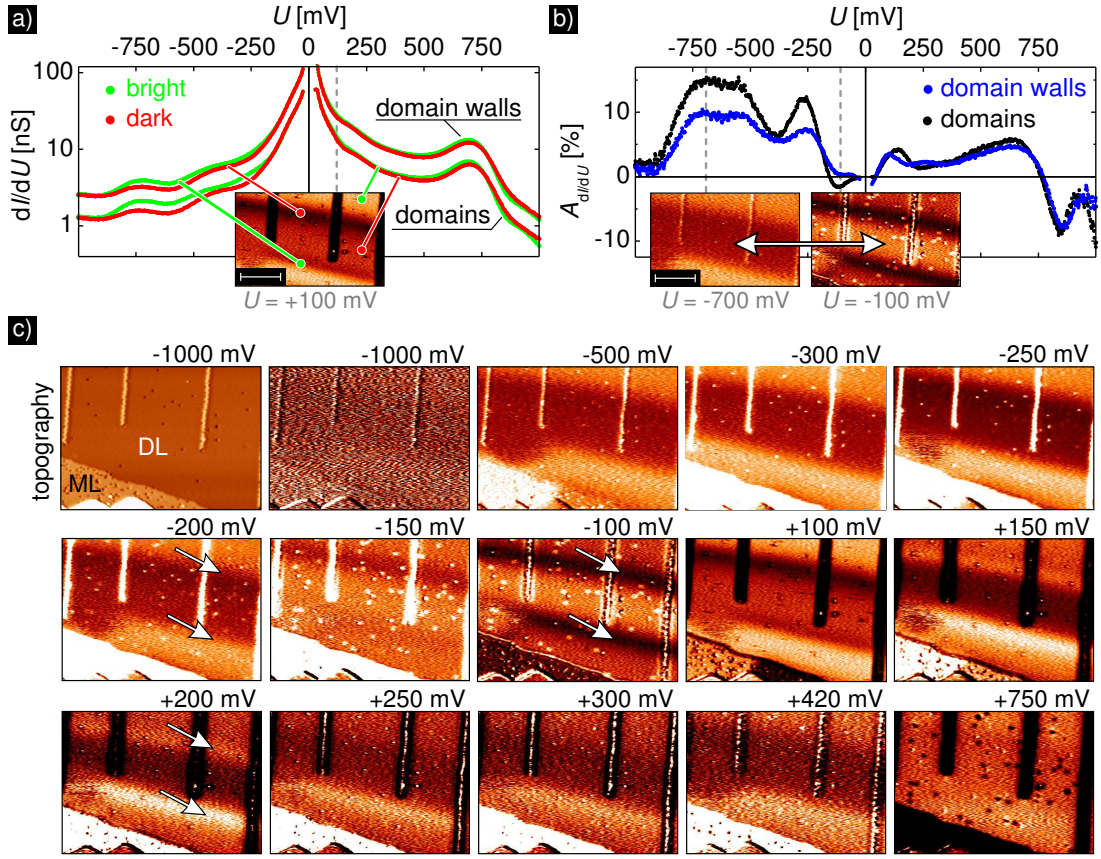

Figure 6.6: Bias dependence of the magnetic contrast on the iron DL. (a) Bias-dependent magnetic $\mathrm{d}I/\mathrm{d}U$ signal taken on two different DL domains and two different domain walls, as indicated in the inset magnetic map. The data points on the DL domain walls are multiplied by a factor of 2 for clear assignment. **(b)** Magnetic asymmetry $A_{\mathrm{d}I/\mathrm{d}U}$ on the DL domains and domain walls respectively. Insets: Two exemplary magnetic maps, revealing a contrast inversion on the DL domains. **(c)** Bias-dependent series of magnetic $\mathrm{d}I/\mathrm{d}U$ maps. The contrast has been adjusted to the DL magnetic features. The image in the upper left shows the respective topography. Length of the scale bar: 20 nm. $I = 2\,\mathrm{nA}$, $T = 41\,\mathrm{K}$.

the known underlying magnetic structure which is a spin spiral which rotates through all directions in the $(1\bar{1}0)$ plane (c.f. Chap. 5). However, there are some bias voltages, where *both* walls appear bright. For example, in contrast to $U = -200\,\mathrm{mV}$, at $U = +200\,\mathrm{mV}$ the upper domain wall appear brighter than the bright domain. Hence, the differential conductance on *both* domain walls is higher than on the bright domain. In the magnetic map at $U = -100\,\mathrm{mV}$ *both* domain walls appear strikingly dark, indicating a conductance that is lower on *both* domain walls than on the darker domains. These observations cannot be explained by a pure magnetic contrast arising from the tunneling magnetoresistance (TMR) effect.

It has already been observed, that – when imaged with a nonmagnetic tip – at certain bias voltages adjacent domain walls on the Fe DL appear *both* bright [181, 209] or dark [181, 187, 188] in a dI/dU map. Hence, adjacent domain walls exhibit a conductance significantly higher or lower than on the domains. This is attributed to the local electronic structure of the Fe DL that depends on the local orientation of the magnetization. Owing to spin-orbit coupling (SOC) the electronic states contributing to the tunnel current depend on the magnetization direction [187, 188]. It has been shown by theory that SOC leads to a magnetization direction dependent hybridization of the minority bands with different orbital character (d_{xy+xz} and d_{z^2}-like states), thereby changing the local density of states in the vacuum [187, 188]. Consequently, at a given sample bias voltage, on the domains and the domain walls different electronic states with different vacuum decay lengths may contribute to the tunnel current, resulting in different conductivities (cf. Sec. 2.2.2). This tunneling anisotropic magnetoresistance (TAMR) can be used for magnetic imaging with a non-magnetic tip, as has been demonstrated by experiments [187, 188, 210].

A schematic drawing of possible conductance levels on the DL domains and domain walls due to the SOC induced TAMR effect is shown in Fig. 6.7(a). Here, the conductance on adjacent domain walls is significantly higher than that on the domains allowing for domain wall imaging. However, as all domain walls exhibit the *same* conductance level, domain walls of opposite magnetization direction cannot be distinguished. In contrast, the distinctive feature of an in-plane magnetic contrast due to the TMR effect is the fact that domain walls of opposite magnetization direction exhibit *different* conductance levels. This is illustrated in Fig. 6.7(b), where adjacent domain walls exhibit different conductance levels and also differ from the conductance level on the domains.

Probing with a magnetic tip both the TMR and the TAMR effect may contribute to the tunnel current [210]. Consequently, the contrast in the dI/dU map at a certain sample bias is a convolution of the magnetic and SOC-induced con-

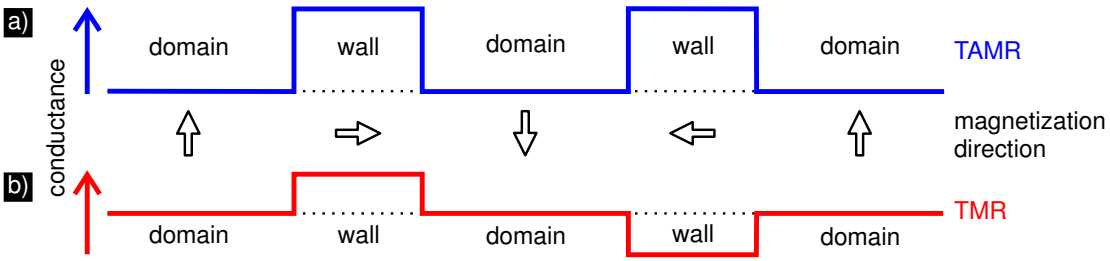

Figure 6.7: Schematic sketch of the TAMR and TMR effect. Conductance of domains and domain walls owing to **(a)** tunneling anisotropic magnetoresistance (TAMR) and **(b)** tunneling magnetoresistance (TMR). The surface magnetization direction is indicated by the arrows.

trast contributions. To separate the SOC-induced from the magnetic contribution to a first approximation, a line section across two DL domain walls is described by a profile of the form:

$$\begin{aligned} y(x) &= y_0 + y_{\mathrm{soc}} + y_{\mathrm{sp}} \\ &= y_0 + y_{\mathrm{soc},0} \cdot \left| \sin\left(\pi/2 + \sum_{i=1}^{2} \arcsin\left[\tanh \frac{x - x_i}{w/2} \right] \right) \right|^2 \\ &\quad + y_{\mathrm{sp},0} \cdot \cos\left(\theta_{\mathrm{tip}} + \underbrace{\sum_{i=1}^{2} \arccos\left[\tanh \frac{x - x_i}{w/2} \right]}_{\theta_{\mathrm{DL}}} \right), \end{aligned} \tag{6.2}$$

where $y(x)$ is the $\mathrm{d}I/\mathrm{d}U$ signal measured at a lateral tip position x, y_0 is the spin-averaged, y_{soc} is the SOC-induced [188] and y_{sp} is the spin-polarized contribution [193] to the $\mathrm{d}I/\mathrm{d}U$ signal, $y_{\mathrm{soc},0}$ and $y_{\mathrm{sp},0}$ are the respective amplitudes, x_i is the center position of the domain wall i ($i = 1; 2$), w is the domain wall width and θ_{tip} is the angle between the tip magnetization direction and the surface normal. The last term y_{sp} is the profile of two 180° domain walls. It strongly depends on the tip magnetization direction, as illustrated in Fig. 6.8. The underlying spatial evolution of the DL magnetization angle θ_{DL} is shown in Fig. 6.8(b). For $\theta_{\mathrm{tip}} = 0°$ the magnetic probe tip is only sensitive to magnetization directions pointing out of the surface plane, resulting in a pure domain contrast with alternating bright and dark domains, as observed for example with Gd-coated W-tips [207]. When

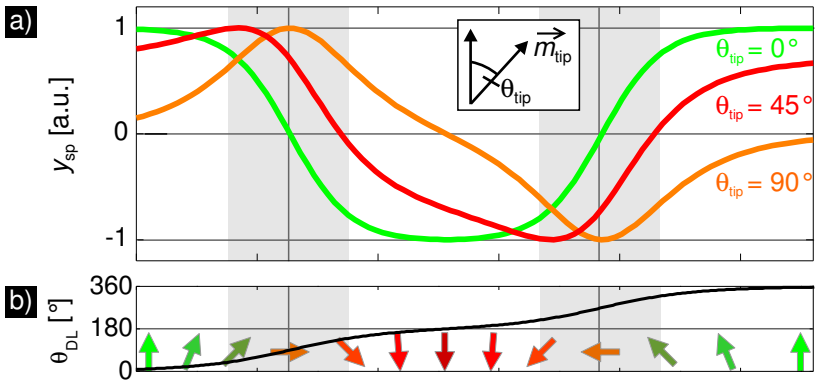

Figure 6.8: Dependence of the domain wall profile on the tip magnetization direction. **(a)** Profile of two 180° domain walls for angles $\theta_{\mathrm{tip}} = 0°, 45°, 90°$ with θ_{tip} being the angle between the surface normal and the tip magnetization direction, as depicted in the inset. Domain walls are indicated by shaded areas. **(b)** Corresponding spatial evolution of θ_{DL} of the DL magnetization. The inset indicates the evolution of the magnetic moments.

$\theta_{\mathrm{tip}} = 90°$, only magnetization directions lying in the surface plane can be sensed, resulting in a pure domain wall contrast with alternating bright and dark domain walls, as observed for example with Fe-coated W-tips [207]. Interestingly, with a tip magnetization canting angle $\theta_{\mathrm{tip}} = 45°$, magnetization directions both lying in and pointing out of the surface plane can be sensed, resulting in a magnetic contrast on both the domain walls and the domains, as depicted in Fig. 6.8(a).

Figure 6.9(a) shows a magnetic $\mathrm{d}I/\mathrm{d}U$ map recorded at $U = +200\,\mathrm{mV}$. A line section across two adjacent DL domain walls is shown in the top panel of Fig. 6.9(b). The tunneling conductance $\mathrm{d}I/\mathrm{d}U$ on the two outer domains is higher than on the inner domain, revealing the magnetic contrast of the domains. In addition, the conductance on the first domain wall is higher than on the second, indicating a magnetic contrast on the domain walls. However, the conductance on *both* domain walls is higher than on the bright domains, hence *both* appear bright in the $\mathrm{d}I/\mathrm{d}U$ map. This can only be explained by the SOC-induced TAMR effect. To separate the SOC-induced from the magnetic contribution, the data has been fitted using Eq. 6.2. Fitting yields a spin-averaged $\mathrm{d}I/\mathrm{d}U$ signal of $y_0 = (9.314 \pm 0.005)\,\mathrm{nS}$ in accordance with the constant-current spectroscopy at the applied bias voltage $U = +200\,\mathrm{mV}$ (cf. Fig. 6.6(a)). The SOC part of the fit (y_{soc}) is shown in the middle panel of Fig. 6.9(b). It reveals two peaks centered on the domain wall positions, indicating that at $U = +200\,\mathrm{mV}$ SOC induces a higher conductance on the DL domain walls than on the DL domains. From the fit, the SOC-induced contribution can be estimated to be about 5% of the total (spin-averaged) $\mathrm{d}I/\mathrm{d}U$ signal. The magnetic part of the fit (y_{sp}) is shown in the

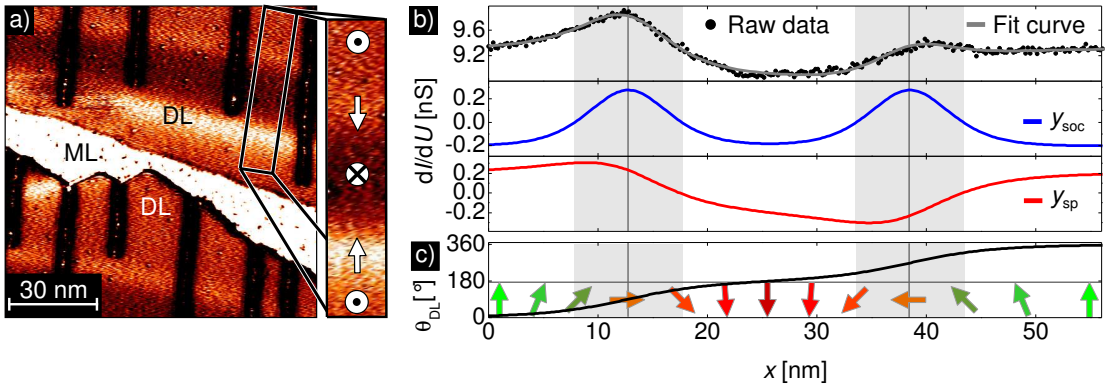

Figure 6.9: Domain wall profile on the iron DL. (a) Magnetic $\mathrm{d}I/\mathrm{d}U$-map taken at $U = +200\,\mathrm{mV}$. The magnetization structure on the DL is marked in the zoom inset. **(b)** (Top:) Line section across two DL domain walls, averaged over the area marked in (a). Data were fitted using Eq. 6.2. (Middle:) SOC induced part of the fit (y_{soc}). (Bottom:) Magnetic part of the fit (y_{sp}). **(c)** Spatial evolution of θ_{DL} of the DL magnetization, as determined from the fit. The inset indicates the evolution of the magnetic moments. Domain walls are indicated by shaded areas. $I = 2\,\mathrm{nA}$, $T = 41\,\mathrm{K}$.

bottom panel of Fig. 6.9(b). It shows a magnetic contrast on both the DL domains as well as on the DL domain walls, in accordance with the line profile of the raw data. From the fit, the angle θ_{tip} is found to be $(49.00 \pm 0.09)^\circ$ which is close to the equal weighting of in-plane and out-of-plane sensitivity at $\theta_{\mathrm{tip}} = 45^\circ$ (cf. Fig. 6.8). The magnetic asymmetry $A_{\mathrm{sp}} = y_{\mathrm{sp},0}/y_0$ [193] is calculated from the fit parameter $y_{\mathrm{sp},0} = (0.309 \pm 0.004)\,\mathrm{nS}$, resulting in about 3%. Consequently, at $U = +200\,\mathrm{mV}$ the SOC-induced contribution dominates over the magnetic one.

The whole set of $\mathrm{d}I/\mathrm{d}U$ maps shown in Fig. 6.6(c) has been fitted in this way using Eq. 6.2 and all of the parameters $[y_0; y_{\mathrm{soc},0}; y_{\mathrm{sp},0}; x_1; x_2; w; \theta_{\mathrm{tip}}]$ have been determined as a function of the sample bias U. The bias-dependent magnetic asymmetry A_{sp} is shown in Fig. 6.10(a) and varies from a minimum absolute value of 2% to a maximum value of 17%. The SOC-induced contribution $y_{\mathrm{soc},0}$ normalized to the spin-averaged $\mathrm{d}I/\mathrm{d}U$ signal y_0 as a function of the bias voltage is shown in Fig. 6.10(b). $A_{\mathrm{soc}} = y_{\mathrm{soc},0}/y_0$ is generally a few percent. In addition, A_{soc} exhibits oscillations around zero as a function of the sample bias. This bias-dependent behavior is in accordance with theoretical studies predicting rapid oscillations of the TAMR with bias voltage [211] and experiments revealing such oscillations in a bias voltage range of 100 mV [212]. According to these bias-dependent changes in sign, the domain walls in the corresponding $\mathrm{d}I/\mathrm{d}U$ maps in Fig. 6.6(c) appear dark for $-200\,\mathrm{mV} < U < +150\,\mathrm{mV}$, and bright otherwise.

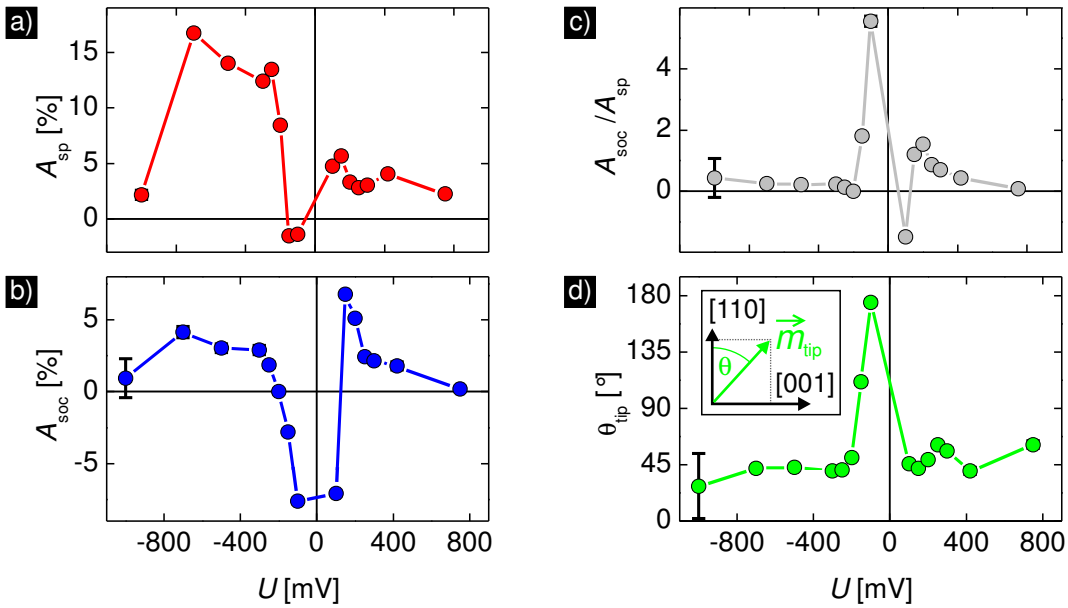

Figure 6.10: Bias-dependence of the DL domain wall profile fit results. **(a)** Magnetic asymmetry $A_{\mathrm{sp}} = y_{\mathrm{sp},0}/y_0$. **(b)** Normalized SOC induced contribution $A_{\mathrm{soc}} = y_{\mathrm{soc},0}/y_0$. **(c)** Ratio $A_{\mathrm{soc}}/A_{\mathrm{sp}}$. **(d)** Angle θ_{tip} between the tip magnetization direction and the surface normal, as indicated in the inset. $I = 2\,\mathrm{nA}$, $T = 41\,\mathrm{K}$.

Figure 6.10(c) shows the ratio of the normalized SOC induced contribution to the magnetic asymmetry, $A_{\mathrm{soc}}/A_{\mathrm{sp}}$. It is a measure of the influence of the SOC induced contribution to the domain wall profile with sample bias. Figure 6.10(c) shows that $A_{\mathrm{soc}}/A_{\mathrm{sp}}$ is largest around zero bias voltage, being approximately unity for positive sample bias voltages, but almost zero at higher negative sample bias. For large $A_{\mathrm{soc}}/A_{\mathrm{sp}}$, strong TAMR effects are expected. In contrast, with $A_{\mathrm{soc}}/A_{\mathrm{sp}} \approx 0$ pure magnetic maps due to TMR are expected.

The angle θ_{tip} determined from the fits of the domain wall profiles at different sample bias voltages is shown in Fig. 6.10(d). Besides the values at $U = -150\,\mathrm{mV}$ and $U = -100\,\mathrm{mV}$ where the TAMR effect dominates (cf. Fig. 6.10(c)), θ_{tip} varies only slightly with sample bias around a mean of $(46 \pm 9)°$. Here, θ_{tip} is extracted from fits which include the SOC-induced contribution as an additive correction (cf. Eq. 6.2). θ_{tip} can be determined most reliably at a sample bias voltage, where the TAMR effect is negligible. As can be seen from Fig. 6.10(b) and (c), at $U = -200\,\mathrm{mV}$ there is no SOC-induced contribution to the $\mathrm{d}I/\mathrm{d}U$ signal. Consequently, this sample bias voltage can be used to extract the tip magnetization angle θ_{tip} reliably. At this voltage the lateral variation of the $\mathrm{d}I/\mathrm{d}U$ signal is *only* determined by the TMR effect depending on the relative orientation between the tip and the sample magnetization. In Fig. 6.11(a) a magnetic $\mathrm{d}I/\mathrm{d}U$ map taken at $U = -200\,\mathrm{mV}$ is shown. A line section across two adjacent DL domain walls is shown in Fig. 6.11(b). The data has been fitted with a profile of two 180° domain walls (given by Eq. 6.2 omitting y_{soc}). The fit yields a domain wall width $w = (7.2 \pm 0.1)\,\mathrm{nm}$, which is consistent with previous investigations [193].

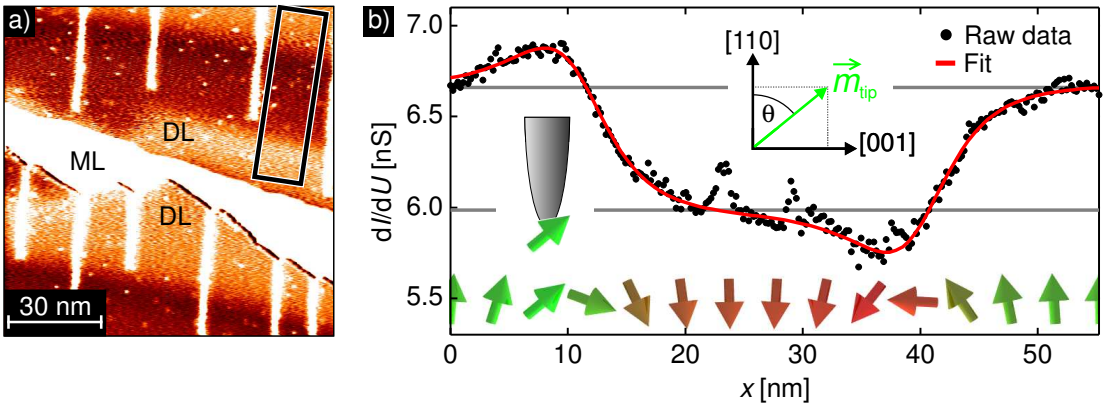

Figure 6.11: Determination of the tip magnetization canting angle. (a) Magnetic map taken at $U = -200\,\mathrm{mV}$. **(b)** Line section across two DL domain walls, averaged over the area marked in (a). Fitting a profile for two 180° domain walls yields the domain wall width w and the angle θ between the tip magnetization direction and the surface normal. The inset indicates the magnetization direction of the tip and the spatial evolution of the magnetic moments along the line section. $I = 2\,\mathrm{nA}$, $T = 41\,\mathrm{K}$.

The angle is found to be $\theta_{\mathrm{tip}} = (50.8 \pm 0.9)^\circ$. The relative orientation of the tip and sample magnetization along the line profile is depicted in Fig. 6.11(b). The bulk Cr tip exhibits a canted tip magnetization which is sensitive to surface magnetization directions pointing out of the plane as well as lying in the surface plane.

6.5 Tuning the magnetic sensitivity via the sample bias voltage

The bias-dependent contrast on the domain and domain walls indicates that the magnetic sensitivity of the bulk Cr tip can be tuned using the sample bias voltage. At $U = -150\,\mathrm{mV}$ $A_{\mathrm{d}I/\mathrm{d}U}$ vanishes on the DL domains, whereas $A_{\mathrm{d}I/\mathrm{d}U} > 0$ on the DL domain walls, as shown in Fig. 6.12(a). This leads to a vanishing magnetic contrast on the DL domains, but a striking magnetic contrast on the DL domain walls, as shown in Fig. 6.12(b). Since the $\mathrm{d}I/\mathrm{d}U$ signal level of the lower DL domain wall coincides with that of the DL domains (due to the SOC induced contrast), only the upper domain wall is visible. At $U = -100\,\mathrm{mV}$ the magnetic sensitivity is the opposite way round: $A_{\mathrm{d}I/\mathrm{d}U}$ vanishes on the DL domain walls, and is inverted on the DL domains, as shown in Fig. 6.12(a). This results in no magnetic contrast on the DL domains walls, but a striking magnetic contrast on the DL domains, as can be seen in Fig. 6.12(c).

For both voltages, line sections across two adjacent DL domain walls on the DL area have been taken, as shown in Fig. 6.12(b) and (c). The line profiles from the $\mathrm{d}I/\mathrm{d}U$ maps have been fitted using Eq. 6.2. The magnetic contributions from the fit (y_{sp}) are shown in the middle panel of Fig. 6.12(b) and (c). At $U = -150\,\mathrm{mV}$ the fit yields a tip magnetization angle $\theta_{\mathrm{tip}} = (111 \pm 2)^\circ$. Hence, at this particular bias voltage a dominant in-plane sensitivity of the bulk Cr tip is observed. At $U = -100\,\mathrm{mV}$ the fit yields a tip magnetization angle $\theta_{\mathrm{tip}} = (175 \pm 2)^\circ$, that is close to the alignment along the surface normal at $\theta = 180^\circ$. Interestingly, also the in-plane contrast on the monolayer domains vanishes at $U = -100\,\mathrm{mV}$, as can be seen in $A_{\mathrm{d}I/\mathrm{d}U}$ and the magnetic map in Fig. 6.5. The bulk Cr tip exhibits an almost exclusive out-of-plane sensitivity at a sample bias $U = -100\,\mathrm{mV}$.

These findings are explained within the concept of intra-atomic noncollinear magnetism [213, 214]. The spin density is treated as a vector field which, if integrated over the whole magnetic volume, gives the global magnetization, but may vary within the magnetic volume. For example different orbitals of the same atom can exhibit different spin quantization axes [215]. The experimental observations can be interpreted in terms of tunneling from different orbitals of the probing atom at the apex of the tip which, as a result of intra-atomic noncollinear magnetism, exhibit different spin density orientations.
At $U = -150\,\mathrm{mV}$ an unoccupied orbital of the tip with a spin density orientation

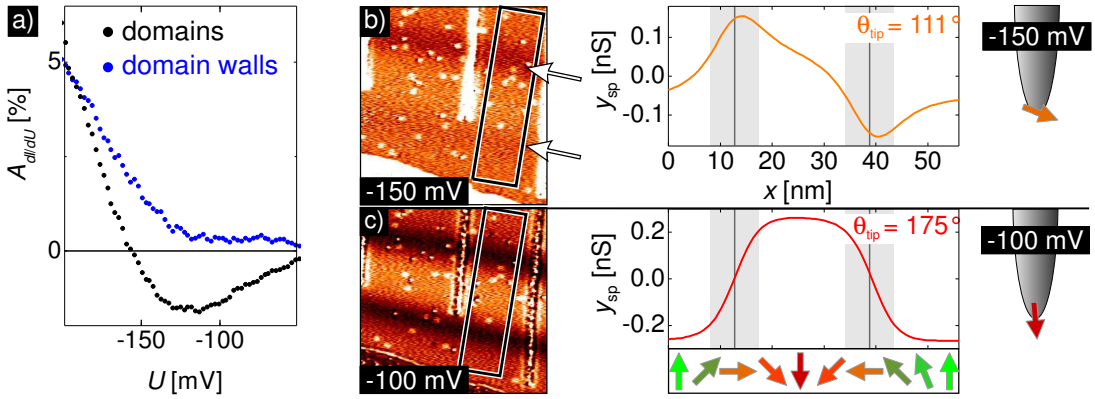

Figure 6.12: Tuning the magnetic sensitivity via the sample bias voltage. (a) Magnetic asymmetry $A_{\mathrm{d}I/\mathrm{d}U}$ on the DL domains (black) and domain walls (blue) as a function of the sample bias. Magnetic $\mathrm{d}I/\mathrm{d}U$-maps taken at **(b)** $U = -150\,\mathrm{mV}$ and **(c)** $U = -100\,\mathrm{mV}$. Line sections across two DL domain walls, averaged over the marked areas, have been fitted using Eq. 6.2. (Middle panel:) Magnetic part (y_{sp}) of the fit. Shaded areas indicate domain walls. The spatial evolution of the magnetic moments along the line section is indicated. (Right panel:) Schematic sketch of the magnetic sensitivity in dependence of applied sample bias voltage. $I = 2\,\mathrm{nA}$, $T = 41\,\mathrm{K}$.

(SDO) pointing almost parallel to the surface probes the density of states of the sample leading to in-plane sensitivity. At $U = -100\,\mathrm{mV}$, another unoccupied tip orbital with a SDO aligned with the surface normal yields out-of-plane sensitivity. This explains also the lack of in-plane contrast on the Fe monolayer domains at $U = -100\,\mathrm{mV}$ (cf. Fig. 6.5(c)). For other sample bias voltages an almost equally weighted in-plane and out-of-plane sensitivity with a mean $\theta_{\mathrm{tip}} = (46 \pm 9)^\circ$ is observed (cf. Fig. 6.10(d)). This indicates that the tunnel current flows through orbitals with a SDO collinear with the global bulk Cr tip magnetization that is canted by an angle θ to the surface normal, resulting in the observed combined in-plane and out-of-plane sensitivity. Here, even the slight variation of the angle with sample bias can be explained by slightly different weightings of the orbitals contributing to the tunnel current.

A bias-dependent magnetic sensitivity has been observed with other probe tips on the Fe DL on W(110). In Ref. [213, 214], a striking out-of-plane domain contrast at low bias voltages was found with an otherwise in-plane sensitive Fe/W-tip. With Gd/W-tips, which are normally out-of-plane sensitive, some bias voltages with a dominant in-plane contrast were found and explained within the concept of intra-atomic noncollinear magnetism [213, 214].

In conclusion, my experiments demonstrate that bulk Cr tips can be sensitive to all spatial magnetization directions, with tunable sensitivities to certain magnetization directions at chosen sample bias voltages.

6.6 Magnetic imaging at elevated temperatures

As demonstrated in the previous sections, both in-plane and out-of-plane surface magnetism can be imaged using bulk Cr tips at low temperatures around 40 K. As the Néel temperature of bulk chromium is $T_N = 311$ K [31], the question arises whether bulk Cr tips can be used for magnetic imaging at higher temperatures. On the Cr(001) surface the in-plane magnetic sensitivity of bulk Cr tips has already been demonstrated at room temperature [30]. In order to test the spatial magnetic sensitivity of bulk Cr tips on the system of the combined Fe ML and DL on W(110) at elevated temperatures, a temperature has to be chosen that is below the Curie temperatures of both the Fe ML and the Fe DL. Whereas the DL is still magnetically ordered at room temperature, T_c of the monolayer is ≈ 225 K [171, 174].

Figure 6.13(a) shows a topography image of the 1.5 ML Fe/W(110) system probed with a bulk Cr tip at $T = 184$ K. ML and DL areas are visible. The simultaneously recorded dI/dU map is shown in Fig. 6.13(b). Dark and bright domains on the DL are visible, indicating an out-of-plane magnetic contrast. The magnetization directions are indicated. Dark and bright domains are also visible on the ML. The contrast in the dI/dU map is weak, so the line sections across the two ML domains shown in Fig. 6.13(c) were averaged over the area marked in (b). The mean dI/dU signals, indicated by the red and the green line, clearly reveal a magnetic contrast on the ML domains. Both the in-plane and the out-of-plane magnetic sensitivity of bulk Cr tips at $T \approx 200$ K have been demonstrated. Consequently, at $T \approx 200$ K both the in-plane as well as the out-of-plane magnetic

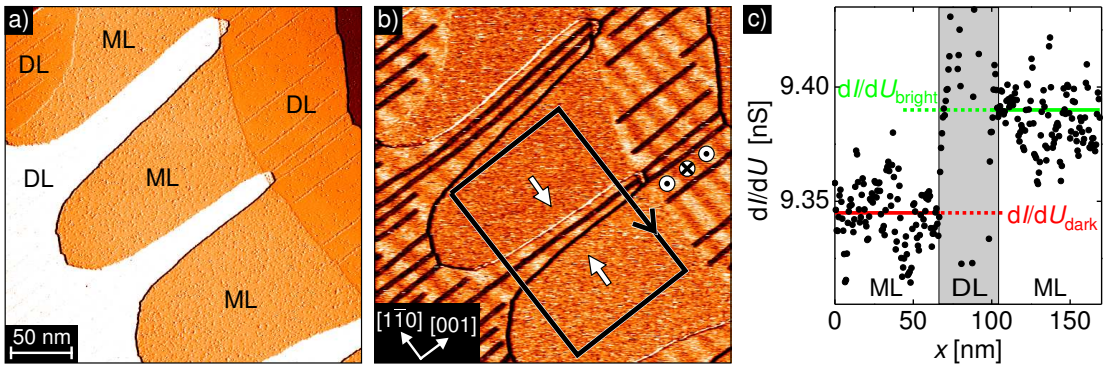

Figure 6.13: Magnetic imaging at T=184 K. (a) Topography image of the 1.5 ML Fe/W(110) system. Monolayer (ML) and double layer (DL) areas are visible. **(b)** Simultaneously recorded dI/dU map, revealing magnetic contrast on the ML domains and the DL domains. The magnetization structure on the ML and the DL is indicated. **(c)** Line section (black data points) across the two ML domains, averaged over the area marked in (b). The mean dI/dU signal averaged over the data points of the respective domain is indicated by the red and the green line. $U = +100$ mV, $I = 2$ nA, $T = 184$ K.

sensitivity of bulk Cr tips have been demonstrated. Bulk Cr tips can be used for investigations of surface magnetism over a wide temperature range.

6.7 Conclusion

By employing bulk Cr tips it is possible to detect all of the spatial magnetization directions provided by Fe mono- and double layers on W(110) over a wide bias voltage range, with tunable sensitivities to certain magnetization directions at appropriate sample bias voltages. In addition, bulk Cr tips exhibit an in-plane as well as an out-of-plane magnetic sensitivity over a wide temperature range.

Numerous control experiments have been performed at low temperatures by inserting different tips or applying short voltage pulses between the tip and the sample, leading to morphology, electronic, and magnetic alterations of the tip configuration. A magnetic contrast was always observable on all of the ML and DL features. It is characteristic that bulk Cr tips can never be purely in-plane or out-of-plane sensitive, but they exhibit a magnetization that is tilted in space. Their canted tip magnetization qualifies them for investigations on unknown magnetic configurations after characterization on a reference system like Fe/W(110).

The final tip preparation can be carried out *in situ* by applying short voltage pulses. Hence, in contrast to thin-film coated tips (cf. Se. 4.3), bulk Cr tips do not require an extensive *in situ* preparation. As a consequence, a tip exchange mechanism is no longer mandatory for SP-STM investigations using bulk Cr tips. This opens new perspectives for standard scanning tunneling microscopes, since any conventional STM can be extended by spin-sensitivity by employing a bulk Cr tip.

Chapter 7

Imaging and Switching Iron Nanomagnets by SP-SFEM

As discussed in Sec. 3.4.1, the combination of a point-like magnetic field emitter with a magnetic collector in an SP-STM setup has been reported recently [23]. The authors demonstrated that magnetic imaging mediated by exchange-split field-emission resonance (FER) states is possible by means of spin-polarized conductance measurements. Their spin-polarized scanning field emission microscopy (SP-SFEM) study was performed on a bulk-like Fe/W(110) surface. As demonstrated in Sec. 3.3, the evolution of the FER states is purely a surface effect. An electron in an FER state is multiply reflected at the vacuum and surface potential. Here, the spin-dependence of the FER state is only determined by the spin-dependent reflectivity of the surface (cf. Sec. 3.3.1 and Sec. 3.4.1). In principle, a single atomic layer of a magnetic material should be sufficient to generate an exchange splitting of the FER state energy. The question arises as to whether magnetic structures that are ultimately only one atomic layer thick can be imaged by SP-SFEM.

The spin-polarized field-emitted electrons penetrate the magnetic surface at relatively high energies compared to the Fermi level of the surface, as can be seen in Fig. 3.8. The interesting question is whether it is possible to detect inelastic interactions of spin-polarized field-emitted electrons with magnets by SP-SFEM and how the latter will be affected by spin-polarized field emission.

I used the sample system Fe/W(110) as in Ref.[23], but reduced the dimensions of the ferromagnet laterally from hundreds of nanometers down to a few nanometers and vertically from about 40 ML to 1 ML. The samples were the well-known Fe nanomagnets on W(110), which were introduced in Sec. 5.2.

7.1 Identification of field-emission resonance states

In order to identify the FER states of the system of Fe/W(110) nanoislands, a spectroscopy study has been performed on both the clean W(110) substrate as well as on the Fe nanoislands.

Generally, a spectroscopy experiment is realized by ramping the sample bias U from an initial to a final voltage and determining the differential conductance $\mathrm{d}I/\mathrm{d}U(U)$ by means of the lock-in technique. As discussed in Sec. 3.4, when ramping the sample bias U in field emission, the FER states give rise to peaks in the differential conductance $\mathrm{d}I/\mathrm{d}U(U)$. Whereas conventional low bias tunneling spectroscopy is performed at *constant height* revealing the surface LDOS at a certain distance to the surface (cf. Sec. 2.2.2), in field emission ramping the sample bias U at a fixed tip-sample distance d would result in a drastic increase in the electric field between the tip and the sample ($\propto U/d$). However, the energetic positions of the FER states are expected to depend crucially on the electric field (cf. Chap. 3). Hence, changing the electric field during spectroscopy would shift the FER states, making their detection unfeasible. Consequently, field-emission spectroscopy has to be performed at *constant electric field*.

According to Eq. 3.13 the current in the field emission regime depends solely on the electric field. Hence, keeping the *current constant* should in turn keep the electric field constant. Experimentally, this is realized by keeping the feedback on while ramping the sample bias from the initial to a final voltage [108, 131]. Hence, with increasing sample bias the tip is retracted from the surface in a way that keeps the current constant. In this way, the electric field between tip and sample is preserved approximately constant.

Here, the bias was ramped between $U = 1$ and 10 V at a fixed current of 2 nA and both the tip-sample distance variation $\Delta z(U)$ and the differential conductance $\mathrm{d}I/\mathrm{d}U(U)$ have been recorded simultaneously. The spectroscopy curves for the Fe/W(110) nanoisland and the W(110) substrate are shown in Fig. 7.1(a). For both Fe/W(110) and the W(110) substrate, $\Delta z(U)$ increases with increasing sample bias. In addition, a step-like behavior of $\Delta z(U)$ is observed, as shown in the top panel of Fig. 7.1(a). At the energetic positions of the steps in $\Delta z(U)$, peaks in the differential conductance $\mathrm{d}I/\mathrm{d}U(U)$ develop, as can be seen in the bottom panel of Fig. 7.1(a). The distance between successive peaks and steps decreases with increasing sample bias. Furthermore, the steps in $\Delta z(U)$ and peaks in $\mathrm{d}I/\mathrm{d}U(U)$ occur at different energetic positions for the Fe/W(110) nanoisland and the W(110) substrate.

As shown in the top panel of Fig. 7.1(a), the tip-sample distance $\Delta z(U)$ increases only slowly between $U = 1$ and ≈ 3 eV. At higher voltages the increase is considerable, which is a typical characteristic of the field emission regime in an STM setup [138]. Hence, the spectroscopy curves between $U = 1$ and 10 V show the transition between the tunneling regime at low bias and the field emission

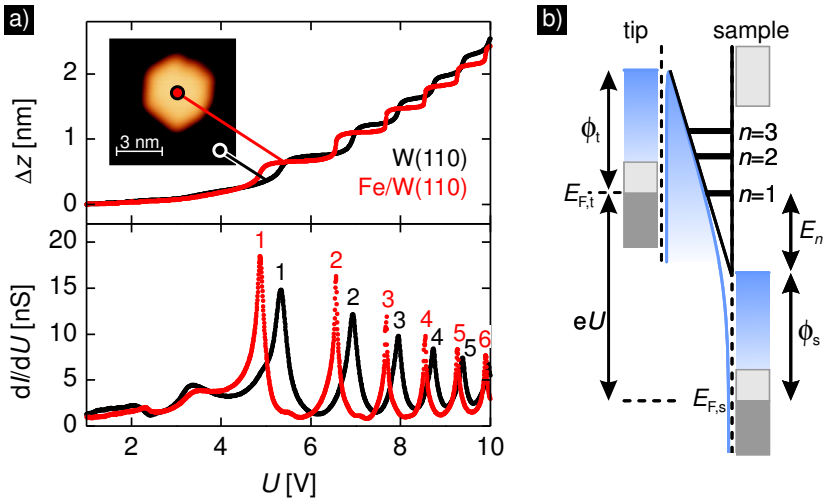

Figure 7.1: Field-emission resonance states on an iron island and the W(110) substrate. (**a**) $\Delta z(U)$ and $\mathrm{d}I/\mathrm{d}U(U)$ recorded above the island (red) and the substrate (black). Inset: Topography image. $U = 200\,\mathrm{mV}$, $I = 2\,\mathrm{nA}$, $T = 35.6\,\mathrm{K}$, bulk Cr-tip. (**b**) Schematic of the electronic confinement between tip and sample. The real potential well (blue line) is approximated by a triangular potential (black line). Energetic positions E_n of the FER states are indicated. ϕ_t, ϕ_s: work functions of tip and sample, $E_{\mathrm{F,t}}$, $E_{\mathrm{F,s}}$: Fermi levels of tip and sample.

regime at high bias voltages. In Fig. 7.1(a), an approximately linear behavior of $\Delta z(U)$ is observed at higher voltages. According to a theoretical study on the influence of the shape of the probe tip on the $\Delta z(U)$ characteristic in field emission [216], this indicates a relatively blunt probe tip generating a homogeneous electric field between the tip and the sample: Whereas a planar tip generates a linear behavior of $\Delta z(U)$ like a parallel plate capacitor, a spherical tip would induce an upward bending of $\Delta z(U)$ which would be the stronger the smaller the tip radius [216].

Increasing the sample bias from $U = 1\,\mathrm{V}$ to $10\,\mathrm{V}$ results in an overall increase of the tip-sample distance by $\Delta z \approx 2.5\,\mathrm{nm}$ (cf. Fig. 7.1(a)). So, in order to hold the same current value as in the tunnel contact at $U = 1\,\mathrm{V}$, the tip has to retract more than 2 nm in field emission. This is a significant increase in the tip-sample distance compared to tunneling experiments, where the distance is only a few Å. Tunneling experiments at low bias would not even be possible at this nanometer distance since the tunnel current I decreases by about one order of magnitude per Å [32], resulting in a decrease of the tunnel current by 20 orders of magnitude for an increase in the tip-sample distance by 2 nm.

In addition to the overall increase of the tip-sample distance with bias voltage, steps in $\Delta z(U)$ and peaks in the differential conductance $\mathrm{d}I/\mathrm{d}U(U)$ are observed, as shown in Fig. 7.1(a). As discussed in Sec. 3.4, whenever the sample bias coincides with the energetic position of an FER state during ramping, an additional transmission channel opens. This results in a drastic increase of the emission cur-

rent. As a consequence, the tip has to retract considerably in order to keep the current at $I = 2\,\mathrm{nA}$. Hence, the FER states give rise to a series of pronounced steps in $\Delta z(U)$. According to the additional transmission channel and the related increase of conductance, at each step a local maximum evolves in the $\mathrm{d}I/\mathrm{d}U(U)$ channel, as observed in the bottom panel of Fig. 7.1(a).

For the W(110) substrate there are five local maxima of the $\mathrm{d}I/\mathrm{d}U(U)$ signal in the energy window between 4 and 10 V corresponding to the first five FER states. On the Fe/W(110) island, in the same energy window, the first six FER states are observed. For both W(110) and Fe/W(110) the height and the width of the FER peaks decrease with increasing sample bias and order n. For example, on W(110) the full width at half maximum (FWHM) is 500 meV for $n = 1$ and 200 meV for $n = 5$. For Fe/W(110) the FWHM is 400 meV for $n = 1$ and 160 meV for $n = 5$. In conventional low bias inelastic electron tunneling spectroscopy the FWHM can be used to determine the intrinsic linewidth Γ of the electron excitation. Here, the experimentally observed linewidth is given by FWHM$= \sqrt{(1.7U_{\mathrm{mod}})^2 + (5.4k_{\mathrm{B}}T/\mathrm{e})^2 + \Gamma^2}$, where U_{mod} is the modulation voltage used for the lock-in technique, k_{B} is the Boltzmann constant and T is the temperature [217]. Applying this formula to the field-emission spectroscopy data with $U_{\mathrm{mod}} = 40\,\mathrm{mV}$ and $T = 36\,\mathrm{K}$ results in $\Gamma_{\mathrm{W(110)}} = 496\,\mathrm{meV}$ and $\Gamma_{\mathrm{Fe/W(110)}} = 395\,\mathrm{meV}$ for $n = 1$. However, from two-photon photoemission experiments the intrinsic linewidths of the $n = 1$ image-potential state (IPS) on W(110) and bulk Fe(110) are known to be a factor of 5 and 4 smaller [122, 218]. As discussed in Chap. 3, owing to the electric field in an STM setup these IPS are transformed into FER states Stark-shifted to higher energies, which is expected to result in a reduction of the lifetime and a concomitant linewidth broadening [22]. However, a combined two-photon photoemission and STM study [145, 219] revealed only a broadening by a factor of 2 due to the electric field, which has also been verified theoretically [22]. Here, the intrinsic linewidth of the first FER state in the STM setup was reliably determined by analyzing the phase coherence length of standing wave patterns. Interestingly, the linewidth of the same FER state on the same sample system determined from the peak in the spectroscopy data was also found to be broadened by a factor of 5 [220]. Consequently, the above FWHM formula for low bias constant height spectroscopy data is not valid for field-emission spectroscopy. Recently, a first attempt has been made to develop a qualitative understanding of the overall shape of the FER peaks in a $\mathrm{d}I/\mathrm{d}U(U)$ spectrum [220]. The authors expect the peak shapes to be strongly influenced by the dynamic constant-current measurement method. To date, the overall shape of the field emission $\mathrm{d}I/\mathrm{d}U(U)$ curve is not fully understood and simulating quantitatively such an FER spectrum is an ongoing challenge.

For both W(110) and Fe/W(110), the distance between two successive peaks in the $\mathrm{d}I/\mathrm{d}U(U)$ spectrum in Fig. 7.1(a) decreases with increasing order n. This can be understood within a simple model describing the vertical confinement of

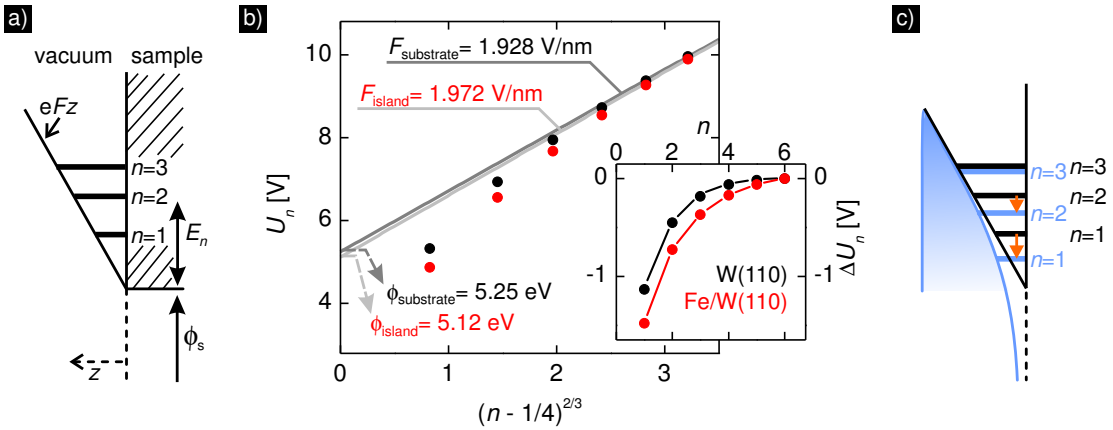

Figure 7.2: Determination of the electric field on the iron island and the W(110) substrate. (**a**) Sketch of a triangular potential well. The Eigenstates E_n are indicated. ϕ_s: sample work function. (**b**) Plot of the FER peak positions U_n on the island (red) and the substrate (black) as a function of $(n-1/4)^{2/3}$, n: FER quantum number. Lines indicate calculated peak positions $U_n^{\text{triangular}}$ according to Eq. 7.2 for the island (light grey) and the substrate (dark grey). Inset: Deviation ΔU_n of peak positions U_n from calculated positions $U_n^{\text{triangular}}$ as a function of n for the island (red) and the substrate (black). (**c**) Sketch of the vacuum potential given by the image potential and the applied electric field (blue line) and in the simplified case of a triangular potential well (black line). Respective Eigenstates E_n are indicated.

the FER states between the tip and the sample. The potential well given by the surface and the vacuum potential can be approximated by a triangular potential, as depicted in Fig. 7.1(b). As discussed in Sec. 3.3.2, the quantized energies E_n in a triangular potential scale with $n^{2/3}$ [124], and the distance between successive FER states is expected to decrease with order n within this approximation.

The differences in the spectra of W(110) and Fe/W(110) in terms of peak position and peak distances can also be understood within the simple model of a triangular potential. Its onset is given by the work function ϕ_s of the sample surface, as depicted in Fig. 7.1(b). Corresponding to the different work functions of W(110) and Fe/W(110), the electric field (represented by the slope of the potential) at a given distance from the surface differs. Consequently, the two materials generate different potential wells above the surface and thereby different resonance conditions for the FER states. The FER series starts at a lower energy on the Fe/W(110) nanoisland than on the W(110) substrate, indicating a lower work function ϕ_{island} on the island than on the substrate. The distances between successive FER peaks in the $\mathrm{d}I/\mathrm{d}U(U)$ spectrum on the Fe/W(110) nanoisland are larger than for the W(110) substrate indicating a higher electric field above the island.

The effective electric field above the Fe/W(110) nanoisland and the W(110) substrate can be determined from the spectra. By neglecting the influence of the

image potential and assuming an infinitely high potential barrier on the bulk side, the potential between the tip and the sample is approximated by a triangular potential well, whose slope is correlated to the electric field strength F according to Eq. 3.19, as depicted in Fig. 7.2(a). As discussed in Sec. 3.3.2, the solutions of the Schrödinger equation for the quantum-mechanical problem of an triangular potential well are Airy functions, whose Eigenvalues are given asymptotically for high n by Eq. 3.20. Adding the sample work function ϕ_s to the asymptotic solutions E_n of the Airy functions results in the energetic positions U_n of the FER peaks:

$$U_n = \frac{\phi_\mathrm{s}}{\mathrm{e}} + \alpha[n - \frac{1}{4}]^{\frac{2}{3}} F^{\frac{2}{3}} \,, \tag{7.1}$$

with $\alpha = \left(\frac{\hbar^2}{2 \cdot m \cdot \mathrm{e}}\right)^{\frac{1}{3}} \left(\frac{3\pi}{2}\right)^{\frac{2}{3}} = 4.39\,\mathrm{V}^{\frac{1}{3}}\mathrm{\AA}^{\frac{2}{3}}$ being a constant [130].

According to Eq. 7.1 plotting the FER peak positions U_n as a function of $[n - \frac{1}{4}]^{\frac{2}{3}}$ should result in a straight line, whose slope is proportional to $F^{\frac{2}{3}}$. Hence, the electric field strength F can be determined. In Fig. 7.2(b), the FER peak positions U_n for both the W(110) substrate and the Fe/W(110) nanoislands are plotted as a function of $[n - \frac{1}{4}]^{\frac{2}{3}}$. The experimental data do not show a linear dependance. Whereas the highest FER states almost lie on the line, the lower FER states are shifted considerably to lower energies. Obviously, a correction of the assumed triangular potential is needed for the low n states. As already discussed in Chap. 3, the image potential mainly influences the low n FER states, as their weight of the wavefunction is closest to the surface where the image potential is the strongest. As depicted in Fig. 7.2(c), the FER states with low quantum number n are thereby shifted to lower energies compared to their energetic position in a pure triangular potential, whereas the high n states remain unaffected. Consequently, the deviation of the low n FER peak positions U_n from the line is attributed to the influence of the image potential, that has been neglected in the model.

However, the influence of the image potential on the sixth FER state is expected to be very small and F can be calculated from the energetic position $U_{n=6}$ using Eq. 7.1. Above the W(110) substrate the electric field strength is $F_\mathrm{substrate} = (1.928 \pm 0.005)\,\mathrm{V/nm}$, assuming a work function $\phi_\mathrm{W(110)} = 5.25\,\mathrm{eV}$ [218]. For the Fe/W(110) nanoisland, with $\phi_\mathrm{Fe(110)} = 5.12\,\mathrm{eV}$ [122], $F_\mathrm{island} = (1.972 \pm 0.006)\,\mathrm{V/nm}$. Thus, the electric field strength above the Fe/W(110) nanoisland is slightly higher than on the W(110) substrate. With the respective value for ϕ and F Eq. 7.1 yields

$$\begin{aligned} U_n^\mathrm{triangular} &= 5.25\,\mathrm{V} + \alpha[n - \frac{1}{4}]^{\frac{2}{3}} (1.928\,\mathrm{V/nm})^{\frac{2}{3}} \text{ for W(110) , and} \\ U_n^\mathrm{triangular} &= 5.12\,\mathrm{V} + \alpha[n - \frac{1}{4}]^{\frac{2}{3}} (1.972\,\mathrm{V/nm})^{\frac{2}{3}} \text{ for Fe/W(110) .} \end{aligned} \tag{7.2}$$

$U_n^\mathrm{triangular}$ indicates the peak positions of the FER states in the case of a purely triangular potential with the corresponding electric field strength $F_\mathrm{island/\,substrate}$.

It is plotted as a straight line for both the W(110) substrate and the Fe/W(110) nanoisland in Fig. 7.2(b). Defining

$$\Delta U_n = U_n - U_n^{\text{triangular}} \tag{7.3}$$

gives the deviation of the data points U_n from their expected positions $U_n^{\text{triangular}}$ in a pure triangular potential according to Eq. 7.2. ΔU_n is shown in the inset of Fig. 7.2(b) for both the W(110) substrate and the Fe/W(110) nanoisland. It is a measure of the modification of the FER state of order n by the image potential. For both, ΔU_n is considerably high for $n = 1$ but decreases quickly with increasing order n. This is reasonable, as the influence of the image potential is expected to decrease with order n resulting in a dominating electric field for high n.

As shown in the inset of Fig. 7.2(b), the absolute value of ΔU_n is larger for the Fe/W(110) nanoisland than for the W(110) substrate. Hence, the low FER states of the nanoisland are shifted to lower energies than the FER states of the substrate. This indicates, that the image potential of the Fe/W(110) nanoisland has a stronger influence on the FER states than the image potential of the W(110) substrate.

In summary, the FER states – though being located nanometer distances away from the surface in vacuo – are strongly influenced by the local electronic properties of the surface and the respective potential landscape in front of the surface. Consequently, a monolayer island consisting of only about 60 iron atoms exhibits a completely different FER spectrum to that of the tungsten substrate.

7.1.1 Spin-resolved spectroscopy

Along with the strong influence of the local electronic properties also the magnetic properties of the nanoisland are expected to have an influence on the FER states. The question arises whether it is actually possible to detect experimentally any exchange splitting of the FER states above the nanomagnet.

In Fig. 7.3(a) a topography of an individual Fe nanomagnet on a clean W(110) substrate textured with a magnetic map is shown. On the nanomagnet a typical stripe pattern is observed. As explained in Chap. 5, it reflects the thermally-induced magnetization switching between two states (0 and 1) when imaged line by line.

As sketched in Fig. 7.3(a), the magnetic tip has been positioned above the center of the nanomagnet and spin-resolved field-emission spectroscopy has been performed. To identify the FER states of the nanomagnet, the bias is ramped between $U = 1$ and 10 V at a fixed current of 2 nA. Recording both the tip-sample distance variation $\Delta z(U)$ and the differential conductance $\mathrm{d}I/\mathrm{d}U(U)$ reveals six steps in $\Delta z(U)$ along with six peaks in $\mathrm{d}I/\mathrm{d}U(U)$, as can be seen in Fig. 7.3(b). As already discussed in Sec. 7.1, they indicate the first six FER states on the nanomagnet.

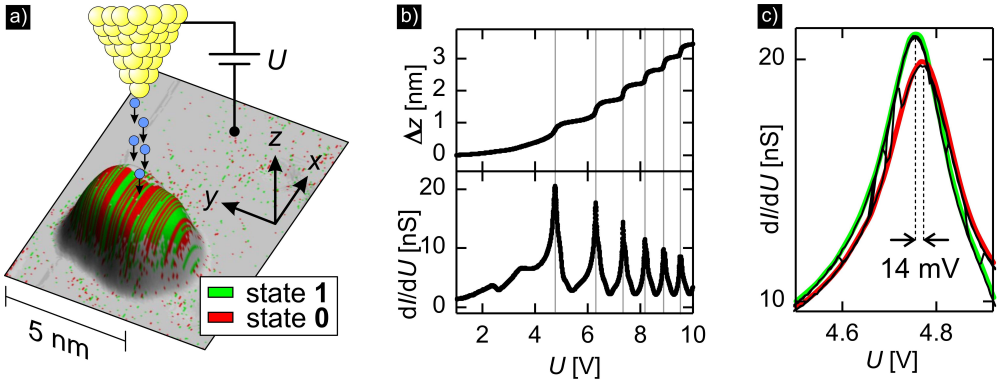

Figure 7.3: Spin-resolved field-emission resonance states on an iron nanomagnet (**a**) Sketch of the experimental setup and topography of a Fe/W(110) nanomagnet, textured with a magnetic map. The nanomagnet frequently switches between two states (red and green). The fast scanning direction of the tip is along x. (**b**) $\Delta z(U)$ and $\mathrm{d}I/\mathrm{d}U(U)$, revealing the first six field emission resonances. (**c**) First FER peak. It changes as the nanomagnet switches its magnetization. $I = 2\,\mathrm{nA}$, $T = 38.8\,\mathrm{K}$, Cr/W-tip.

The first FER peak is shown in Fig. 7.3(c) in more detail. Several $\mathrm{d}I/\mathrm{d}U$ spectroscopy curves are taken, each of them exhibiting sudden jumps. Plotting them on top of each other reveals that two peaks can be constructed, with the signal jumping between them. The jumping rate is comparable to the switching rate of the nanomagnet as observed from its switching behavior when imaged line by line in Fig. 7.3(a). Consequently, the jumps indicate switching events of the nanomagnet, with the FER peak slightly changing in terms of position and height. This finding indicates a significant overlap of two exchange-split FER peaks that reflect the magnetization of the underlying nanomagnet. Due to their strong overlap, both FER spin states are accessible for a fixed energy by the respective spin-polarized field-emitted electrons. A strong overlap has also been observed for exchange-split image-potential states. For example, on a bulk Fe(110) surface, spin-resolved inverse photoemission measurements have revealed a linewidth of $(140 \pm 10)\,\mathrm{meV}$ for the spin $\downarrow$ state and $(70 \pm 10)\,\mathrm{meV}$ for the spin $\uparrow$ state, whereas the binding energies are only split magnetically by $(57 \pm 5)\,\mathrm{meV}$ [115].

As shown in Fig. 7.3(c), an effective splitting $\Delta E_{\downarrow\uparrow}^{\mathrm{exp}}$ can be determined from the shifting of the peak position, resulting in about 14 meV. Consequently, the FER state of atomic-scale iron magnets already exhibit a significant exchange splitting.

Above the bulk-like Fe(110) surface, spin-polarized field-emission spectroscopy in an SP-STM setup revealed a $\Delta E_{\downarrow\uparrow}^{\mathrm{exp}} = 25\,\mathrm{meV}$ [23], whereas photoemission experiments on the same system yield values ranging from $(57 \pm 5)\,\mathrm{meV}$ [115] to $(85 \pm 20)\,\mathrm{meV}$ [218]. Consequently, the exchange splitting found in SP-SFEM is about 40 to 30 % smaller, though the applied electric field in SP-SFEM is expected to increase the splitting compared to the field-free case in photoemission

experiments (see Sec. 3.3.3). On the pseudomorphically grown monolayer island, the exchange splitting of the first FER state may differ from the value on the bulk Fe(110) surface, since a different spin-dependent electronic structure of the nanoisland will result in a different spin-dependent behavior of the FER state (cf. Sec. 3.3.1 and Sec. 3.3.3). After pulsing the probe tip and again determining the exchange splitting of the first FER above the same nanomagnet, $\Delta E_{\downarrow\uparrow}^{\mathrm{exp}} = 24\,\mathrm{meV}$ was found. Obviously, the experimentally determined value of $\Delta E_{\downarrow\uparrow}^{\mathrm{exp}}$ in SP-SFEM depends on the configuration of the individual probe tip, and in particular on the spin polarization of the tip.

The influence of the spin polarization of the tip and the relationship between the intrinsic and the experimentally determined exchange splitting is illustrated in Fig. 7.4. If only spin ↑ (or spin ↓) electrons are available, as in the case of a total spin polarization, pure spin ↑ (spin ↓) FER states are probed, as depicted in Fig. 7.4(a). The intrinsic exchange splitting $\Delta E_{\downarrow\uparrow}$ between both can be determined. As discussed above, the exchange-split FER states exhibit a significant overlap and at a given energy both are accessible to the respective spin-polarized field-emitted electrons. Hence, probing with an unpolarized tip results in only one spin-averaged FER peak with its maximum lying in the middle of the exchange-split FER states, as depicted in Fig. 7.4(b). The situation for a finite tip polarization is shown in Fig. 7.4(c). According to the spin polarization, the contributions of the spin ↑ and spin ↓ state are weighted, resulting in an FER peak whose maximum is shifted with respect to the pure spin ↑ and spin ↓ peaks, for example being closer to the spin ↑ maximum. By inverting the spin polarization, the weighting

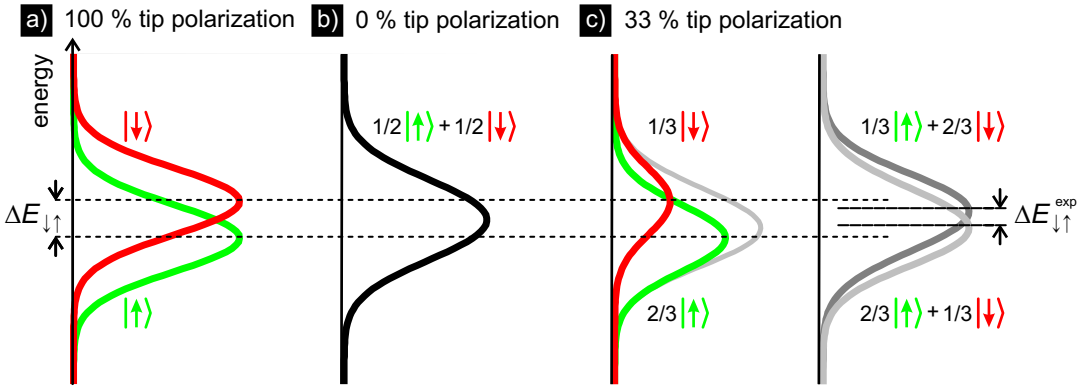

Figure 7.4: Relation of intrinsic and experimentally determined exchange splitting of FER states. (**a**) Sketch of the resulting spin ↑ (green) and spin ↓ (red) FER peaks when probed with a 100 % tip spin polarization. The spin-splitting $\Delta E_{\downarrow\uparrow}$ can be determined. (**b**) A vanishing tip polarization results in a spin-averaged FER peak. (**c**) With a finite spin polarization, the contributions of the spin ↑ and spin ↓ state are weighted accordingly, resulting in an FER peak e.g. being closer to the spin ↑ maximum (light grey). Inverting the polarization results in an FER peak e.g. being closer to the spin ↓ maximum (dark grey). The spin-splitting $\Delta E_{\downarrow\uparrow}^{\mathrm{exp}}$ of these two FER peaks (right) is smaller than $\Delta E_{\downarrow\uparrow}$ (left).

of the two spin channels is inverted, resulting in an FER peak that is now closer to the spin ↓ maximum. Consequently, the splitting $\Delta E_{\downarrow\uparrow}^{\mathrm{exp}}$ of these two resulting FER peaks is smaller than the intrinsic exchange splitting $\Delta E_{\downarrow\uparrow}$. As a result, the value of the FER exchange splitting determined by SP-SFEM depends critically on the individual tip polarization.

However, with knowledge of the spin polarization, the intrinsic exchange splitting can be estimated from the experimental value: In a small energy window around the maximum of the peak, the $\mathrm{d}I/\mathrm{d}U$ signal can be approximated by a parabola:

$$f_{\pm}(E) = b - a\left(E \pm \frac{\Delta E_{\downarrow\uparrow}}{2}\right)^2 \quad , \tag{7.4}$$

where b and a are constants and $E = \mathrm{e}U$ is the energy. The two intrinsic peaks $f_{\pm}$ contribute to the experimentally probed peaks g_+ and g_- according to the tip polarization P:

$$g_{\pm} = \frac{1+P}{2} f_{\pm} + \frac{1-P}{2} f_{\mp} \ . \tag{7.5}$$

The experimentally observed exchange splitting $\Delta E_{\downarrow\uparrow}^{\mathrm{exp}}$ is determined by the separation of the maxima of g_+ and g_-, resulting in $\Delta E_{\downarrow\uparrow}^{\mathrm{exp}} = P\Delta E_{\downarrow\uparrow}$. Hence,

$$\Delta E_{\downarrow\uparrow} = P^{-1}\Delta E_{\downarrow\uparrow}^{\mathrm{exp}} \ . \tag{7.6}$$

On the thermally switching Fe/W(110) nanomagnet the tip-sample distance varies by $\Delta z = (12 \pm 2)\,\mathrm{pm}$ according to its magnetic orientation with respect to the stable tip magnetization. According to Ref. [33] $\phi = 3.1\,\mathrm{eV}$ is a typical apparent barrier height for a Cr/W-tip and an Fe/W(110) nanomagnet [33], so the effective spin polarization $P = \tanh(1.025\,\mathrm{eV}^{-1/2}\mathrm{\AA}^{-1}\sqrt{\phi}\Delta z/2)$ [46] can be determined, resulting in $P = (0.11 \pm 0.02)$. With this estimate for P and $\Delta E_{\downarrow\uparrow}^{\mathrm{exp}} = (14.2 \pm 0.2)\,\mathrm{meV}$, the intrinsic exchange splitting of the first FER state above the Fe nanoisland can be estimated to $\Delta E_{\downarrow\uparrow} = (135 \pm 23)\,\mathrm{meV}$.

As mentioned above, photoemission experiments on a bulk Fe(110) surface found values for $\Delta E_{\downarrow\uparrow}$ ranging from $(57 \pm 5)\,\mathrm{meV}$ [115] to $(85 \pm 20)\,\mathrm{meV}$ [218]. In contrast to SP-SFEM experiments, photoemission experiments are performed *without* an electric field [25]. As the electric field is expected to increase the exchange splitting (cf. Sec. 3.3.3), the values determined in SP-SFEM cannot be directly compared to the results of photoemission experiments. However, Hanuschkin *et al.* have calculated the exchange splitting of FER states on the Fe(110) surface as a function of the electric field [125]. As discussed in Sec. 7.1, the electric field between the tip and the sample can be estimated using Eq. 7.1. On this particular Fe/W(110) nanomagnet, $U_{n=6} = 9.51\,\mathrm{V}$, resulting in $F = 1.7\,\mathrm{V/nm}$. At this field strength, the authors found $\Delta E_{\downarrow\uparrow} \approx 200\,\mathrm{meV}$. Consequently, the exchange splitting of the first FER state on the Fe nanoisland is similar to that on the bulk Fe(110) surface. Hence, reducing the dimensions of

a bulk ferromagnet to one monolayer vertically and a few tens of atoms laterally does not significantly reduce the exchange splitting of the FER states.

7.2 Magnetic imaging of iron nanomagnets

In Fig. 7.3(c) it has been shown, that the FER peak above the Fe/W(110) nanomagnet changes slightly in terms of position and height when the underlying nanomagnet switches its magnetization. Hence, at a fixed sample bias U the $\mathrm{d}I/\mathrm{d}U$ signal within the exchange-split FER peaks depends on the relative orientation of the stable tip magnetization and the actual magnetization of the nanomagnet. The question arises whether this difference in the $\mathrm{d}I/\mathrm{d}U$ signal on the nanomagnets at a fixed sample bias is adequate for magnetic imaging.

An overview magnetic $\mathrm{d}I/\mathrm{d}U$ map around the nanomagnet of Fig. 7.3 has been recorded with spin-polarized tunneling electrons at $U = 100\,\mathrm{mV}$. It is shown in Fig. 7.5(a). On the nanomagnets a typical stripe pattern is observed. As explained in Chap. 5, it reflects the thermally-induced magnetization switching between two states when imaged line by line. As the switching frequency depends on the island size and shape, each nanomagnet exhibits its own characteristic stripe widths. A line section taken across the center nanomagnet is shown in Fig. 7.5(b). On the nanomagnet, two discrete conductance levels are found, as shown in the inset of

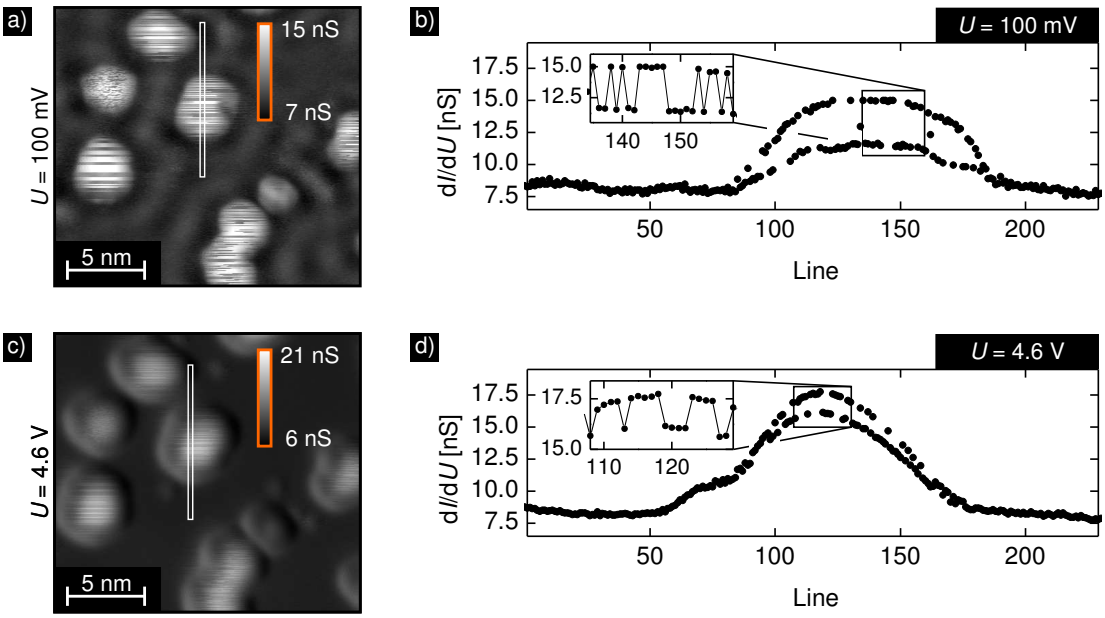

Figure 7.5: Magnetic imaging by SP-STM and SP-SFEM. $\mathrm{d}I/\mathrm{d}U$-map recorded with (**a**) spin-polarized tunneling electrons at $U = 100\,\mathrm{mV}$ and (**c**) spin-polarized field-emitted electrons at $U = 4.6\,\mathrm{V}$. The fast scanning direction is horizontal, the slow scanning direction vertical. (**b**) and (**d**) $\mathrm{d}I/\mathrm{d}U$ line sections along the boxes in (a) and (c). $I = 2\,\mathrm{nA}$, $T = 38.8\,\mathrm{K}$, Cr/W-tip.

Fig. 7.5(b). They reflect the actual magnetic orientation of the nanomagnet with respect to the stable tip magnetization. Here, each data point represents a line scan along the horizontal direction in Fig. 7.5(a). Hence, the line section across the nanomagnet indicates the nanomagnet being in the antiparallel configuration for some scan lines, switching to the parallel configuration for some subsequent scan lines and so forth.

The same sample area has been imaged with spin-polarized field-emitted electrons at $U = 4.6\,\mathrm{V}$. The resulting map of the spin-polarized field emission conductance $\mathrm{d}I/\mathrm{d}U$ is shown in Fig. 7.5(c). The nanomagnets appear blurred with no clear border to the surrounding substrate. However, in the center of the nanomagnets a faint stripe pattern is visible, reflecting the change of magnetization between the tip and the sample while recording the image line by line. A line section taken across the center nanomagnet is shown in Fig. 7.5(d). The inset in Fig. 7.5(d) clearly reveals that two conductance levels are found on the nanomagnet, indicating that the magnetization switches while scanning line by line.

Figure 7.5(d) also indicates that the spin-averaged contribution to the field emission conductance $\mathrm{d}I/\mathrm{d}U$ changes significantly both between the nanomagnet and the substrate and also on the nanomagnet. The magnetic contribution causes only a small additional variation of the $\mathrm{d}I/\mathrm{d}U$ signal on the island, resulting in the faint stripe pattern in the $\mathrm{d}I/\mathrm{d}U$ map. The line section of the SP-STM map shown in Fig. 7.5(b) reveals that the spin-averaged contribution to the tunneling conductance $\mathrm{d}I/\mathrm{d}U$ changes only slightly within the nanomagnet. As a result, the magnetic switching is clearly visible and the nanomagnets appear as pronounced islands clearly separated from the surrounding substrate in the SP-STM $\mathrm{d}I/\mathrm{d}U$-map of Fig. 7.5(a). In the SP-SFEM image of Fig. 7.5(c) the strong lateral variation of the field emission conductance $\mathrm{d}I/\mathrm{d}U$ results in a blurry appearance of the nanoislands.

The differences in the appearance of the nanoislands in the two $\mathrm{d}I/\mathrm{d}U$-maps reflect the different imaging techniques. SP-STM uses tunneling electrons, that are mainly influenced by the local electronic density of states at the Fermi level of the surface (see Sec. 2.2.1). The latter changes on an atomic scale between the substrate and the nanoisland but stays approximately constant over the island. In contrast, imaging in SP-SFEM is mediated by the FER states located in vacuo above the sample. They are influenced mainly by the local electronic surface potential [221] (cf. Sec. 3.3). As shown in Sec. 7.1, the work functions of the substrate and the nanomagnets differ significantly. In order to fulfill the continuity conditions, the corresponding lateral potential landscape has to change smoothly, and so do the FER states. Hence, along with the energetic position of the FER peak also the corresponding emission conductance $\mathrm{d}I/\mathrm{d}U$ depends on the local surface potential. Consequently, the $\mathrm{d}I/\mathrm{d}U$ signal in the SP-SFEM image is dominated by contributions from spin-independent electronic features. Never-

theless, the magnetic information is available in the spin-polarized field emission conductance.

Generating magnetic maps in SP-SFEM

As discussed above, the conductance $\mathrm{d}I/\mathrm{d}U$ may be influenced, or even dominated, by spin-independent contributions reflecting the site-dependent electronic configuration between the tip and the sample. However, when the magnetization of the sample switches frequently, a magnetic map can be derived from the raw data, shown in Fig. 7.6(a). In order to separate the spin-independent contributions to $\mathrm{d}I/\mathrm{d}U$ from purely magnetic features, a Savitzky-Golay smoothing filter is applied perpendicular to the fast scanning direction. The result is shown in

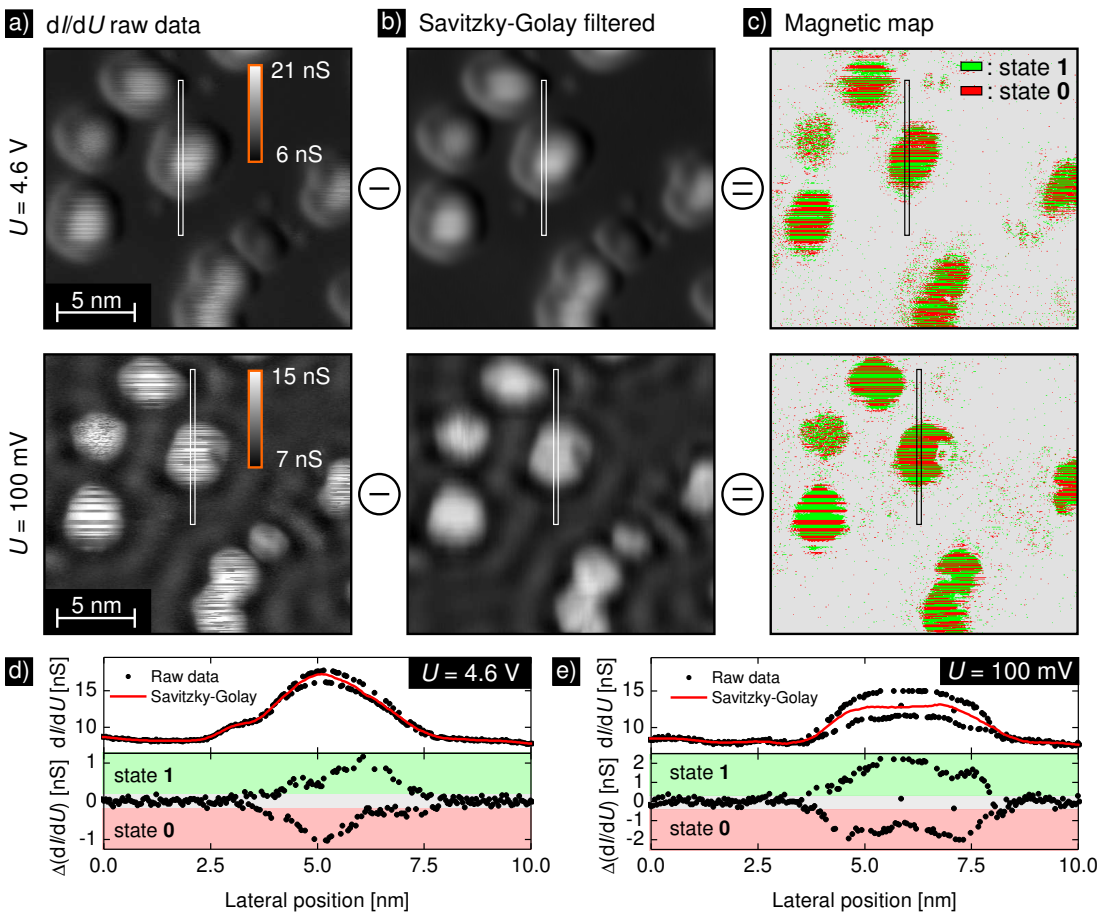

Figure 7.6: Generating magnetic maps. (**a**) $\mathrm{d}I/\mathrm{d}U$ raw data, (**b**) non-magnetic map resulting from filtering and (**c**) color-coded purely magnetic map, representing the subtraction of the filtered data from the raw data for SP-SFEM (top) and SP-STM (bottom). (**d**) and (**e**) $\mathrm{d}I/\mathrm{d}U$ line sections along the boxes in (a): Raw data (black dots) and filtered data (red line) (top panel), and the difference signal (bottom panel). $I = 2\,\mathrm{nA}$, $T = 38.8\,\mathrm{K}$, Cr/W-tip.

Fig. 7.6(b). The filtered data represent the spin-independent, purely electronic contributions to the $\mathrm{d}I/\mathrm{d}U$ signal. As discussed above, in SP-SFEM the site-dependent electronic configuration between the tip and the sample is mainly determined by the local electronic potential. Hence, Fig. 7.6(b) represents a map of the local effective potential variation between the tip and the sample. Subtracting this image of non-magnetic features from the raw data yields the magnetic map, shown in Fig. 7.6(c). The difference signal is $\approx 0\,\mathrm{nS}$ on the substrate. This indicates that on the W(110) substrate there are only spin-independent, purely electronic contributions to the $\mathrm{d}I/\mathrm{d}U$ signal, which is expected as W(110) is non-magnetic. On the nanomagnets the difference signal jumps between positive and negative values, reflecting the magnetization switching of the nanomagnets. This can also be seen in the line section in Fig. 7.6(d). Map regions with the difference signal exceeding a certain threshold around zero are denoted as state 1 (positive values) or state 0 (negative values), respectively. For comparison, the same procedure is applied to the $\mathrm{d}I/\mathrm{d}U$ raw data taken with spin-polarized tunneling electrons at $U = 100\,\mathrm{mV}$, see the lower images in Fig. 7.6(a-c). Again a Savitzky-Golay filter is applied perpendicular to the fast scanning direction, and subtracting the result from the raw data yields the magnetic map. Figure 7.6(d) shows a line section, where the difference signal is again $\approx 0\,\mathrm{nS}$ on the substrate, with jumps between positive and negative values on the nanomagnet due to its switching. Applying the same procedure as for the SP-SFEM magnetic map, the stripe pattern on the nanomagnets is clearly visible in Fig. 7.6(c).

7.2.1 Comparison with SP-STM

Deriving the purely magnetic information by generating magnetic maps from SP-SFEM and SP-STM $\mathrm{d}I/\mathrm{d}U$ signals allows the two magnetic imaging methods to be compared. Figure 7.7(a) shows an SP-SFEM magnetic map textured onto the topography taken with spin-polarized field-emitted electrons at $U = 4.6\,\mathrm{V}$. For comparison, an SP-STM image of the same area taken with tunneling electrons at $U = 100\,\mathrm{mV}$ is shown in Fig. 7.7(b). In both images, the substrate shows no magnetic features, whereas the characteristic magnetic stripe pattern can be seen on each of the nanomagnets.

As can be seen in the zoom of Fig. 7.7(c), the corrugation is slightly enhanced in the SP-SFEM topography. As extracted from the line sections of Fig. 7.7(c), the lateral dimension is offset by about 1 nm, and the effective corrugation is increased by a factor of 1.5 for $U = 4.6\,\mathrm{V}$. At $U = 4.6\,\mathrm{V}$ imaging is performed at a sample bias that coincides with the FER peak on the nanomagnets, whereas the FER peak position on the substrate is offset by about $0.5\,\mathrm{V}$ (cf. Fig. 7.1). Consequently, when the probe tip scans the sample, the conductance drastically increases when approaching a nanomagnet, provoking an anomalously strong tip retraction at the edge of the nanomagnet. Likewise, the probe tip has to considerably approach the

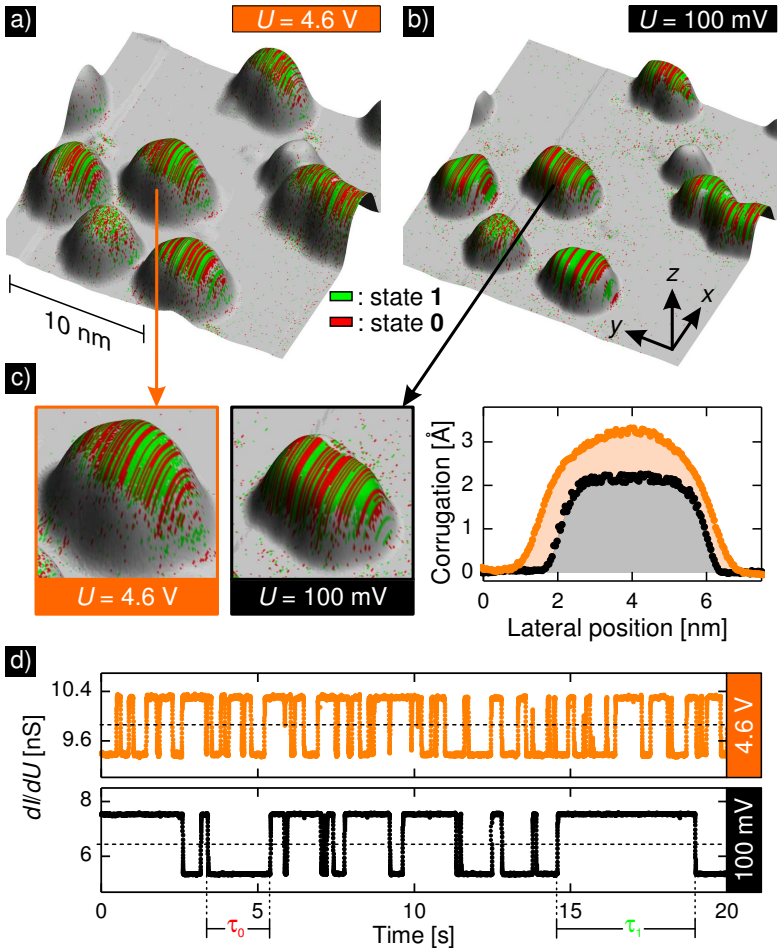

Figure 7.7: Comparison of the magnetic imaging by SP-SFEM and SP-STM. (**a**) SP-SFEM topography and magnetic map, recorded at $U = 4.6\,\mathrm{V}$. (**b**) SP-STM topography and magnetic map, recorded at $U = 100\,\mathrm{mV}$. Characteristic stripe patterns evolve on the nanomagnets. (**c**) Zoom to one nanomagnet, imaged by SP-SFEM (left) and conventional SP-STM (right). The topography line sections show an increase in apparent height and lateral dimensions. $I = 2\,\mathrm{nA}$, $T = 38.8\,\mathrm{K}$. (**d**) Trace section of the magnetic telegraph noise recorded on the nanomagnet of c) using SP-SFEM (top) and SP-STM (bottom). $I = 2\,\mathrm{nA}$, $T = 39.4\,\mathrm{K}$, Cr/W-tip.

substrate when leaving the nanomagnet, as the conductance drops drastically on the substrate. Hence, the anomalous corrugation of the nanomagnets results from their resonant imaging whereas the tungsten substrate is imaged off-resonance. Such a dependence of the corrugation on the field emission resonance condition has been observed also in other sample systems [141, 142].

In order to compare the signal quality of SP-SFEM to that in conventional SP-STM, the magnetic tip is positioned stationary above the nanomagnet shown in Fig. 7.7(c). Recording the magnetic $\mathrm{d}I/\mathrm{d}U(t)$ signal as a function of time t

allows for the observation of the temporal magnetization evolution, as can be seen in Fig. 7.7(d). Two sections of the $\mathrm{d}I/\mathrm{d}U(t)$ raw signal are shown, one recorded by SP-SFEM using field-emitted electrons, and one by conventional SP-STM using low-energy tunneling electrons. A characteristic telegraph noise is observed, with the signal changing abruptly between two discrete conductance levels (state 0 and state 1) reflecting the island magnetization switching from the parallel to the antiparallel configuration and vice versa with respect to the stable tip magnetization.

7.2.2 Magnetic imaging using higher order FER states

In Fig. 7.8(a), field-emission spectroscopy has been performed on the nanomagnet of Fig. 7.7(c), revealing three FER peaks in the $\mathrm{d}I/\mathrm{d}U$ signal. In addition to the first FER peak discussed before, the second and the third FER peak also exhibit a small but distinct exchange splitting, that allow for magnetic imaging. In Fig. 7.8(b) the magnetic tip is positioned stationary above the nanomagnet and the conductance $\mathrm{d}I/\mathrm{d}U(t)$ is recorded as a function of time using SP-STM at $U = 100\,\mathrm{mV}$ and SP-SFEM at $U = 4.9\,\mathrm{V}$, $U = 6.1\,\mathrm{V}$ and $U = 7.2\,\mathrm{V}$, which coincides with the flank of the first, second and third FER peak, respectively, as marked in Fig. 7.8(a). The characteristic magnetic telegraph noise is observed for all cases. All three exchange-split FER peaks allow for high-quality magnetic imaging with a very good signal-to-noise ratio. Note that the tip-sample distance

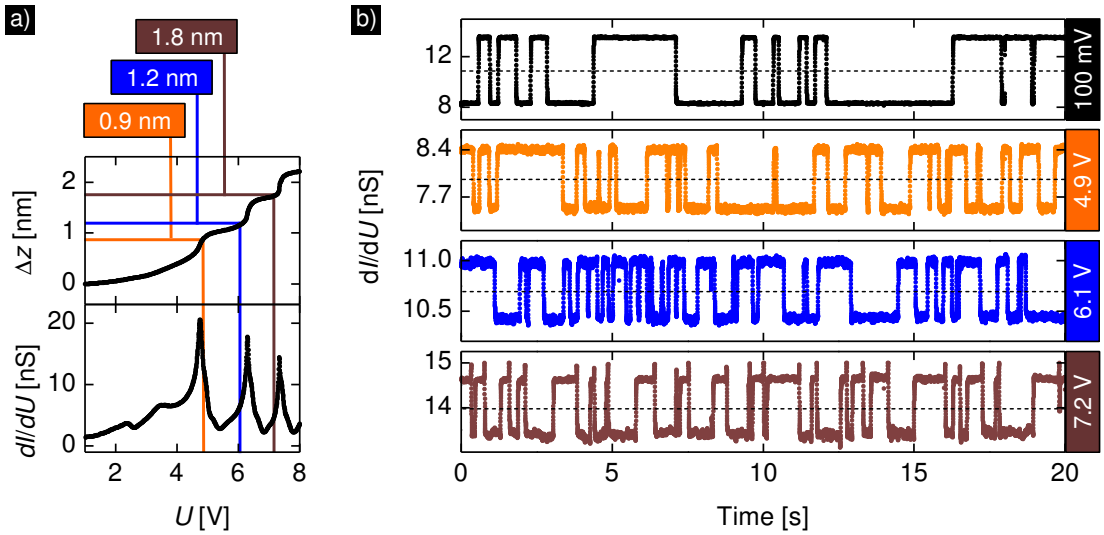

Figure 7.8: Magnetic imaging at large tip-sample distances. (**a**) Field-emission spectroscopy $\Delta z(U)$ and $\mathrm{d}I/\mathrm{d}U(U)$, revealing the first three FER peaks. (**b**) Trace section of the magnetic telegraph noise recorded on the nanomagnet using SP-STM at $U = 100\,\mathrm{mV}$ and SP-SFEM at $U = 4.9\,\mathrm{V}$, $U = 6.1\,\mathrm{V}$ and $U = 7.2\,\mathrm{V}$ (from top to bottom). The tip-sample distance increases thereby up to $\Delta z \approx 2\,\mathrm{nm}$. $I = 2\,\mathrm{nA}$, $T = 38.8\,\mathrm{K}$, Cr/W-tip.

has been increased by up to 2 nm for recording the telegraph noise for the third FER, as extracted from $\Delta z(U)$ in Fig. 7.8(a). Consequently, the exchange splitting of higher order FER states permits magnetic imaging at nanometer distances.

7.3 Interaction of iron nanomagnets with field-emitted electrons

On closer inspection of the magnetic telegraph noise shown in Fig. 7.7(d) more switching events within the same time are visible when imaging the switching behavior of the nanomagnet with spin-polarized field-emitted electrons. This indicates an increase in the switching frequency of the nanomagnet when injecting spin-polarized field-emitted electrons. Hence, spin-polarized field emission seems to affect the nanomagnet thereby modifying its switching behavior.

7.3.1 Joule heating generated by field-emitted electrons

In my experiment the probe tip is positioned above the center of an individual Fe/W(110) nanomagnet and the magnetic $\mathrm{d}I/\mathrm{d}U$ signal is recorded as a function of time with low-energy tunneling electrons. As shown in Fig. 7.9(a), 25 switching events are visible.

Imaging the switching behavior with field-emitted electrons reveals that the nanomagnet switched 54 times within the same time frame, as shown in Fig. 7.9(b). Consequently, recording the telegraphic noise of the nanomagnet with field-emitted electrons results in a considerable reduction of the mean lifetime.

As the mean lifetime depends strongly on the temperature I suppose the nanomagnet is being effectively heated by the field-emitted electrons. Indeed, increasing the sample temperature by $\Delta T = 1\,\mathrm{K}$ results in the same switching behavior as observed before (Fig. 7.9(c)). Hence, changing from low-energy tunneling electrons to higher energy field-emitted electrons by increasing the sample bias affects the magnetic switching behavior in the same way as increasing the nanomagnet's temperature.

To account for the observed effective heating within the framework of the macrospin model, the Néel-Brown law (Eq. 5.1) is expanded. The mean lifetime $\bar{\tau}(U)$ is given by

$$\bar{\tau}(U) = \nu_0^{-1} \exp\left(\frac{E_\mathrm{b}}{k_\mathrm{B}(T + \Delta T(U))}\right), \tag{7.7}$$

with $\Delta T(U)$ being the effective temperature increase of the nanomagnet.

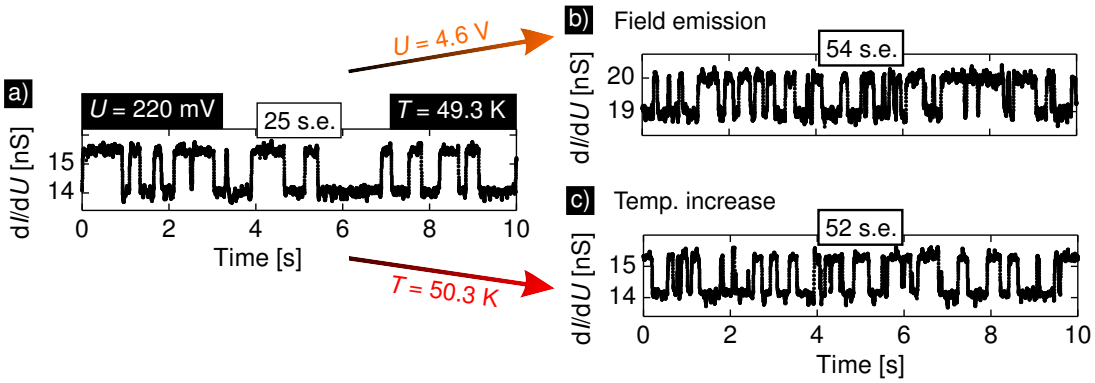

Figure 7.9: Trace sections of the magnetic $\mathrm{d}I/\mathrm{d}U$ signal. **(a)** $U = 220\,\mathrm{mV}$ at $T = 49.3\,\mathrm{K}$. 25 switching events (s.e.) are observable. **(b)** $U = 4.6\,\mathrm{V}$ at the same temperature as in (a). 54 s.e. are observable. **(c)** $U = 220\,\mathrm{mV}$ at $T = 50.3\,\mathrm{K}$. 52 s.e. are observable. $I = 2\,\mathrm{nA}$, Cr/W-tip.

Combining Eq. 5.1 and Eq. 7.7 allows $\Delta T(U)$ generated by field-emitted electrons to be calculated:

$$\Delta T(U) = \left(\frac{1}{T} + \frac{k_\mathrm{B}}{E_\mathrm{b}} \ln \frac{\bar{\tau}(U)}{\bar{\tau}_\mathrm{i}} \right)^{-1} - T, \tag{7.8}$$

where $\bar{\tau}_\mathrm{i}$ is the intrinsic mean lifetime. It is determined from the telegraph noise recorded at low bias using tunneling electrons in the STM.

Lifetime analysis

For the quantification of $\Delta T(U)$ the mean lifetimes $\bar{\tau}(U)$ and $\bar{\tau}_\mathrm{i}$ as well as the energy barrier E_b have to be known. These characteristic quantities can be determined by a lifetime analysis.

The probe tip is positioned above the center of the nanomagnet and the magnetic $\mathrm{d}I/\mathrm{d}U$ signal is recorded as a function of time with low-energy tunneling electrons, as shown for example in Fig. 7.10(a). The lifetime τ between two consecutive switching events is determined for the whole data set in order to plot a histogram, as shown in Fig. 7.10(b). Approximately a thousand switching events have to be recorded to get good statistics in the lifetime distribution. Similar to radioactive decay, the lifetime distribution can be described by an exponential decay law, and fitting the data results in the mean lifetime $\bar{\tau}$. This procedure for determining the lifetime is then repeated at different temperatures. From the mean lifetimes at different temperatures E_b is determined from Eq. 5.1.

For the data presented in Fig. 7.9, a detailed lifetime analysis of the whole data set has been performed. According to Eq. 7.8 with $\bar{\tau}_\mathrm{i} = (370 \pm 18)\,\mathrm{ms}$, $\bar{\tau}(U = 4.6\,\mathrm{V}) = (185 \pm 10)\,\mathrm{ms}$ and $E_\mathrm{b} = (160 \pm 2)\,\mathrm{meV}$, the effective temperature increase of the nanomagnet due to the field-emitted electrons is found to be

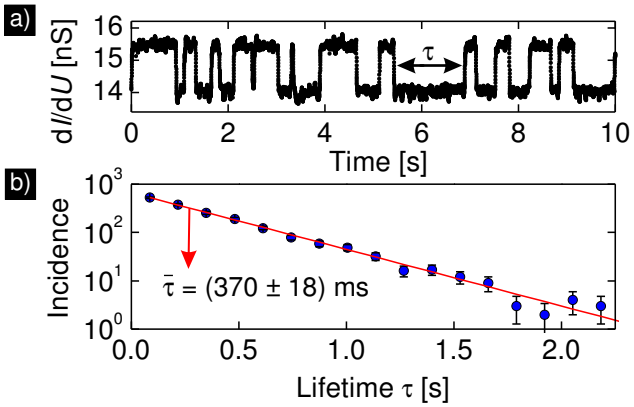

Figure 7.10: Lifetime analysis of an individual nanomagnet. (**a**) Trace section of the magnetic $\mathrm{d}I/\mathrm{d}U$ signal. (**b**) Respective histogram of lifetimes τ. Fitting with a decay law results in the mean lifetime $\bar{\tau}$. $T = 49.3\,\mathrm{K}$, $U = 220\,\mathrm{mV}$, $I = 2\,\mathrm{nA}$, Cr/W-tip.

$\Delta T(4.6\,\mathrm{V}) = (0.9 \pm 0.1)\,\mathrm{K}$. Hence, the effective heating of approximately 1 K calculated by Eq. 7.8 is consistent with the experimental finding that increasing the sample bias to 4.6 V results in the same mean lifetime as increasing the substrate temperature by $\Delta T = 1\,\mathrm{K}$. Consequently, the modified Néel-Brown law describes the experimental observations correctly.

Emission current dependent magnetic switching behavior

To get a more detailed understanding of the interaction of spin-polarized field emission currents with magnets, a current-dependent lifetime analysis has been performed. The switching behavior of an individual iron nanomagnet has been recorded at different emission currents between 2 and 140 nA. Increasing the current is realized by further approaching the tip to the sample. To compensate for the resulting Stark shift, the bias voltage was slightly adjusted for maximum magnetic contrast on the edge of the first FER peak at every current setpoint. Trace sections of the magnetic telegraph noise using SP-SFEM at an emission current of $I = 2\,\mathrm{nA}$, $I = 80\,\mathrm{nA}$ and $I = 140\,\mathrm{nA}$ are shown in Fig. 7.11. At low emission current $I = 2\,\mathrm{nA}$ the nanomagnet switches only two times within 20 s, as shown in the top panel of Fig. 7.11. Roughly estimated, this corresponds to a mean lifetime of the order of about 10 s. Increasing the emission current to $I = 80\,\mathrm{nA}$, the nanomagnet has a mean lifetime of about 0.5 s. Finally, at an emission current of $I = 140\,\mathrm{nA}$ the magnet has a mean lifetime of only about 25 ms. The results of the lifetime analysis for every current setpoint I are shown in Fig. 7.12(a). Increasing the emission current from $I = 2\,\mathrm{nA}$ to 140 nA results in a drastic decrease of the mean lifetime by three orders of magnitude. This indicates a considerable effective temperature increase of the nanomagnet. Generally, passing a current I at constant bias U through a conductor generates a temper-

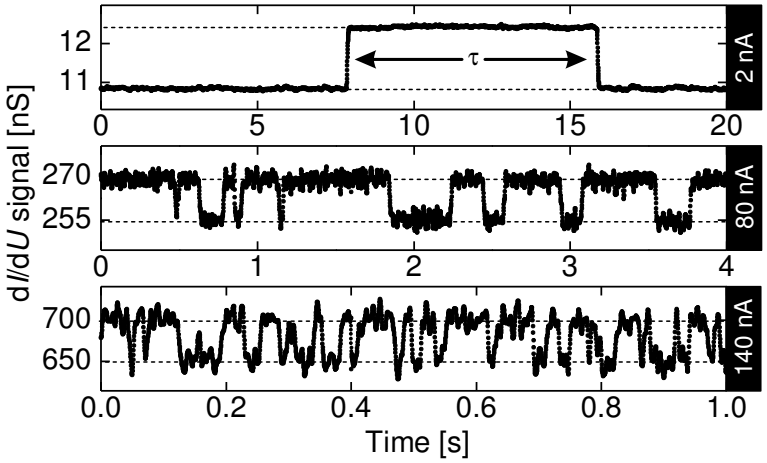

Figure 7.11: Magnetic switching behavior at different emission currents recorded by SP-SFEM. Trace section of the magnetic telegraph noise at emission current $I = 2\,\mathrm{nA}$, $I = 80\,\mathrm{nA}$ and $I = 140\,\mathrm{nA}$ (from top to bottom). $U = 4.9$, 5.0, 5.1 V, $T = 35.4\,\mathrm{K}$, bulk Cr-tip.

ature increase proportional to the power $P = U \cdot I$. This phenomenon is known as *Joule heating*. Here, as the effective temperature increase of the nanomagnet is caused by passing a field emission current through the nanomagnet, a Joule heating generated by field-emitted electrons is observed.

In order to compare the effects of field-emitted electrons with those of low-energy tunneling electrons, an additional lifetime analysis has been performed by SP-STM with the same probe tip on the same nanomagnet. The results for several tunnel current setpoints between $I = 2$ and $1000\,\mathrm{nA}$ are shown in the top panel of Fig. 7.12(b). Whereas in SP-SFEM the mean lifetime decreases considerably by three orders of magnitude when increasing the emission current to $I = 140\,\mathrm{nA}$, in SP-STM increasing the tunnel current up to $1000\,\mathrm{nA}$ only results in a lifetime reduction of two orders of magnitude. This finding indicates a stronger Joule heating generated by field-emitted electrons than by tunneling electrons.

Equation 7.8 allows for the determination of the effective temperature increase $\Delta T(U, I)$ of the nanomagnet due to Joule heating, where $\bar{\tau}_\mathrm{i}$ is in this case the mean lifetime determined at $U = 200\,\mathrm{mV}$ and $I = 10\,\mathrm{nA}$. The effective energy barrier has been determined by the mean lifetimes at two different temperatures according to Eq. 5.1, resulting in $E_\mathrm{b} = (128 \pm 5)\,\mathrm{meV}$. The results for the effective temperature increase $\Delta T(I)$ generated by tunneling electrons at $U = 200\,\mathrm{mV}$ are plotted in the lower panel of Fig. 7.12(b). The temperature rises linearly as a function of the tunnel current I. This is consistent with previous SP-STM experiments on the same sample system as well as an experimental STM study of heat generation between an STM tip and a metallic sample, both demonstrating that the Joule heat dissipated in the sample scales linearly with I at constant low bias voltage [222, 223]. Fitting the data with $\Delta T(I) = c_\mathrm{JH} I$ yields $c_\mathrm{JH} =$

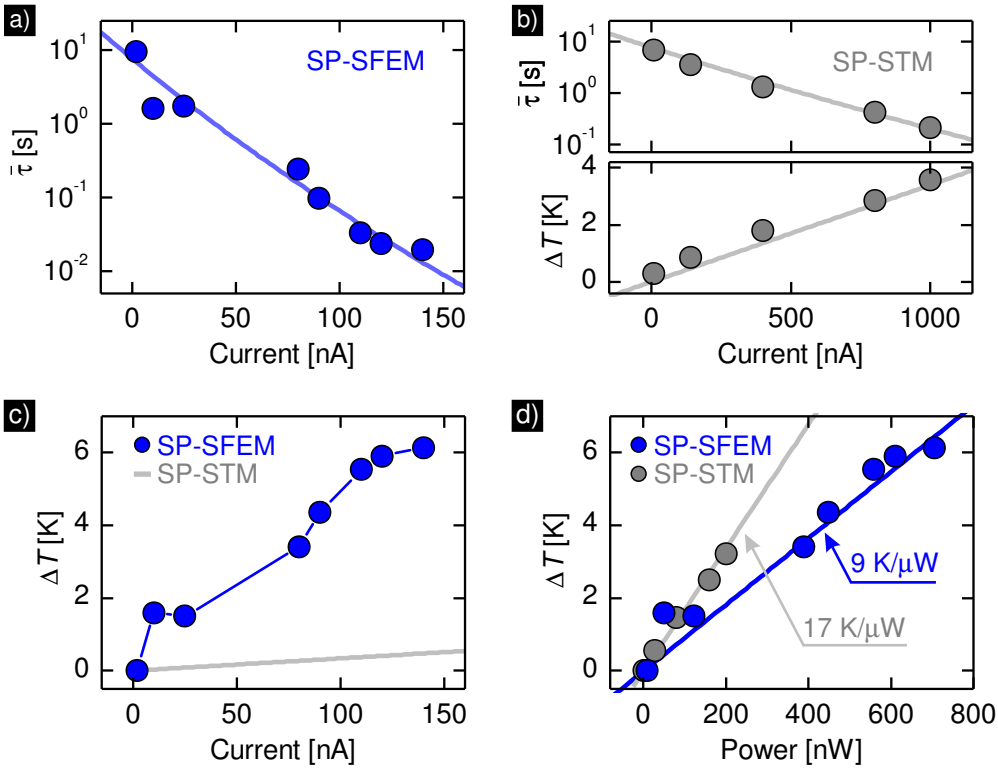

Figure 7.12: Joule heating generated by field-emitted and tunneling electrons. (**a**) Mean lifetime $\bar{\tau}$ as a function of emission current I. The blue line is a guide to the eye. (**b**) Mean lifetime $\bar{\tau}$ (upper panel) and temperature increase ΔT (lower panel) of the nanomagnet as a function of tunnel current I. The grey line in the upper panel is a guide to the eye and indicates a linear fit in the lower panel. (**c**) ΔT as a function of emission current. For comparison, $\Delta T(I)$ of (b) generated by tunneling electrons is indicated by the grey line. (**d**) ΔT as a function of power. Fitting yields the respective differential temperature increase dT/dP. The error bars are within data points. $U = 4.9, ..., 5.1\,\mathrm{V}$ (SP-SFEM), $U = 200\,\mathrm{mV}$ (SP-STM), $T = 35.4\,\mathrm{K}$, bulk Cr-tip.

$(3.4 \pm 0.1)\,\mathrm{K}/\mu\mathrm{A}$, where c_{JH} is introduced as the differential heating coefficient of the magnetic tunnel junction.

In Fig. 7.12(c), the temperature increase $\Delta T(I)$ generated by spin-polarized field-emitted electrons is shown. The data are deduced from the mean lifetimes shown in Fig. 7.12(a) according to Eq. 7.8. For comparison, the results of the SP-STM analysis of Fig. 7.12(b) using low-energy tunneling electrons at $U = 200\,\mathrm{mV}$ with the same tip on the same nanomagnet are indicated by the grey line.

The temperature of the nanomagnet increases by 6 K for a field emission current of $I = 140\,\mathrm{nA}$. This is a factor of ten higher than for tunneling electrons. Hence, the Joule heating as a function of current is considerably higher for field emission than for tunneling.

Generally, Joule heating is expected to depend on the power. In SP-SFEM at the same current setpoint owing to the increased sample bias more power is passed through the nanomagnet than in SP-STM. In order to compare the Joule heating generated by field-emitted and tunneling electrons, the effective temperature increase ΔT has to be considered in terms of the total power injection $P = UI$, as shown in Fig. 7.12(d). Surprisingly, for the same power P a different effective temperature increase is observed for field-emitted and for tunneling electrons. Naively, one would expect the Joule heating to be the same for the same power. Fitting the data in Fig. 7.12(d) with $\Delta T(P) = (\mathrm{d}T/\mathrm{d}P) \cdot P$ yields a differential temperature increase $\mathrm{d}T/\mathrm{d}P$ of $(9 \pm 1)\,\mathrm{K}/\mu\mathrm{W}$ for SP-SFEM and $(17 \pm 1)\,\mathrm{K}/\mu\mathrm{W}$ for SP-STM. Consequently, $\mathrm{d}T/\mathrm{d}P$ generated by field-emitted electrons is about a factor of two smaller than for tunneling electrons. So it matters if field-emitted or tunneling electrons pass through the nanomagnet. As the main difference between the field-emitted and the tunneling electrons is the electron energy eU, this finding indicates that the effective temperature increase of the nanomagnet depends not only on the power but also on the electron energy.

The different electron energies result in different energy relaxation processes resulting in different effective temperature increases of the nanomagnet. Consider the physical picture sketched schematically in Fig. 7.13. In SP-STM, electrons with small energies above the Fermi level $E_{\mathrm{F,s}}$ of the sample tunnel directly into the nanoisland, thereby predominantly generating phonons inside the nanoisland [224, 225], as depicted in Fig. 7.13(a). As the Fe nanoisland is thermally coupled to the W substrate serving as infinite heat bath, one might naively expect that there is no noticeable heating of the island. However, owing to the thermal resistance of the Fe-W-interface [226, 227], a very local heat dissipation within the Fe nanoisland is expected, with the temperature of the W substrate remaining unaffected.

In SP-SFEM, a two-step process is expected for field-emitted electrons, that are first injected into the FER state and subsequently relax inelastically to the Fermi level of the sample, as depicted in Fig. 7.13(b). Here, photon emission takes place [228, 229] removing energy from the surface. Hence, the electron energy released by photon emission cannot be transferred into heat any more. But the quantum yield is expected to be only about 10^{-3} [228] to 10^{-4} [230], meaning that only every thousandth or ten thousandth electron releases its energy by photon emission. Hence, this relaxation mechanism cannot explain the smaller differential temperature increase $\mathrm{d}T/\mathrm{d}P$ of the nanomagnet in SP-SFEM on its own. The dominating relaxation mechanism is given by electron-electron interactions, whereas electron-phonon coupling is weak [111, 231, 232]. As a consequence, phonons are not directly excited by the field-emitted electrons but are excited collaterally in electron-electron interaction processes, leading to hot electrons that finally thermalize.

In contrast to SP-STM, where electrons can only tunnel into the nanoisland via overlapping wavefunctions from the tip and the sample (cf. Chap. 2), the

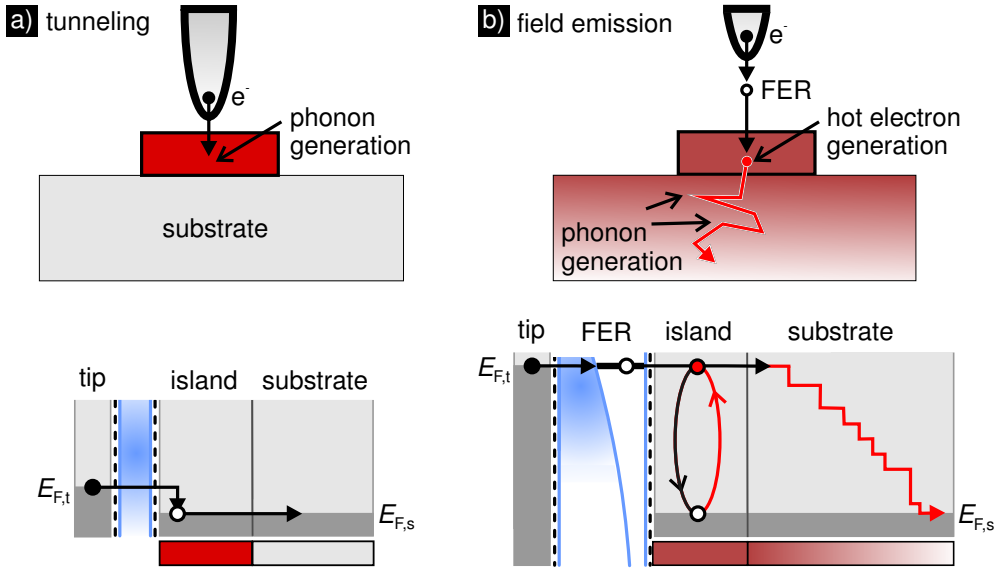

Figure 7.13: Energy dissipation in the island and the substrate due to tunneling and field-emitted electrons. (**a**) In SP-STM, electrons tunnel directly into the island, thereby generating phonons. The substrate remains unaffected. (**b**) In SP-SFEM, electrons are injected into the FER state and subsequently relax to $E_{F,s}$, thereby predominantly exciting hot electrons. The latter need a long thermalization path to relax to $E_{F,s}$. $E_{F,t}$, $E_{F,s}$: Fermi level of the tip and the sample.

field-emitted electrons in SP-SFEM are free electrons in that they have a positive kinetic energy in front of the surface and are accelerated towards the surface. When penetrating the surface without former energy relaxation, the electron is expected to have an inelastic mean free path of $\approx 6\,\text{Å}$ [233], which is three times larger than the vertical dimensions of the monolayer thick Fe/W(110) nanomagnet. Hence, some of the field-emitted electrons pass ballistically through the nanomagnet and relax afterwards in the substrate. This process does not affect the nanomagnet. However, some of the field-emitted electrons may relax within the nanoisland, thereby predominantly exciting hot electrons [111, 234, 235]. The latter will thermalize finally. But as they need a long thermalization path to relax to the Fermi level of the sample, this thermalization takes place in the substrate rather than in the nanomagnet. As a consequence, the overall phonon generation *within* the nanomagnet is weaker in SP-SFEM than in SP-STM.

Phonon excitation probability

The Joule heating generated at different sample temperatures has been investigated, as shown in Fig. 7.14. The mean lifetime $\bar{\tau}$ of the nanomagnet has been determined as a function of power using field-emitted and tunneling electrons at $T = 35.4\,\text{K}$. The decrease of the mean lifetime as a function of power is larger for SP-STM than for SP-SFEM, as indicated in Fig. 7.14(a). The corresponding

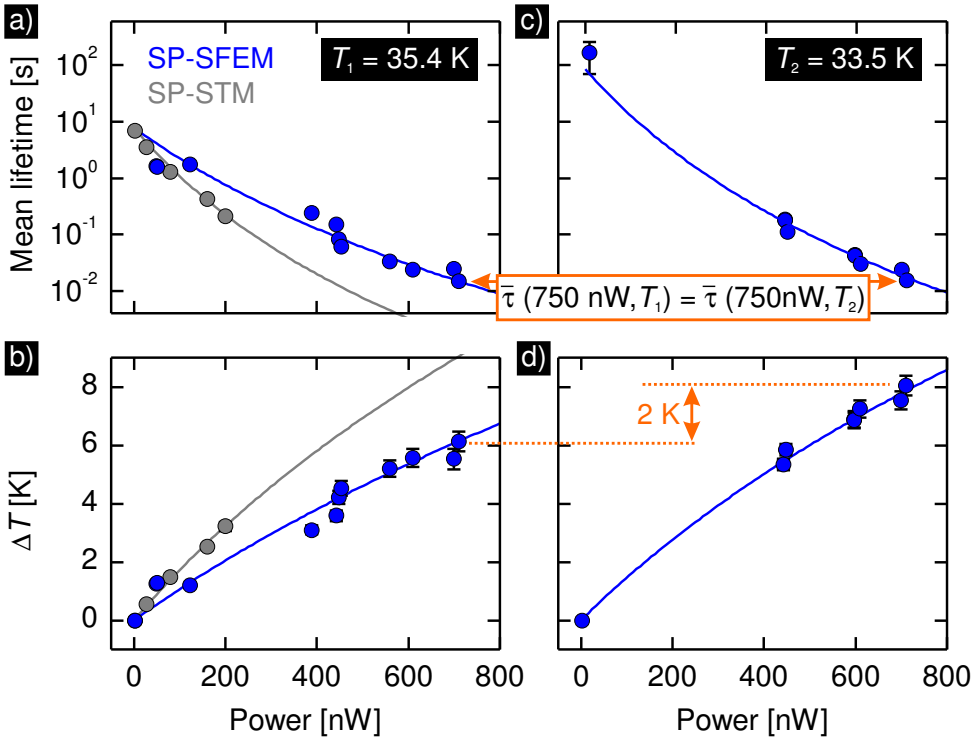

Figure 7.14: Joule heating generated at different temperatures. (**a**) Mean lifetime as a function of power and (**b**) corresponding Joule heating $\Delta T(P)$ when injecting field-emitted (blue) or tunneling (grey) electrons at $T_1 = 35.4\,\mathrm{K}$. (**c**) Mean lifetime as a function of power and (**d**) corresponding Joule heating $\Delta T(P)$ when injecting field-emitted electrons at $T_2 = 33.5\,\mathrm{K}$. The lines in (a) and (c) are guides to the eye. At $P = 750\,\mathrm{nW}$ the mean lifetime is the same for both temperatures, and $\Delta T(P = 750\,\mathrm{nW})$ is 2 K higher for T_2 than for T_1 (marked by arrows). The data are well described by a simple model of temperature-dependent thermal boundary resistance and different phonon excitation probabilities for field-emitted (blue line) and tunneling electrons (grey line). $U = 200\,\mathrm{mV}$ (SP-STM), $U = 4.9, ..., 5.1\,\mathrm{V}$ (SP-SFEM), bulk Cr-tip.

effective temperature increase $\Delta T(P)$ as a function of power P has been evaluated using Eq. 7.8, as shown in Fig. 7.14(b). For the same power, a different effective temperature increase is observed for field-emitted and for tunneling electrons.

Figure 7.14(c) shows the mean lifetime for the same nanomagnet as a function of power for field-emitted electrons at a sample temperature of $T = 33.5\,\mathrm{K}$. The intrinsic lifetime of the nanomagnet is one order of magnitude longer at $T = 33.5\,\mathrm{K}$ than at $T = 35.4\,\mathrm{K}$. This is expected from the Arrhenius-like behavior of the mean lifetime as a function of temperature (cf. Eq. 5.1) [190]. Surprisingly, the mean lifetime of the nanomagnet at $P = 750\,\mathrm{nW}$ is the same for both temperatures, $\bar{\tau}(35.4\,\mathrm{K}) = \bar{\tau}(33.5\,\mathrm{K})$. From the higher intrinsic mean lifetime at $T = 33.5\,\mathrm{K}$ and making the assumption that the Joule heating is independent on the sample

temperature, one would expect the mean lifetime at $P = 750\,\mathrm{nW}$ to be larger at $T = 33.5\,\mathrm{K}$ than at $T = 35.4\,\mathrm{K}$.

The corresponding effective temperature increase $\Delta T(P)$ as a function of power P for $T = 33.5\,\mathrm{K}$ is shown in Fig. 7.14(d). Whereas the effective temperature increase for $P = 750\,\mathrm{nW}$ at $T = 33.5\,\mathrm{K}$ is $8\,\mathrm{K}$, it is $6\,\mathrm{K}$ at $35.4\,\mathrm{K}$ (cf. Fig. 7.14(b)). Hence, $\Delta T(P = 750\,\mathrm{nW})$ is $2\,\mathrm{K}$ higher for the lower temperature. The previous facts suggest that the Joule heating depends on the sample temperature.

Local heating of the nanoisland is due to phonon generation by inelastically scattered electrons. The phonons responsible for the heat transport are scattered at the interface between the iron and the tungsten, resulting in a temperature difference ΔT. The heat flow across the interface between two semi-infinite solids is given by [226]

$$\alpha_{\mathrm{ph}} P = \frac{2\pi^5 k_{\mathrm{B}}^4}{15h^3} A \left(\frac{\Gamma_l}{c_l^2} + \frac{2\Gamma_t}{c_t^2} \right) \left(T_{\mathrm{island}}^4 - T^4 \right), \tag{7.9}$$

where α_{ph} is the probability of phonon excitation by a tunneling or field-emitted electron, $P = UI$ is the power, h is Planck's constant, A is the interface area of the nanoisland, Γ_l and Γ_t are the transmission probabilities of longitudinal and transverse phonon modes, c_l and c_t are their sound velocities, $T_{\mathrm{island}} = \Delta T + T$ is the temperature of the nanoisland and T the substrate temperature. Generally, the transmission probabilities are complicated integral functions of the phonon densities and sound velocities of the two media. Since Fe/W(110) nanoislands grow pseudomorphically [174], as a first approximation, both sides of the interface are taken to be identical. A perfect match at the interface would give $\Gamma_l = \Gamma_t = 0.5$ [226, 227]. Given the sound velocities of tungsten $c_l = 5.2 \times 10^3\,\mathrm{m/s}$ and $c_t = 2.9 \times 10^3\,\mathrm{m/s}$ [227], the temperature difference between the substrate and a nanoisland with a base area of $A = (6 \pm 1)\,\mathrm{nm}^2$ is

$$\Delta T(P) = \sqrt[4]{(2.83 \cdot 10^{14}\,\mathrm{K^4/W})\alpha_{\mathrm{ph}} P + T^4} - T. \tag{7.10}$$

Fitting Eq. 7.10 to the Joule heating $\Delta T(P)$ at $T = 35.4\,\mathrm{K}$ generated by field-emitted and tunneling electrons yields a phonon excitation probability for field-emitted electrons $\alpha_{\mathrm{FEM}} = (0.7 \pm 0.1)\,\%$ and for tunneling electrons $\alpha_{\mathrm{Tunnel}} = (1.2 \pm 0.2)\,\%$. α_{FEM} is consistent with an electron-phonon coupling of the first image-potential state with values ranging from $0.2\,\%$ to $1\,\%$ [110, 111, 232]. Compared to other studies with α_{Tunnel} ranging between $1\,\%$ and $10\,\%$ [236, 237], my result for α_{Tunnel} is reasonable, demonstrating that the simple model describes the physics of the experiment.

The relatively low phonon excitation probability for both field-emitted and tunneling electrons means that most of the electrons pass through the nanoisland without exciting any lattice vibrations, and the electron energy is mainly

deposited in the substrate. However, since it serves as an infinite heat bath the temperature of the substrate remains unchanged. Although being low in both cases, the phonon excitation probability for field-emitted electrons is lower than for tunneling electrons. As a result, the temperature increase of the nanoisland for the same power P for field-emitted and tunneling electrons differ, in agreement with the model of different relaxation mechanisms described above.

Fitting Eq. 7.10 to the Joule heating $\Delta T(P)$ at $T = 33.5\,\mathrm{K}$ generated by field-emitted electrons yields a phonon excitation probability $\alpha_{\mathrm{FEM}} = (0.8 \pm 0.1)\,\%$. At both temperatures phonon excitation probabilities are nearly identical. This is consistent with the general expectation that the phonon excitation probability does not depend strongly on the temperature [227]. In simple words, as phonons are bosonic quasiparticles, their creation is independent of the presence of other phonons. Consequently, the observed dependence of the Joule heating on temperature arises primarily from the temperature dependence of the heat flow across the interface between the nanoisland and the substrate.

7.3.2 Spin-transfer torque generated by field-emitted electrons

Recent SP-STM experiments have demonstrated spin-transfer torque effects induced by spin-polarized tunnel currents [194, 222]. When passing a *spin-polarized* field emission current through a magnet, the spin magnetic moment of the field-emitted electrons is expected to exert a torque on the sample magnetization. The question arises, whether spin-transfer torque effects can be detected in SP-SFEM and how the spin magnetic moment of field-emitted electrons interacts with atomic-scale magnets.

The magnetic telegraph noise recorded at different spin-polarized field emission currents between 2 and 140 nA has been analyzed in terms of the lifetimes of the two magnetic orientations of the nanomagnet with respect to the tip magnetization. All the lifetimes between two consecutive switching events were determined. Unlike in Sec. 7.3.1, the lifetimes for the two magnetic states, τ_0 and τ_1, have been evaluated separately resulting in a state-resolved lifetime histogram of the nanomagnet, as shown in the upper and middle panel of Fig. 7.15(a) for a low emission current of $I = 10\,\mathrm{nA}$. By definition, state 0 is related to a low $\mathrm{d}I/\mathrm{d}U$ signal, and state 1 is related to a high $\mathrm{d}I/\mathrm{d}U$ signal in the telegraph noise. Fitting an exponential decay law yields the mean lifetimes $\bar{\tau}_0$ for state 0 and $\bar{\tau}_1$ for state 1. At low emission both lifetimes $\bar{\tau}_0$ and $\bar{\tau}_1$ are virtually equal since both states are energetically degenerate and should be populated equally. The state-resolved lifetime histogram for a high emission current of $I = 140\,\mathrm{nA}$ is shown in the lower panel of Fig. 7.15(a). In contrast to the low emission regime, both lifetimes are reduced due to Joule heating (cf. Sec. 7.3.1). In addition, an imbalance of the mean lifetimes $\bar{\tau}_0$ and $\bar{\tau}_1$ is observed at high emission with state 1 having a longer

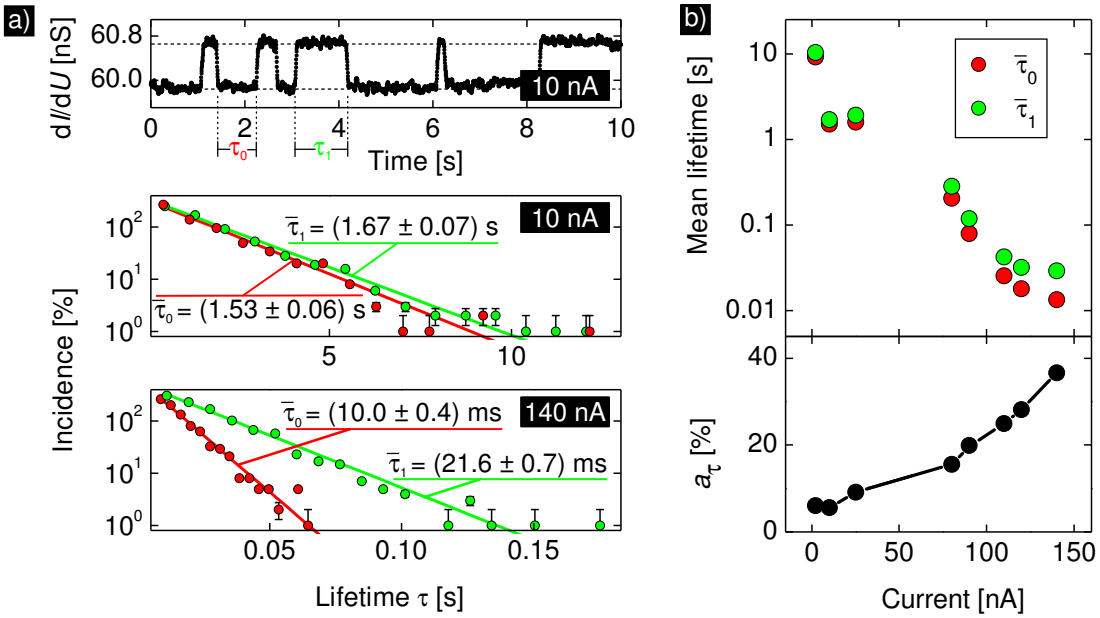

Figure 7.15: State-resolved lifetimes of a nanomagnet affected by spin-polarized field-emitted electrons. (**a**) Trace section of the magnetic dI/dU signal at an emission current $I = 10\,\mathrm{nA}$ (upper panel). Histograms of the lifetimes τ_0 and τ_1 of state 0 and 1 measured at $I = 10\,\mathrm{nA}$ (lower panel) and $I = 140\,\mathrm{nA}$ (bottom panel), and decay law fit (lines) yields the respective mean lifetime $\bar{\tau}_{0,1}$. (**b**) Mean lifetimes $\bar{\tau}_0$ and $\bar{\tau}_1$ as a function of emission current (top panel) and lifetime asymmetry (bottom panel). (Error bars are within the data points.) $U = 4.9, ..., 5.1\,\mathrm{V}$, $T = 35.4\,\mathrm{K}$, bulk Cr-tip.

lifetime than state 0. Consequently, the mean lifetime at high emission currents is found to depend strongly on the relative magnetization directions of the tip and the sample.

The results of the state-resolved lifetime analysis for each current setpoint I are shown in the top panel of Fig. 7.15(b). The mean lifetimes drop by about three orders of magnitude when increasing the emission current I from 2 to 140 nA due to Joule heating, as discussed in Sec. 7.3.1.

A trend from equal lifetimes at low emission current to a lifetime splitting at high emission current is observed in the top panel of Fig. 7.15(b). This becomes more obvious when plotting the lifetime asymmetry $a_\tau(I) = \frac{\bar{\tau}_1(I) - \bar{\tau}_0(I)}{\bar{\tau}_1(I) + \bar{\tau}_0(I)}$, as can be seen in the bottom panel of Fig. 7.15(b). a_τ increases with I, and values of up to 40 % for $I = 140\,\mathrm{nA}$ are obtained. The spin-polarized field-emitted electrons force the nanomagnet to favor one of the degenerate magnetic states at the expense of the other. It indicates a directed switching of the nanomagnet. This purely magnetic feature is direct experimental demonstration of spin-transfer torque generated by field emission currents.

To illustrate the influence of Joule heating and spin-transfer torque on the switching behavior of a nanomagnet within the macrospin model, a schematic of the energy landscape of a magnet with uniaxial anisotropy under the influence of a low and a high spin-polarized emission current is depicted in Fig. 7.16. Due to thermal excitation at temperature T the magnetization may overcome the effective activation barrier E_b between the two states 0 and 1, as shown in Fig. 7.16(a). At high emission current, one magnetic state is favored at the cost of the other. This can be explained by different effective energy barriers from state 0 to state 1 and vice versa, as depicted in Fig. 7.16(b). Passing a high spin-polarized emission current through the magnet, the spin-transfer torque modifies the effective energy barrier E_b by $\pm\Delta E$, thereby removing the state degeneracy and favoring switching from state 0 to state 1, as shown in Fig. 7.15.

For comparison with the spin-transfer torque of spin-polarized low-energy tunneling electrons, a lifetime analysis as a function of tunnel current has been performed with SP-STM using the same probe tip on the same nanomagnet. The magnetic telegraph noise recorded at a fixed bias of $U = 200\,\mathrm{mV}$ and several tunnel current setpoints between $I = 10$ and $1000\,\mathrm{nA}$ has been analyzed with respect to the lifetimes of the two magnetic states of the nanomagnet. The results of the state-resolved lifetime analysis are shown in Fig. 7.17. As can be seen in Fig. 7.17(a), both the lifetimes of state 1 and 0 decrease with increasing I, and simultaneously a lifetime asymmetry evolves, favoring state 1. As discussed in the case of SP-SFEM, the reduced lifetime is attributed to Joule heating, and the evolving lifetime asymmetry is caused by the spin-transfer torque of the spin-polarized tunnel current [194].

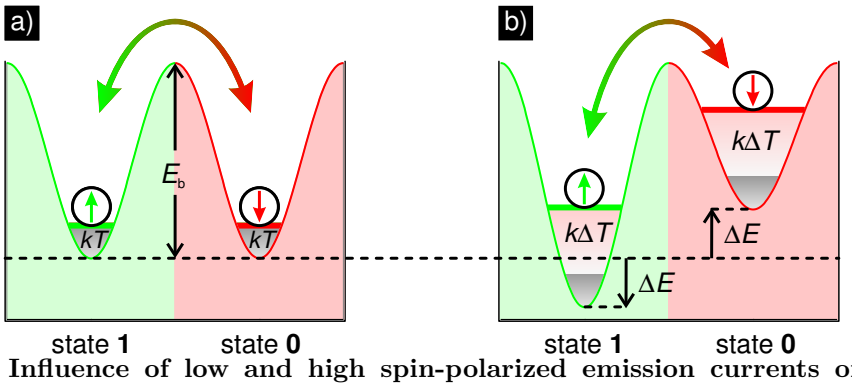

Figure 7.16: Influence of low and high spin-polarized emission currents on the energy landscape of a magnet with uniaxial anisotropy. (**a**) At low emission current, the intrinsic switching behavior of the magnet remains unaffected. Because of thermal agitation at temperature T, the magnetization may overcome the effective activation barrier E_b between the two states 1 and 0. (**b**) Influence of a high spin-polarized emission current: Joule heating effectively increases T by ΔT, and the spin-torque modifies E_b by ΔE, thereby removing the state degeneracy and favoring switching from state 1 to state 0.

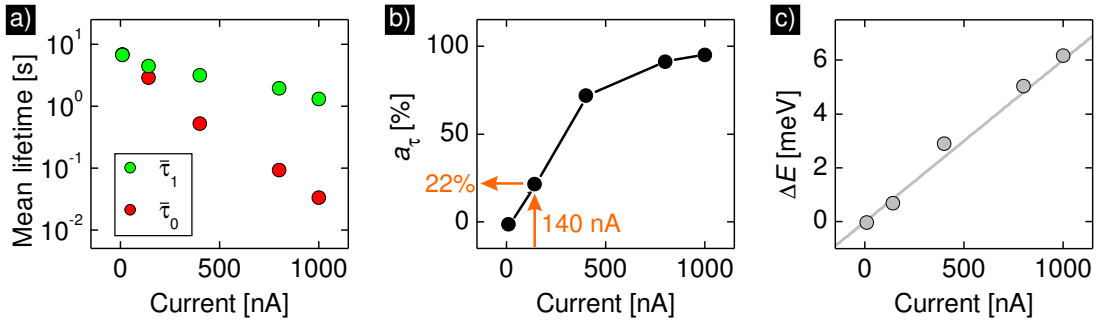

Figure 7.17: Current-dependent magnetic switching behavior in SP-STM using spin-polarized tunneling electrons. (**a**) State-resolved mean lifetimes $\bar{\tau}_0$ and $\bar{\tau}_1$ as a function of tunnel current I. (**b**) Lifetime asymmetry a_τ. (**c**) Spin-transfer torque modification $\Delta E(I)$ of the effective activation energy barrier E_b. (Error bars are within data points). Grey line indicates a linear fit. $U = 200\,\mathrm{mV}$, $T = 35.4\,\mathrm{K}$, bulk Cr-tip.

In Fig. 7.17(b), the lifetime asymmetry $a_\tau(I)$ is plotted, indicating an asymmetry of almost 100% at $I = 1000\,\mathrm{nA}$. At this tunnel current the mean lifetime of state 0 is almost two orders of magnitude lower than the lifetime of state 1, as shown in Fig. 7.17(a). After switching to state 0, the nanomagnet is forced immediately to switch back to state 1. Hence, at $I = 1000\,\mathrm{nA}$ the nanomagnet is forced to remain in the magnetic state 1. The magnitude of the spin-transfer torque generated in SP-STM is expected to scale with the tunnel current [222, 238]. Each electron carries a spin magnetic moment. When it flips its spin, it exerts a torque on the nanomagnet. Consequently, the spin-transfer torque is exerted per electron and its magnitude is expected to scale with the current. Hence, the more electrons per second pass through the magnet, the greater the spin-transfer torque and thus the lifetime asymmetry. The high asymmetry of almost 100% at $I = 1000\,\mathrm{nA}$ in Fig. 7.17(b) can be attributed to the high current.

As discussed in Sec. 7.3.1, the considerable Joule heating in SP-SFEM results in very short mean lifetimes of about 10 ms at moderate emission currents. The emission current could not be increased above $I = 140\,\mathrm{nA}$ in this experiment as this particular nanomagnet then switches too fast to be analyzed. However, at the same current $I = 140\,\mathrm{nA}$, the lifetime asymmetry in SP-SFEM is almost 40 % (cf. Fig. 7.15(b)), whereas it is only 22 % in SP-STM. This finding suggests a stronger spin-transfer torque effect in SP-SFEM.

To account for the spin-transfer torque effect, the Néel-Brown law (Eq. 5.1 and Eq. 7.7) is expanded further. The mean lifetime $\bar{\tau}_0(U, I)$ and $\bar{\tau}_1(U, I)$ arising from a spin-polarized current I at sample bias U can be described by

$$\bar{\tau}_{0/1}(U, I) = \nu_0^{-1} \exp\left(\frac{E_\mathrm{b} \mp \Delta E(U, I)}{k_\mathrm{B}(T + \Delta T(U, I))}\right). \tag{7.11}$$

The temperature T of the nanomagnet is increased by $\Delta T(U, I)$ due to Joule heating and the spin-transfer torque modifies E_b by $\mp\Delta E(U, I)$, depending on the

relative orientation of the magnetization of the tip and the sample. Equation 7.11 can be used to determine the energy splitting $\Delta E(U, I)$ of the effective activation energy barrier E_b due to the spin-transfer torque:

$$\Delta E(U, I) = \frac{k_\mathrm{B}\left[T + \Delta T(U, I)\right]}{2} \ln \frac{\bar{\tau}_0(U, I)}{\bar{\tau}_1(U, I)}. \tag{7.12}$$

Here, $\Delta T(U, I)$ is the Joule heating as determined previously (see Fig. 7.12). The results for the spin-transfer torque modification $\Delta E(I)$ generated by tunneling electrons are plotted in Fig. 7.17(c). A linear dependence on the tunnel current I is observed. This finding is in accordance with theoretical studies on the thermally-assisted magnetization reversal in the presence of a spin-transfer torque within the macrospin model [238] and previous SP-STM experiments on the same sample system [222]. Fitting the data with $\Delta E = c_\mathrm{ST} I$ results in $c_\mathrm{ST} = (6.3 \pm 0.2)\,\mathrm{meV}/\mu\mathrm{A}$, with c_ST being introduced as the differential modification of the effective activation energy barrier E_b.

The spin-transfer torque contribution $\Delta E(I)$ generated by spin-polarized field-emitted electrons is shown in Fig. 7.18(a). The data were derived from the mean lifetimes $\bar{\tau}_0$ and $\bar{\tau}_1$ in Fig. 7.15 using Eq. 7.12. For comparison, the results of the SP-STM analysis using low-energy tunneling electrons with the same tip on the same nanomagnet are indicated by the grey line. At currents $I < 80\,\mathrm{nA}$, the spin-transfer torque contribution $\Delta E(I)$ generated by spin-polarized field-emitted electrons is similar to that of spin-polarized tunneling electrons. However, at higher currents ΔE is increased for field-emitted electrons. This is unexpected, since each electron can only flip its spin magnetic moment *once* when exerting a torque on the nanomagnet. However, the spin-flip process *itself* may differ for low-energy tunneling electrons and higher energy field-emitted electrons, leading to different efficiencies in forcing the nanomagnet to reverse its magnetization.

The microscopic processes of spin-transfer torque in SP-SFEM and SP-STM have to be considered. In a simple model, assuming a spin polarization of unity, the electron has to flip its spin in order to get into the sample when the tip and the sample are in an antiparallel magnetic configuration. As depicted in Fig. 7.18(b), in SP-STM spin-polarized low-energy electrons tunnel directly from occupied states of the tip into unoccupied states close to E_F in the sample. Here, the spin-flip is achieved predominantly by creating magnons [239].

In contrast to the direct tunneling in SP-STM, in SP-SFEM a two-step process can take place. Spin-polarized electrons are first injected into the exchange-split FER state and subsequently relax into the sample. During the interaction with the sample two different spin-flip processes may occur. The field-emitted electron may flip its spin either (i) by relaxing within the FER spin states, thereby generating low-energy magnons inside the magnet [16]; or (ii) when relaxing from the FER state into the sample, resulting in Stoner excitation [240]. The two spin-flip processes are shown schematically in Fig. 7.18(c).

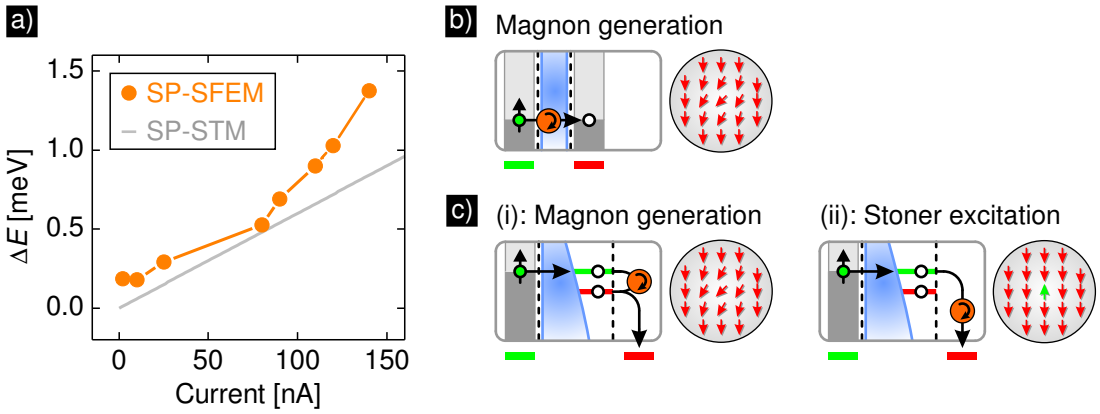

Figure 7.18: Spin-transfer torque generated by spin-polarized electrons. (**a**) Modification $\Delta E(I)$ of E_b. (Error bars are within the data points). For comparison, the SP-STM results are indicated by the grey line. $U = 4.9, ..., 5.1\,\mathrm{V}$, $T = 35.4\,\mathrm{K}$, bulk Cr-tip. (**b**) Spin-flip of electrons in SP-STM while tunneling from the tip into the sample, thereby generating magnons. (**c**) Spin-flip of field-emitted electrons in SP-SFEM: (i) within the FER spin states, generating magnons; (ii) when relaxing from the FER spin state into the sample, resulting in Stoner excitations.

Both processes destabilize the sample magnetization and ultimately trigger magnetization reversal, resulting in a directed switching accompanied by a lifetime asymmetry. However, magnons are spin waves, where all of the spin magnetic moments of the nanomagnet precess only slightly, as depicted in Fig. 7.18(c). They also carry very little energy ($\sim$ meV) for the destabilization of the nanomagnet's orientation [241, 242]. In contrast, Stoner excitations are higher energy single-site spin flips. A single excitation can reverse individual spin magnetic moments of the nanomagnet, as indicated in Fig. 7.18(c), transfering a tremendous amount of energy ($\sim$ eV) to the spin system. [12, 243] Consequently, flipping the spin by generating Stoner excitations destabilizes the nanomagnet's magnetization more efficiently than magnon generation.

As shown in Fig. 7.18(a), a higher efficiency of the spin-transfer torque per electron is observed at higher emission currents. I suppose, that the contributions from the two possible spin-flip processes (i) and (ii) in SP-SFEM change with the emission current. Increasing the emission current I is achieved by reducing the distance between the tip and the sample. This increases the electric field in the junction. It is known, that an increased electric field pushes the FER states towards the surface, thereby leading to an enhanced coupling of the FER to the magnet [22]. Consequently, process (ii) is expected to become more and more dominant with increasing emission current. Hence, with increasing emission current more and more Stoner excitations are generated at the cost of magnon generation. Since they have a much higher switching efficiency than magnons,

these Stoner excitations may give rise to the observed increase in the spin-transfer torque switching efficiency at high emission current I.

7.4 Switching quasistable iron nanomagnets

The previous section has demonstrated that spin-polarized field-emitted electrons strongly impact thermally switching nanomagnets. This raises the question whether thermally-stable nanomagnets can be influenced by spin-polarized field-emitted electrons.

An experimental demonstration would be the magnetization reversal of an otherwise thermally-stable nanomagnet triggered by SP-SFEM. The basic idea is sketched in Fig. 7.19. Initially, the nanomagnet is in the magnetic state 1, as depicted in Fig. 7.19(a). Thermal switching between the two magnetic states is hindered because the thermal energy $k_{\mathrm{B}}T$ is much smaller than the effective energy barrier E_{b}. When applying a high field emission current in SP-SFEM, the temperature rise ΔT produced by Joule heating decreases the lifetime of the magnetic state, as indicated in Fig. 7.19(b). In addition, the spin-transfer torque generated by the field-emitted electrons removes the degeneracy of the two magnetic states, and E_{b} is further decreased by ΔE for state 1, thereby favoring a magnetization reversal. Once the magnetization has been reversed, the increased effective energy barrier caused by the spin-transfer torque for state 0 inhibits switching back. Fig. 7.19(c) shows the situation after SP-SFEM induced switching. The nanomagnet is in the magnetic state 0 and the high effective energy barrier again stabilizes the magnetization of the nanoisland against thermally-driven reversal.

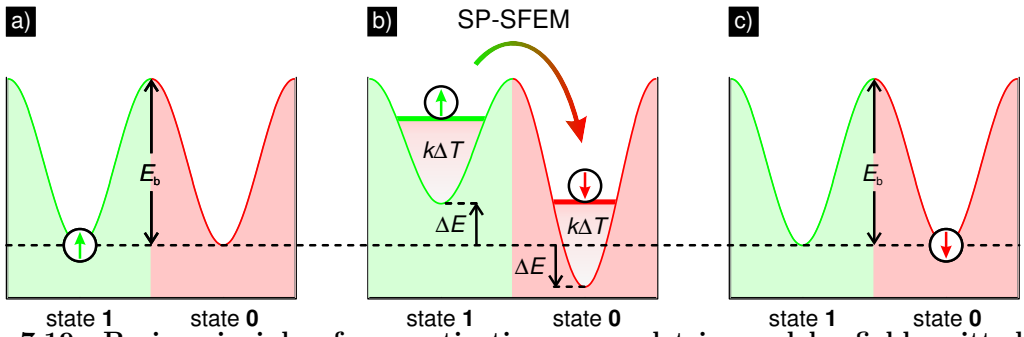

Figure 7.19: Basic principle of magnetization reversal triggered by field-emitted electrons. Energy landscape for a quasistable nanomagnet. (**a**) Initial state. The high effective energy barrier E_{b} prevents thermal switching events. (**b**) Application of a high spin-polarized field emission current. The temperature rise ΔT due to Joule heating decreases the mean lifetime of both states, and the spin torque (ΔE) removes the degeneracy of the state lifetimes, thereby favoring a magnetization reversal from state 1 to 0. (**c**) Final state. The nanomagnet is in the magnetic state 0, and E_{b} hinders again magnetization reversal.

In Fig. 7.20(a), an SP-STM magnetic map of four Fe/W(110) nanomagnets is shown. The magnetic state of the respective nanomagnet is color-coded on top of the topography. Three of them exhibit a stable magnetization. On the smallest nanomagnet a typical stripe pattern is observed due to thermal switching of the magnetization while imaging line by line (cf. Chap. 5). The tip was positioned above the indicated nanomagnet in the magnetic state 1. Then, a spin-polarized field emission current is applied and ramped up and down from 2-70 nA while simultaneously recording the magnetic $\mathrm{d}I/\mathrm{d}U$ signal. The $\mathrm{d}I/\mathrm{d}U$ signal as a function of emission current I is plotted in Fig. 7.20(c). $\mathrm{d}I/\mathrm{d}U$ increases with I, reflecting the enhanced conductance at smaller tip-sample distances. The $\mathrm{d}I/\mathrm{d}U$ downward curve initially fits the upward curve, but a sudden decrease of $\mathrm{d}I/\mathrm{d}U$ is observed at $I \approx 63\,\mathrm{nA}$, causing a deviation from the upward curve. This behavior indicates a switching event of the nanomagnet. A subsequently recorded SP-STM image on the same area revealed that the nanomagnet had in fact switched to the magnetic state 0, whereas the surrounding remained unchanged, as shown in Fig. 7.20(b). From a long-term SP-STM observation with low-energy tunneling

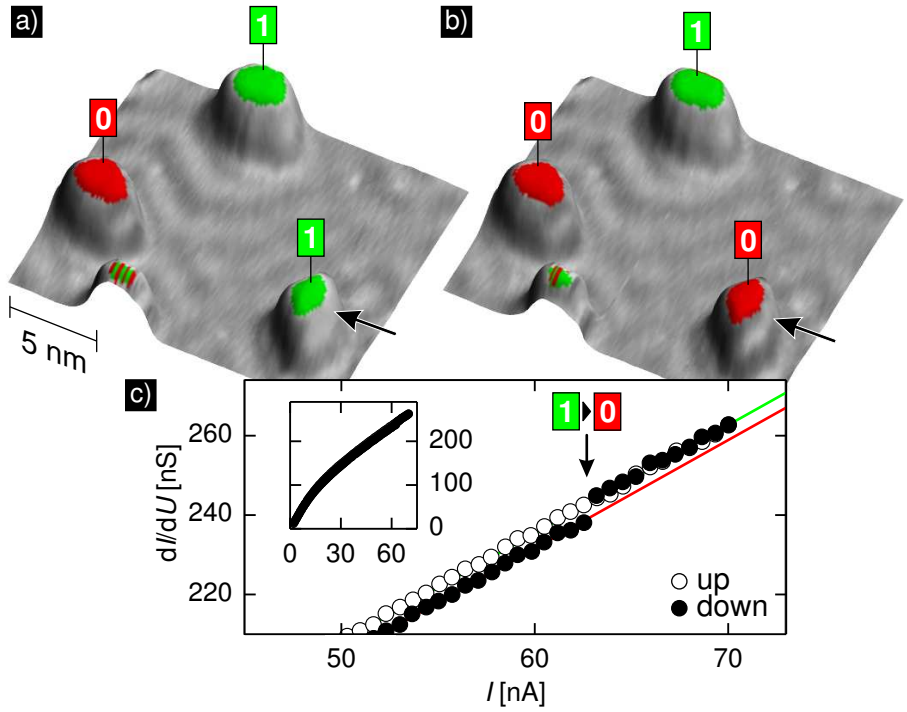

Figure 7.20: Magnetization reversal triggered by field-emitted electrons. SP-STM topography textured with a magnetic map of the sample. (**a**) Before and (**b**) after ramping a field emission current on one individual nanomagnet marked by the arrow. $U = 100\,\mathrm{mV}$, $I = 2\,\mathrm{nA}$, $T = 31.5\,\mathrm{K}$, bulk Cr-tip. (**c**) $\mathrm{d}I/\mathrm{d}U$ signal while ramping I up and down on the nanomagnet using field-emitted electrons. A jump is observed at $I \approx 63\,\mathrm{nA}$, indicating magnetization reversal. Red and green lines indicate the $\mathrm{d}I/\mathrm{d}U$ signal for state 0 and 1. $U = 5\,\mathrm{V}$.

electrons the intrinsic lifetime was found to be about one hour. With a field emission current sweep rate of 8.5 nA/s, the mean lifetime of the nanomagnet in the current window between 60 and 70 nA can be estimated to be a few seconds. Consequently, spin-polarized field emission significantly reduces the state lifetime of the nanomagnet, ultimately resulting in the magnetization becoming unstable and inducing switching.

Repeating this experiment several times showed that magnetization reversals are triggered preferentially at $I \approx 60\,\mathrm{nA}$. However, magnetization reversal occurs irrespective of the initial magnetic state, so Joule heating must be the main driving force for triggering, whereas the spin-transfer torque plays only a minor role. From the dimensions of the nanomagnet, the effective energy barrier can be estimated to $E_\mathrm{B} = (170 \pm 20)\,\mathrm{meV}$ [190], resulting in a Joule heating $\Delta T \approx 4\,\mathrm{K}$ for $I = 60\,\mathrm{nA}$.

Note that the low threshold of only some tens of nA using field-emitted electrons is tiny compared to experiments using low-energy tunneling electrons on the same sample system, where typical threshold currents in the μA range were employed [244]. Compared to these tunneling experiments the distance of the tip to the sample surface is an order of magnitude larger. This is advantageous as it avoids the risk of accidental tip-sample collisions during magnetization switching.

Chapter 8

Summary and Perspectives

A new technique for magnetic imaging and switching of atomic-scale magnets based on spin-polarized field emission is described in this thesis. Local injection of spin-polarized field-emitted electrons is achieved by approaching a biased magnetic tip to a few nm above a metallic sample surface in a scanning tunneling microscope under UHV conditions. Magnetic imaging is achieved via spin-polarized field emission conductance measurements. This spin-sensitive local probe technique is called *spin-polarized scanning field emission microscopy* (SP-SFEM). It allows the fundamental microscopic processes involved in the interaction of individual atomic-scale magnets with spin-polarized field-emitted electrons to be investigated.

A prerequisite for the experiments is a magnetic tip generating a spin-polarized field emission current. To avoid dipolar interactions, antiferromagnetic field emitters made of chromium (Cr) were used, demonstrating an electron spin-polarization in field emission from an *antiferromagnetic* bulk material.

The characterization of the bulk Cr tips was performed on the well-known system of the Fe mono- and double layer on W(110) since it exhibits a variety of magnetization directions. The measurements were made using spin-polarized scanning tunneling microscopy (SP-STM) and spectroscopy at low temperatures. A detailed bias-dependent study of the spatial magnetic sensitivity reveals that all magnetic directions are sensed over a wide bias range, with tunable sensitivities to certain magnetization directions at chosen sample bias voltages. The canted magnetization of bulk Cr tips makes them ideal for investigations of any magnetic configuration after characterization on a reference system like Fe/W(110). In addition, bulk Cr tips exhibit magnetic sensitivity over a wide temperature range. Hence, they can be used both for the generation of spatially-resolved magnetic maps and for spin-polarized spectroscopy and also for studying temperature-dependent magnetic phenomena. Since these tips do not need an extended *in situ* preparation like thin-film coated tips, a tip exchange mechanism is no longer

mandatory for SP-STM investigations. In principle, any standard scanning tunneling microscope can be operated in spin-polarized mode using Cr tips.

Field emission of spin-polarized electrons is induced by applying a high electric field on the order of GV/m to these bulk Cr tips. The electrons were resonantly injected into nanomagnets consisting of about 50 iron atoms on a tungsten substrate. Spin-polarized field emission conductance measurements reveal that the field-emission resonance (FER) states located nanometers above these magnets in vacuo exhibit a significant exchange splitting. The FER states serve as sensor for the underlying magnetic structure and allow for resonant magnetic imaging of atomic-scale magnetism even at tip-sample distances of about 2 nm.

The thermally-driven magnetization reversal of the nanomagnets is strongly affected by hot-electron spin injection. Increasing the field emission current significantly increases the thermal switching frequency of the nanomagnet, indicating considerable Joule heating. Additionally, the spin-polarized field emission current forces the nanomagnet to favor one of its magnetic states at the expense of the other, experimentally demonstrating the spin-transfer torque exerted by the field-emitted spins.

Field emission and tunnel currents can be varied by orders of magnitude simply by altering the tip-sample distance at constant sample bias and thus constant *energy* of the charge carriers. Comparative lifetime analyses with hot field-emitted and low-energy tunneling electrons reveal significant differences in the respective heat dissipation and spin-transfer torque effects. Owing to different energy relaxation mechanisms for low-energy tunneling and higher energy field-emitted electrons, the effective temperature increase of the nanomagnet depends not only on the power but also on the electron energy. Tunneling electrons predominantly excite phonons within the nanomagnet, however, field-emitted electrons mainly excite hot electrons, which thermalize outside the nanomagnet within the substrate. As a result, the overall phonon generation and thus the heat dissipation *within* the nanomagnet is less for SP-SFEM than for SP-STM. Whereas the spin-transfer torque contribution for tunneling electrons scales linearly with the current and is mainly caused by low-energy magnon formation, a stronger effect is found in field emission. This indicates an enhancement in the spin-transfer torque per electron with increasing emission current, presumably due to the excitation of higher energy Stoner modes.

Using spin-polarized field emission current injection the combined effects of Joule heating and spin-transfer torque can trigger magnetization reversal in otherwise thermally-stable nanomagnets. Thus, SP-SFEM has the capability of controlled magnetization switching on the atomic scale. By adjusting the electric field between the SP-SFEM probe tip and the nanomagnet the emission current can be used to read out the state of an individual nanomagnet and also to intentionally reverse its magnetization. The distance between the tip and the magnet is in the

regime of several nanometers, comparable to the technically feasible read/write head-media distances in today's magnetic data storage devices.

These experiments may stimulate the development of future magnetic data storage applications. Here, the conventional read/write head could be replaced by a single sharp magnetic needle, the data being read out and written via field emission. The state of the bit, e.g. represented by an individual nanomagnet, is read out by conductance measurements at low emission current, while at high emission current the electron spin forces the bit to reverse its orientation, assisted by a considerable local heating due to the electron bombardment. In contrast to conventional data storage devices, a magnetic field is no longer mandatory in the writing process. Since precise emission current injection allows to adress single bits on a very local scale, this read/write technique would permit a drastic increase in the data storage density.

In conclusion, this work provides insight into the microscopic details of the interplay between field-emitted hot-electron spins and magnets on the atomic scale and opens the pathway toward new scientific and technological applications based on magnetic imaging and switching using spin-polarized field emission.

Bibliography

[1] A. Fert, Angew. Chem. Int. Ed. **47**, 5956 (2008).

[2] S. S. P. Parkin, X. Jiang, C. Kaiser, A. Panchula, K. Roche, and M. Samant, Proc. IEEE **91**, 661 (2003).

[3] R. Jansen, J. Phys. D: Appl. Phys. **36**, R289 (2003).

[4] S. A. Wolf, D. D. Awschalom, R. A. Buhrman, J. M. Daughton, S. von Molnár, M. L. Roukes, A. Y. Chtchelkanova, and D. M. Treger, Science **294**, 1488 (2001).

[5] M. N. Baibich, J. M. Broto, A. Fert, F. N. V. Dau, F. Petroff, P. Etienne, G. Creuzet, A. Friederich, and J. Chazelas, Phys. Rev. Lett. **61**, 2472 (1988).

[6] J. S. Moodera, L. R. Kinder, T. M. Wong, and R. Meservey, Phys. Rev. Lett. **74**, 3273 (1995).

[7] E. Beaurepaire, J.-C. Merle, A. Daunois, and J.-Y. Bigot, Phys. Rev. Lett. **76**, 4250 (1996).

[8] C. Stamm, T. Kachel, N. Ponzius, R. Mitzner, T. Quast, K. Holldack, S. Khan, C. Lupulescu, E. F. Aziz, M. Wietstruk, et al., Nature Mater. **6**, 740 (2007).

[9] B. Koopmans, G. Malinowski, F. Dalla Longa, D. Steiauf, M. Fänle, T. Roth, M. Cinchetti, and M. Aeschlimann, Nature Mater. **9**, 259 (2010).

[10] E. Turgut, C. La-o-vorakiat, J. M. Shaw, P. Grychtol, H. T. Nembach, D. Rudolf, R. Adam, M. Aeschlimann, C. M. Schneider, T. J. Silva, et al., Phys. Rev. Lett. **110**, 197201 (2013).

[11] C. D. Stanciu, F. Hansteen, A. V. Kimel, A. Kirilyuk, A. Tsukamoto, A. Itoh, and T. Rasing, Phys. Rev. Lett. **99**, 047601 (2007).

[12] M. Plihal, D. L. Mills, and J. Kirschner, Phys. Rev. Lett. **82**, 2579 (1999).

[13] H. Pinkvos, H. Poppa, E. Bauer, and J. Hurst, Ultramicrosc. **47**, 339 (1992).

[14] W. H. Rippard and R. A. Buhrman, Appl. Phys. Lett. **75**, 1001 (1999).

[15] A. B. Schmidt, M. Pickel, M. Wiemhöfer, M. Donath, and M. Weinelt, Phys. Rev. Lett. **95**, 107402 (2005).

[16] A. B. Schmidt, M. Pickel, M. Donath, P. Buczek, A. Ernst, V. P. Zhukov, P. M. Echenique, L. M. Sandratskii, E. V. Chulkov, and M. Weinelt, Phys. Rev. Lett. **105**, 197401 (2010).

[17] H.-W. Fink, Phys. Scr. **38**, 260 (1988).

[18] N. D. Lang, A. Yacoby, and Y. Imry, Phys. Rev. Lett. **63**, 1499 (1989).

[19] R. Fowler and L. Nordheim, Proc. R. Soc. London, Ser. A **119**, 173 (1928).

[20] M. Hofmann, G. Regenfus, and O. Schärpf, Phys. Lett. **25A**, 270 (1967).

[21] M. Landolt and Y. Yafet, Phys. Rev. Lett. **40**, 1401 (1978).

[22] S. Crampin, Phys. Rev. Lett. **95**, 046801 (2005).

[23] A. Kubetzka, M. Bode, and R. Wiesendanger, Appl. Phys. Lett. **91**, 012508 (2007).

[24] F. J. Himpsel, Phys. Rev. B **43**, 13394 (1991).

[25] M. Donath, C. Math, M. Pickel, A. B. Schmidt, and M. Weinelt, Surf. Sci. **601**, 5701 (2007).

[26] S. Murphy, J. Osing, and I. V. Shvets, Appl. Surf. Sci. **144-145**, 497 (1999).

[27] M. Cavallini and F. Biscarini, Rev. Sci. Instr. **71**, 4457 (2000).

[28] C. Albonetti, I. Bergenti, M. Cavallini, V. Dediu, M. Massi, J.-F. Moulin, and F. Biscarini, Rev. Sci. Instr. **73**, 4254 (2002).

[29] S. F. Ceballos, G. Mariotto, S. Murphy, and I. V. Shvets, Surf. Sci. **523**, 131 (2003).

[30] A. Li Bassi, C. S. Casari, D. Cattaneo, F. Donati, S. Foglio, M. Passoni, C. E. Bottani, P. Biagioni, A. Brambilla, M. Finazzi, et al., Appl. Phys. Lett. **91**, 173120 (2007).

[31] A. A. Minakov and I. V. Shvets, Surf. Sci. **236**, L377 (1990).

[32] R. Wiesendanger, Rev. Mod. Phys. **81**, 1495 (2009).

[33] S. Krause, Ph.D. thesis, University of Hamburg (2008).

[34] P. Ebert, in *Probing the Nanoworld. Microscopies, Scattering and Spectroscopies of the Solid State, Schriften des Forschungszentrums Jülich, Materie und Material.* (2007), vol. 34.

[35] J. Bardeen, Phys. Rev. Lett. **6**, 57 (1961).

[36] J. Tersoff and D. R. Hamann, Phys. Rev. Lett. **50**, 1998 (1983).

[37] J. Tersoff and D. R. Hamann, Phys. Rev. B **31**, 805 (1985).

[38] N. D. Lang, Phys. Rev. Lett. **56**, 1164 (1986).

[39] L. Bartels, G. Meyer, and K.-H. Rieder, Appl. Phys. Lett. **71**, 213 (1997).

[40] K. von Bermann, M. Bode, A. Kubetzka, M. Heide, S. Blügel, and R. Wiesendanger, Phys. Rev. Lett. **92**, 046801 (2004).

[41] R. M. Feenstra, J. A. Strocio, and A. P. Fein, Surf. Sci. **181**, 295 (1987).

[42] V. A. Ukraintsev, Phys. Rev. B **53**, 11176 (1996).

[43] J. Li, W.-D. Schneider, and R. Berndt, Phys. Rev. B **56**, 7656 (1997).

[44] J. C. Slonczewski, Phys. Rev. B **39**, 6995 (1989).

[45] M. Julliere, Phys. Lett. A **54**, 225 (1975).

[46] R. Wiesendanger, H. J. Güntherodt, G. Güntherodt, R. J. Gambino, and R. Ruf, Phys. Rev. Lett. **65**, 247 (1990).

[47] D. Wortmann, S. Heinze, P. Kurz, G. Bihlmayer, and S. Blügel, Phys. Rev. Lett. **86**, 4132 (2001).

[48] W. Schottky, Z. Physik **14**, 63 (1923).

[49] R. W. Wood, Phys. Rev. **5**, 1 (1897).

[50] R. A. Milikan and C. F. Eyring, Phys. Rev. **27**, 51 (1926).

[51] R. A. Milikan and C. C. Lauritsen, Proc. Nat. Acad. Sci. **14**, 45 (1928).

[52] A. Modinos, Solid State Electron. **45**, 809 (2001).

[53] R. G. Forbes, Ultramicrosc. **79**, 11 (1999).

[54] E. L. Murphy and R. H. Good, Phys. Rev. **102**, 1464 (1956).

[55] L. W. Nordheim, Proc. Roy. Soc. London A **121**, 626 (1928).

[56] A. Sommerfeld and H. Bethe, in *Handbuch der Physik*, edited by H. Geiger and K. Scheel (H. Geiger and K. Scheel, Verlag Springer Julius, Berlin, 1933), vol. 24, p. 442.

[57] H. Jeffreys, Proc. London Math. Soc. **23**, 428 (1925).

[58] D. Bohm, *Quantum Theory* (Prentice-Hall, Englewood Cliffs, NJ, 1951).

[59] R. D. Young, Phys. Rev. **113**, 110 (1959).

[60] J. W. Gadzuk and E. W. Plummer, Rev. Mod. Phys. **45**, 487 (1973).

[61] P. H. Cutler, J. He, J. Miller, N. M. Miskovsky, B. Weiss, and T. E. Sullivan, Progr. Surf. Sci. **42**, 169 (1993).

[62] R. E. Burgess, H. Kroemer, and J. M. Houston, Phys. Rev. **90**, 515 (1953).

[63] J. W. Gadzuk, Phys. Rev. B **47**, 12832 (1993).

[64] E. W. Müller, Z. Physik **108**, 668 (1938).

[65] R. Haefer, Z. Physik **116**, 604 (1940).

[66] E. W. Müller, Z. Physik **106**, 541 (1937).

[67] R. P. Little and W. T. Whitney, J. Appl. Phys. **34**, 2430 (1963).

[68] D. Alpert, D. A. Lee, E. M. Lyman, and H. E. Tomaschke, J. Vac. Sci. Technol. **1**, 35 (1964).

[69] C. J. Bennette, R. W. Strayer, E. C. Strayer, E. C. Cooper, and L. W. Swanson, AIAA Journal **3**, 284 (1965).

[70] A. Dangwal, Ph.D. thesis, University of Wuppertal, Germany (2007).

[71] I. S. Hwang, H. S. Kuo, C.-C. Chang, and T. T. Tsong, J. Electrochem. Soc. **157**, 7 (2010).

[72] S. Horch and R. Morin, J. Appl. Phys. **74**, 3652 (1993).

[73] V. T. Binh and N. García, Ultramicrosc. **42-44**, 80 (1992).

[74] J. He, P. H. Cutler, and N. M. Miskovsky, Appl. Phys. Lett. **59**, 1644 (1991).

[75] D. A. Kirkpatrick, A. Mankofsky, and K. T. Tsang, Appl. Phys. Lett. **60**, 2065 (1992).

[76] D. Atlan, G. Gardet, V. T. Binh, N. García, and J. J. Sáenz, Ultramicrosc. **42-44**, 154 (1992).

[77] L.-H. Pan, T. E. Sullivan, V. J. Peridier, P. H. Cutler, and N. M. Miskovsky, Appl. Phys. Lett. **65**, 2151 (1994).

[78] J. D. Zuber, K. L. Jensen, and T. E. Sullivan, J. Appl. Phys. **91**, 9379 (2002).

[79] A. Kyritsakis, G. C. Kokkorakis, J. P. Xanthakis, T. L. Kirk, and D. Pescia, Appl. Phys. Lett. **97**, 023104 (2010).

[80] R. Wu and A. J. Freeman, Phys. Rev. Lett. **69**, 2867 (1992).

[81] E. Fues and H. Hellmann, Phys. Z. **31**, 465 (1930).

[82] H. v. Issendorff and R. Fleischmann, Z. Physik **167**, 11 (1962).

[83] W. T. Pimbley and E. W. Müller, J. Appl. Phys. **33**, 238 (1962).

[84] W. Gleich, R. Regenfos, and R. Sizmann, Phys. Rev. Lett. **27**, 1066 (1971).

[85] N. Müller, W. Eckstein, W. Heiland, and W. Zinn, Phys. Rev. Lett. **29**, 1651 (1972).

[86] N. Müller, Phys. Lett. **54 A**, 415 (1975).

[87] E. Kisker, G. Baum, A. H. Mahan, W. Raith, and K. Schrödder, Phys. Rev. Lett. **36**, 982 (1976).

[88] M. Campagna, T. Utsumi, and D. N. E. Buchanan, J. Vac. Sci. Technol. **13**, 193 (1976).

[89] G. Chrobok and M. Hofmann, Phys. Lett. **57 A**, 257 (1976).

[90] G. Chrobok, M. Hofmann, G. Regenfus, and R. Sizmann, Phys. Rev. B **15**, 429 (1977).

[91] M. Landolt and M. Campagna, Phys. Rev. Lett. **38**, 663 (1977).

[92] M. Landolt and Y. Yafet, Phy. Rev. Lett. **40**, 1401 (1978).

[93] R. Meservey and P. M. Tedrow, Phys. Rep. **238**, 173 (1994).

[94] R. Bryl and M. S. Altman, J. Appl. Phys. **94**, 4670 (2003).

[95] Y. R. Niu and M. S. Altman, Suf. Sci. **604**, 1055 (2010).

[96] Y. R. Niu and M. S. Altman, Appl. Phys. Lett. **95**, 203113 (2009).

[97] T. Irisawa, T. K. Tamada, and T. Mizoguchi, New. J. Phys. **11**, 113031 (2009).

[98] S. Nagai, Y. Fujiwara, and K. Hata, Surf. and Interf. Anal. **40**, 1673 (2008).

[99] S. Nagai, Y. Fujiwara, and K. Hata, Ultramicrosc. **109**, 395 (2009).

[100] P. M. Echenique and J. B. Pendry, J. Phys. C: Solid State Phys. **11**, 2065 (1978).

[101] V. Dose, W. Altmann, A. Goldmann, U. Kolac, and J. Rogozik, Phys. Rev. Lett. **52**, 1919 (1984).

[102] D. Straub and F. J. Himpsel, Phys. Rev. Lett. **52**, 1922 (1984).

[103] T. Mayer-Kuckuk, *Atomphysik* (Teubner Studienbücher, Stuttgart, 1997).

[104] P. M. Echenique and J. B. Pendry, Prog. Surf. Sci. **32**, 111 (1989).

[105] E. G. McRae, Rev. Mod. Phys. **51**, 541 (1979).

[106] N. V. Smith, Phys. Rev. B **32**, 3549 (1985).

[107] D. Straub and F. J. Himpsel, Phys. Rev. B **33**, 2256 (1986).

[108] G. Binnig, K. H. Frank, H. Fuchs, N. Garcia, B. Reihl, H. Rohrer, F. Salvan, and A. R. Williams, Phys. Rev. Lett. **55**, 991 (1985).

[109] J. B. Pendry, C. G. Larsson, and P. M. Echenique, Surf. Sci. **166**, 57 (1986).

[110] M. Weinelt, J. Phys.: Condens. Matter **14**, R1099 (2002).

[111] P. M. Echenique, R. Berndt, E. V. Chulkov, T. Fauster, A. Goldmann, and U. Höfer, Surf. Sci. Rep. **52**, 219 (2004).

[112] G. Borstel and G. Thörner, Surf. Sci. Rep. **8**, 1 (1987).

[113] F. Passek and M. Donath, Phys. Rev. Lett. **69**, 1101 (1992).

[114] K. Starke, K. Ertl, and V. Dose, Phys. Rev. B **45**, 6154 (1992).

[115] F. Passek, M. Donath, K. Ertl, and V. Dose, Phys. Rev. Lett. **75**, 2746 (1995).

[116] S. Bode, K. Starke, P. Rech, and G. Kaindl, Phys. Rev. Lett. **72**, 1072 (1994).

[117] S. Bode, K. Starke, and G. Kaindl, Phys. Rev. **60**, 2946 (1999).

[118] C. Math, Ph.D. thesis, University of Bayreuth, Germany (2000).

[119] F. J. Himpsel, J. A. Knapp, and D. E. Eastman, Phys. Rev. B **19**, 2919 (1979).

[120] D. E. Eastman, F. J. Himpsel, and J. A. Knapp, Phys. Rev. Lett. **44**, 95 (1980).

[121] A. Santoni and F. J. Himpsel, Phys. Rev. B **43**, 1305 (1991).

[122] R. Fischer, N. Fischer, S. Schuppler, T. Fauster, and F. J. Himpsel, Phys. Rev. B **46**, 9691 (1992).

[123] J. Stark, Ann. d. Phys. **348**, 965 (1914).

[124] T. Ando, A. B. Fowler, and F. Stern, Rev. Mod. Phys. **54**, 437 (1982).

[125] A. Hanuschkin, D. Wortmann, and S. Blügel, Phys. Rev. B **76**, 165417 (2007).

[126] R. Young, J. Ward, and F. Scire, Phys. Rev. Lett. **27**, 922 (1971).

[127] R. Young, J. Ward, and F. Scire, Rev. Sci. Instr. **43**, 999 (1972).

[128] J. G. Simmons, J. Appl. Phys. **34**, 1793 (1963).

[129] K. H. Gundlach, Solid State Electron. **9**, 949 (1966).

[130] J. H. Coombs and K. K. Gimzewski, J. of Microscopy **152**, 841 (1988).

[131] R. S. Becker, J. A. Golovchenko, and B. S. Swartzentruber, Phys. Rev. Lett. **55**, 987 (1985).

[132] R. Wiesendanger, *Scanning Probe Microscopy and Spectroscopy: Methods and Applications* (Cambridge Univ. Press, Cambridge, 1994).

[133] A. J. Jason, Phys. Rev. B **156**, 266 (1967).

[134] B. T. Jonker, N. C. Bartelt, and R. L. Park, Surf. Sci. **127**, 183 (1983).

[135] J. Maserjian, J. Vac. Sci. Technol. **11**, 996 (1974).

[136] G. P. Petersson, C. M. Svensson, and J. Maserjian, Solid-State Electron. **18**, 449 (1975).

[137] T. W. Hickmott, P. M. Solomon, R. Fischer, and H. Morkoc, Appl. Phys. Lett. **44**, 90 (1984).

[138] G. Binnig and R. Rohrer, Helv. Phys. Acta **55**, 726 (1982).

[139] J. A. Kubby, Y. R. Wang, and W. J. Greene, Phys. Rev. Lett. **65**, 2165 (1990).

[140] A. J. Caamaño, Y. Pogorelov, O. Custance, J. Méndez, A. M. Baró, J. Y. Veuillen, J. M. Gómez-Rodríguez, and J. J. Sáenz, Surf. Sci. **426**, L420 (1999).

[141] T. Jung, Y. W. Mo, and F. J. Himpsel, Phys. Rev. Lett. **74**, 1641 (1995).

[142] E. D. L. Rienks, N. Nilius, H.-P. Rust, and H.-J. Freund, Phys. Rev. B **71**, 241404(R) (2005).

[143] M. Pivetta, F. Patthey, M. Stengel, A. Baldereschi, and W.-D. Schneider, Phys. Rev. B **72**, 115404 (2005).

[144] H.-C. Ploigt, C. Brun, M. Pivetta, F. Patthey, and W.-D. Schneider, Phys. Rev. B **76**, 195404 (2007).

[145] P. Wahl, M. A. Schneider, L. Diekhöner, R. Vogelgesang, and K. Kern, Phys. Rev. Lett. **91**, 106802 (2003).

[146] M. Roth, M. Weinelt, T. Fauster, P. Wahl, M. A. Schneider, L. Diekhöner, and K. Kern, Appl. Phys. A **78**, 155 (2004).

[147] S. Crampin, J. Kröger, H. Jensen, and R. Berndt, Phys. Rev. Lett. **95**, 029701 (2005).

[148] K. Schouteden and C. Van Haesendonck, Phys. Rev. Lett. **103**, 266805 (2009).

[149] K. Schouteden and C. Van Haesendonck, Phys. Rev. Lett. **108**, 076806 (2012).

[150] B. Borca, S. Barja, M. Garnica, D. Sánchez-Portal, V. M. Silkin, E. V. Chulkov, C. F. Hermanns, J. J. Hinarejos, A. L. Vázquez de Parga, A. Arnau, et al., Phys. Rev. Lett. **105**, 036804 (2010).

[151] S. Bose, V. M. Silkin, R. Ohmann, I. Brihuega, L. Vitali, C. H. Michaelis, P. Mallet, J. Y. Veuillen, M. A. Schneider, E. V. Chulkov, et al., New. J. Phys. **12**, 023028 (2010).

[152] K. Schouteden, A. Volodin, D. A. Muzychenko, M. P. Chowdhury, A. Fonseca, J. B. Nagy, and C. van Haesendonck, Nanotechnology **21**, 485401 (2010).

[153] K. Bobrov, A. J. Mayne, and G. Dujardin, Nature **413**, 616 (2001).

[154] M. Bode, A. Wachowiak, J. Wiebe, A. Kubetzka, M. Morgenstern, and R. Wiesendanger, Appl. Phys. Lett. **84**, 948 (2004).

[155] A. Wachowiak, J. Wiebe, M. Bode, O. Pietzsch, M. Morgenstern, and R. Wiesendanger, Science **298**, 577 (2002).

[156] J. A. Venables, *Introduction to surface and thin film processes* (Cambride University Press, Cambridge, UK, 2000).

[157] Oxford Instruments Analytical GmbH, D-47589 Uedem (2013).

[158] Omicron Nanotechnology GmbH, D-65232 Taunusstein (2013).

[159] T. Hänke, Ph.D. thesis, University of Hamburg (2005).

[160] O. Pietzsch, A. Kubetzka, D. Haude, M. Bode, and R. Wiesendanger, Rev. Sci. Instr. **71**, 424 (2000).

[161] S. H. Pan, *Piezo-electric motor*, International Patent Publication Number WO 93/19494, International Bureau, World Intellectual Organization (1993).

[162] FEMTO Messtechnik GmbH, Berlin, Germany.

[163] CryoVac GmbH, D-53842 Troisdorf (1998).

[164] S. Krause, Diploma thesis, University of Hamburg (2003).

[165] A. Kubetzka, M. Bode, O. Pietzsch, and R. Wiesendanger, Phys. Rev. Lett. **88**, 057201 (2002).

[166] R. Wiesendanger, Rev. Mod. Phys. **81**, 1495 (2009).

[167] M. Bode, Rep. Progr. Phys. **66**, 523 (2003).

[168] M. Bode, S. Krause, L. Berbil-Bautista, S. Heinze, and R. Wiesendanger, Surf. Sci. **601**, 3308 (2007).

[169] http://www.webelements.de.

[170] P. J. Berlowitz, J.-W. He, and D. W. Goodman, Surf. Sci. **231**, 315 (1990).

[171] H. J. Elmers, J. Hauschild, H. Höche, U. Gradmann, H. Bethge, D. Heuer, and U. Köhler, Phys. Rev. Lett. **73**, 898 (1994).

[172] H. Bethge, D. Heuer, C. Jensen, K. Reshöft, and U. Köhler, Surf. Sci. **331–333**, 878 (1995).

[173] J. Hauschild, H. J. Elmers, and U. Gradmann, Phys. Rev. B **57**, R677 (1998).

[174] U. Gradmann, G. Liu, H. J. Elmers, and M. Przybylski, Hyp. Int. **57**, 1845 (1990).

[175] E. Bauer, Z. Kristallogr. **110**, 372 (1958).

[176] C. Jensen, K. Reshöft, and U. Köhler, Appl. Phys. A **62**, 217 (1996).

[177] A. Kubetzka, O. Pietzsch, M. Bode, and R. Wiesendanger, Phys. Rev. B **63**, 140407 (2001).

[178] J. Hauschild, U. Gradmann, and H. J. Elmers, Appl. Phys. Lett. **72**, 3211 (1998).

[179] H. J. Elmers, J. Hauschild, and U. Gradmann, J. Magn. Magn. Mater. **198**, 222 (1999).

[180] H. J. Elmers, J. Hauschild, and U. Gradmann, Phys. Rev. B **59**, 3688 (1999).

[181] E. Y. Vedmedenko, A. Kubetzka, K. von Bergmann, O. Pietzsch, M. Bode, J. Kirschner, H. P. Oepen, and R. Wiesendanger, Phys. Rev. Lett. **92**, 077207 (2004).

[182] S. Meckler, N. Mikuszeit, A. Preßler, E. Y. Vedmedenko, O. Pietzsch, and R. Wiesendanger, Phys. Rev. Lett. **103**, 157201 (2009).

[183] N. Weber, K. Wagner, H. J. Elmers, J. Hauschild, and U. Gradmann, Phys. Rev. B **55**, 14121 (1997).

[184] O. Pietzsch, A. Kubetzka, M. Bode, and R. Wiesendanger, Phys. Rev. Lett. **84**, 5212 (2000).

[185] O. Pietzsch, A. Kubetzka, M. Bode, and R. Wiesendanger, Science **292**, 2053 (2001).

[186] M. Bode, A. Kubetzka, O. Pietzsch, and R. Wiesendanger, Appl. Phys. A **72**, S149 (2001).

[187] M. Bode, S. Heinze, A. Kubetzka, O. Pietzsch, X. Nie, G. Bihlmayer, S. Blügel, and R. Wiesendanger, Phys. Rev. Lett. **89**, 237205 (2002).

[188] M. Bode, A. Kubetzka, S. Heinze, O. Pietzsch, R. Wiesendanger, M. Heide, X. Nie, G. Bihlmayer, and S. Blügel, J. Phys.: Condens. Matter **15**, S679 (2003).

[189] H. J. Elmers, J. Hauschild, and U. Gradmann, Phys. Rev. B **54**, 15224 (1996).

[190] S. Krause, G. Herzog, T. Stapelfeldt, L. Berbil-Bautista, M. Bode, E. Y. Vedmedenko, and R. Wiesendanger, Phys. Rev. Lett. **103**, 127202 (2009).

[191] M. Pratzer, H. J. Elmers, M. Bode, O. Pietzsch, A. Kubetzka, and R. Wiesendanger, Phys. Rev. Lett. **87**, 127201 (2001).

[192] M. Heide, G. Bihlmayer, and S. Blügel, Phys. Rev. B **78**, 140403(R) (2008).

[193] A. Kubetzka, O. Pietzsch, M. Bode, and R. Wiesendanger, Phys. Rev. B **67**, 020401 (2003).

[194] S. Krause, L. Berbil-Bautista, G. Herzog, M. Bode, and R. Wiesendanger, Science **317**, 1537 (2007).

[195] H.-B. Braun, Phys. Rev. Lett. **71**, 3557 (1993).

[196] H.-B. Braun, Phys. Rev. B **50**, 16501 (1994).

[197] H.-B. Braun, J. Appl. Phys. **85**, 6172 (1999).

[198] M. Bode, O. Pietzsch, A. Kubetzka, and R. Wiesendanger, Phys. Rev. Lett. **92**, 067201 (2004).

[199] M. L. Néel, Ann. Géophys. **5**, 99 (1949).

[200] W. F. Brown, Phys. Rev. **130**, 1677 (1963).

[201] W. Wernsdorfer, E. B. Orozco, K. Hesselbach, A. Benoit, B. Barbara, N. Demoney, A. Loiseau, H. Pascard, and D. Mailly, Phys. Rev. Lett. **78**, 1791 (1997).

[202] R. Wiesendanger, D. Bürgler, G. Tarrach, T. Schaub, U. Hartmann, H. J. Güntherodt, I. V. Shvets, and J. M. D. Coey, Appl. Phys. A **53**, 349 (1991).

[203] S. Blügel, D. Pescia, and P. H. Dederichs, Phys. Rev. B **39**, 1392 (1989).

[204] M. Kleiber, M. Bode, R. Ravlić, and R. Wiesendanger, Phys. Rev. Lett. **85**, 4606 (2000).

[205] A. J. Melmed, J. Vac: Sci. Technol. B **9**, 601 (1990).

[206] J. P. Ibe, P. P. Bey, S. L. Brandow, R. A. Brizzolara, N. A. Burnham, D. P. Dilella, K. P. Lee, C. R. K. Marrian, and R. J. Colton, J. Vac: Sci. Technol. A **8**, 3570 (1990).

[207] M. Bode, A. Kubetzka, O. Pietzsch, and R. Wiesendanger, Surf. Sci. **514**, 135 (2002).

[208] S. F. Alvarado, Phys. Rev. Lett. **75**, 513 (1995).

[209] K. von Bergmann, M. Bode, and R. Wiesendanger, J. Magn. Magn. Mater. **305**, 279 (2006).

[210] K. von Bergmann, M. Menzel, D. Serrate, Y. Yoshida, S. Schröder, P. Ferriani, A. Kubetzka, R. Wiesendanger, and S. Heinze, Phys. Rev. B **86**, 134422 (2012).

[211] J. D. Burton, R. F. Sabirianov, J. P. Velev, O. N. Mryasov, and E. Y. Tsymbal, Phys. Rev. B **76**, 144430 (2007).

[212] N. Néel, S. Schröder, N. Ruppelt, P. Ferriani, J. Kröger, R. Berndt, and S. Heinze, Phys. Rev. Lett. **110**, 037202 (2013).

[213] M. Bode, O. Pietzsch, A. Kubetzka, S. Heinze, and R. Wiesendanger, Phys. Rev. Lett. **86**, 2142 (2001).

[214] M. Bode, Rep. Prog. Phys. **66**, 523 (2003).

[215] L. Nordström and D. J. Singh, Phys. Rev. Lett. **76**, 4420 (1996).

[216] J. M. Pitarke, F. Flores, and P. M. Echenique, Surf. Sci. **234**, 1 (1990).

[217] B. C. Stipe, M. A. Rezaei, and W. Ho, Science **280**, 1732 (1998).

[218] U. Thomann, C. Reuß, T. Fauster, F. Passek, and M. Donath, Phys. Rev. B **61**, 16163 (2000).

[219] P. Wahl, M. A. Schneider, L. Diekhöner, R. Vogelgesang, and K. Kern, Phys. Rev. Lett. **95**, 029702 (2005).

[220] J. I. Pascual, C. Corriol, G. Ceballos, I. Aldazabal, H.-P. Rust, K. Horn, J. M. Pitarke, P. M. Echenique, and A. Arnau, Phys. Rev. B **75**, 165326 (2007).

[221] J. Bono and R. H. Good, Surf. Sci. **188**, 153 (1987).

[222] S. Krause, G. Herzog, A. Schlenhoff, A. Sonntag, and R. Wiesendanger, Phys. Rev. Lett. **107**, 186601 (2011).

[223] I. Bat'ko and M. Bat'ková, Eur. Phys. J. Appl. Phys. **31**, 191 (2005).

[224] L. Vitali, M. A. Schneider, L. Wirtz, A. Rubio, and K. Kern, Phys. Rev. B **69**, 121414 (2004).

[225] H. Gawronski, M. Mehlhorn, and K. Morgenstern, Science **319** (2008).

[226] W. A. Little, Can. J. Phys. **37**, 334 (1959).

[227] E. T. Swartz and R. O. Pohl, Rev. Mod. Phys. **61**, 605 (1989).

[228] J. H. Coombs, J. K. Gimzewski, B. Reihl, J. K. Sass, and R. R. Schlitter, J. Microsc. **152**, 325 (1988).

[229] R. Berndt, J. K. Gimzewski, and R. R. Schlitter, Ultramicrosc. **42-44**, 335 (1992).

[230] P. Johansson, R. Monreal, and P. Apell, Phys. Rev. B **42**, 9210 (1990).

[231] A. Eiguren, B. Hellsing, E. V. Chulkov, and P. M. Echenique, J. Electron Spec. Rel. Phen. **129**, 111 (2003).

[232] S. S. Tsirkin and S. V. Eremeev, Russ. Phys. J. **54**, 92 (2011).

[233] R. Zdyb, T. O. Menteş, A. Locatelli, M. A. Niño, and E. Bauer, Phys. Rev. B **87**, 075436 (2013).

[234] P. M. Echenique, J. M. Pitarke, E. V. Chulkov, and A. Rubio, Chem. Phys. **251**, 1 (2000).

[235] I. Y. Sklyadneva, A. Leonardo, P. M. Echenique, S. V. Eremeev, and E. V. Chulkov, J. Phys.: Condens. Matter **18**, 7323 (2006).

[236] B. N. J. Persson and J. E. Demuth, Sol. State Commun. **57**, 769 (1986).

[237] B. N. J. Persson and A. Baratoff, Phys. Rev. Lett. **59**, 339 (1987).

[238] Z. Li and S. Zhang, Phys. Rev. B **69**, 134416 (2004).

[239] T. Balashov, A. F. Takács, W. Wulfhekel, and J. Kirschner, Phys. Rev. Lett. **97**, 187201 (2006).

[240] J. Hong and D. L. Mills, Phys. Rev. B **62**, 5589 (2000).

[241] J. Prokop, W. X. Tang, Y. Zhang, I. Tudosa, T. R. F. Peixoto, K. Zakeri, and J. Kirschner, Phys. Rev. Lett. **102**, 177206 (2009).

[242] A. Bergman, A. Taroni, L. Bergqvist, J. Hellsvik, B. Hjörvarsson, and O. Eriksson, Phys. Rev. B **81**, 144416 (2010).

[243] L. Bergmann and C. Schaefer, eds., *Lehrbuch der Experimentalphysik; Bd. 2: Elektromagnetismus* (de Gruyter, 2006).

[244] G. Herzog, S. Krause, and R. Wiesendanger, Appl. Phys. Lett. **96**, 102505 (2010).

Publications

Research articles

- A. Schlenhoff, S. Krause, A. Sonntag, and R. Wiesendanger, *Individual atomic-scale magnets interacting with spin-polarized field-emitted electrons*, Phys. Rev. Lett. **109**, 097602 (2012).
- S. Krause, G. Herzog, A. Schlenhoff, A. Sonntag, and R. Wiesendanger, *Joule heating and spin-transfer torque investigated on the atomic scale using a spin-polarized scanning tunneling microscope*, Phys. Rev. Lett. **107**, 186601 (2011).
- A. Schlenhoff, S. Krause, G. Herzog, and R. Wiesendanger, *Bulk Cr tips with full spatial magnetic sensitivity for spin-polarized scanning tunneling microscopy*, Appl. Phys. Lett. **97**, 083104 (2010).

Awards

- 2012-09-05:
  ECOSS Prize 2012,
  29^{th} European Conference on Surface Science (ECOSS-29), Edinburgh (UK).

Conferences

Invited talks

- 2013-06-14:
  Nanomagnets interacting with spin-polarized electrons from Stark-shifted image-potential states, Group seminar AG Prof. M. Weinelt, FU Berlin, Berlin (Germany).

- 2013-03-14:
  Spin-polarized scanning field emission microscopy and spectroscopy, 77^{th} Spring Conference, Deutsche Physikalische Gesellschaft, Regensburg (Germany).

- 2012-06-12:
  Individual atomic-scale magnets interacting with spin-polarized field-emitted electrons, Seminar of the SFB616 'Energy Dissipation at Surfaces', University of Duisburg-Essen, Duisburg (Germany).

Contributed talks

- 2012-09-11:
  A. Schlenhoff, S. Krause, A. Sonntag, and R. Wiesendanger, *Spin-transfer torque and Joule heating generated by spin-polarized field-emitted electrons*, 6^{th} International Conference on SPS and 4^{th} International Workshop on SP-STM, Timmendorfer Strand (Germany).

- 2012-09-05:
  A. Schlenhoff, S. Krause, A. Sonntag, and R. Wiesendanger, *Spin-transfer torque and Joule heating generated by spin-polarized field-emitted electrons*, 29^{th} European Conference on Surface Science (ECOSS-29), Edinburgh (UK).

- 2012-07-25:
  A. Schlenhoff, S. Krause, A. Sonntag, and R. Wiesendanger, *Spin-transfer torque and Joule heating of field-emitted electrons*, International Conference on Nanoscience and Technology (ICN+T), Paris (France).

- 2012-07-25:
  S. Krause, G. Herzog, A. Schlenhoff, A. Sonntag, and R. Wiesendanger, *Joule heating and spin-transfer torque investigated on the atomic scale using SP-STM*, International Conference on Nanoscience and Technology (ICN+T), Paris (France).

- 2012-07-12:
  A. Schlenhoff, S. Krause, A. Sonntag, and R. Wiesendanger, *Spin-transfer torque and Joule heating of field-emitted electrons*, International Conference on Magneticm (ICM), Busan (Republic of Korea).

- 2012-07-12:
  S. Krause, G. Herzog, A. Schlenhoff, A. Sonntag, and R. Wiesendanger, *Joule heating and spin-transfer torque investigated on the atomic scale using SP-STM*, International Conference on Magneticm (ICM), Busan (Republic of Korea).

- 2012-03-29:
  A. Schlenhoff, S. Krause, A. Sonntag, and R. Wiesendanger, *Spin-transfer torque and Joule heating of field-emitted electrons*, 76^{th} Spring Conference, Deutsche Physikalische Gesellschaft, Berlin (Germany).

- 2012-03-29:
  A. Sonntag, S. Krause, G. Herzog, A. Schlenhoff, and R. Wiesendanger, *Spin-transfer torque switching efficiency in SP-STM experiments*, 76^{th} Spring Conference, Deutsche Physikalische Gesellschaft, Berlin (Germany).

- 2011-03-18:
  A. Schlenhoff, A. Sonntag, S. Krause, and R. Wiesendanger, *Observation of superparamagnetism in image potential states using SP-STM*, 75^{th} Spring Conference, Deutsche Physikalische Gesellschaft, Dresden (Germany).

- 2010-08-24:
  A. Schlenhoff, S. Krause, G. Herzog, and R. Wiesendanger, *Cr bulk tips for SP-STM with both in-plane and out-of-plane sensitivity*, International Conference on Nanoscience and Technology (ICN+T), Beijing (China).

- 2010-08-24:
  S. Krause, G. Herzog, A. Schlenhoff, and R. Wiesendanger, *Critical current for switching the magnetization of quasistable nano-islands using SP-STM*, International Conference on Nanoscience and Technology (ICN+T), Beijing (China).

- 2010-08-24:
  G. Herzog, S. Krause, A. Schlenhoff, and R. Wiesendanger, *Spin Torque Switching of Nanomagnets by SP-STM*, International Conference on Nanoscience and Technology (ICN+T), Beijing (China).

- 2010-08-20:
  G. Herzog, S. Krause, A. Schlenhoff, and R. Wiesendanger, *Spin Torque Switching of Nanomagnets by SP-STM*, International Workshop on Spin-Polarized Scanning Tunneling Microscopy (SP-STM3), Seoul (Republic of Korea).

- 2010-08-19:
  A. Schlenhoff, S. Krause, G. Herzog, and R. Wiesendanger, *Bulk Cr tips with full spatial magnetic sensitivity for spin-polarized scanning tunneling microscopy*, International Workshop on Spin-Polarized Scanning Tunneling Microscopy (SP-STM3), Seoul (Republic of Korea).

- 2010-08-19:
  S. Krause, G. Herzog, A. Schlenhoff, and R. Wiesendanger, *Critical current for switching the magnetization of quasistable nano-islands using SP-STM*, International Workshop on Spin-Polarized Scanning Tunneling Microscopy (SP-STM3), Seoul (Republic of Korea).

- 2010-03-25:
  A. Emmenegger*, S. Krause, G. Herzog, and R. Wiesendanger, *Cr Bulk Tips for Spin Polarized Scanning Tunneling Microscopy with both In-plane and Out-of-plane Sensitivity*, 74$^{\text{th}}$ Spring Conference, Deutsche Physikalische Gesellschaft, Regensburg (Germany).

- 2010-03-25:
  G. Herzog, S. Krause, A. Emmenegger*, and R. Wiesendanger, *Heat assisted Spin Torque Switching of Nanomagnets by SP-STM*, 74$^{\text{th}}$ Spring Conference, Deutsche Physikalische Gesellschaft, Regensburg (Germany).

- 2010-03-25:
  S. Krause, G. Herzog, A. Emmenegger*, and R. Wiesendanger, *Critical Current for Switching the Magnetization of Quasistable Nano-Islands Using SP-STM*, 74$^{\text{th}}$ Spring Conference, Deutsche Physikalische Gesellschaft, Regensburg (Germany).

*A. Schlenhoff, née Emmenegger

Posters

- 2013-03-12:
  J. Friedlein, A. Schlenhoff, A. Sonntag, S. Krause, and R. Wiesendanger, *Nanomagnets affected by spin-polarized tunneling and field-emission*, 77$^{\text{th}}$ Spring Conference, Deutsche Physikalische Gesellschaft, Regensburg (Germany).

- 2012-09-10:
  A. Sonntag, A. Schlenhoff, S. Krause, G. Herzog, and R. Wiesendanger, *Bulk Cr tips with full spatial magnetic sensitivity for spin-polarized scanning tunneling microscopy*, 6$^{\text{th}}$ International Conference on SPS and 4$^{\text{th}}$ International Workshop on SP-STM, Timmendorfer Strand (Germany).

- 2012-09-10:
  S. Krause, A. Sonntag, G. Herzog, A. Schlenhoff, and R. Wiesendanger, *Spin-transfer torque switching efficiency in SP-STM experiments*, 6$^{\text{th}}$ International Conference on SPS and 4$^{\text{th}}$ International Workshop on SP-STM, Timmendorfer Strand (Germany).

- 2012-07-12:
  A. Schlenhoff, A. Sonntag, S. Krause, G. Herzog, and R. Wiesendanger, *Bulk Cr tips with full spatial magnetic sensitivity for spin-polarized scanning tunneling microscopy*, International Conference on Magneticm (ICM), Busan (Republic of Korea).

- 2011-03-18:
  A. Engel, A. Schlenhoff, A. Sonntag, S. Krause, and R. Wiesendanger, *Preparation of bulk chromium tips for SP-STM*, 75$^{\text{th}}$ Spring Conference, Deutsche Physikalische Gesellschaft, Dresden (Germany).

- 2011-03-18:
  A. Sonntag, A. Schlenhoff, G. Herzog, S. Krause, B. Ehlers, and R. Wiesendanger, *Thermal magnetization reversal of small Fe-nanoislands on W(110)*, 75$^{\text{th}}$ Spring Conference, Deutsche Physikalische Gesellschaft, Dresden (Germany).

- 2009-07-27:
  A. Emmenegger[*], S. Krause, G. Herzog, A. Kubetzka, and R. Wiesendanger, *Observation of Superparamagnetic Fe/W(110) Nanoislands by SP-STM in the Field Emission Mode*, International Conference on Magnetism (ICM), Karlsruhe (Germany).

[*] A. Schlenhoff, née Emmenegger

- 2009-03-24:
  A. Emmenegger*, S. Krause, A. Kubetzka, G. Herzog, and R. Wiesendanger, *High Order Field Emission Resonances on W(110) and Fe/W(110) studied by Scanning Tunneling Spectroscopy*, 73rd Spring Conference, Deutsche Physikalische Gesellschaft, Dresden (Germany).

*A. Schlenhoff, née Emmenegger

Acknowledgements

Ich danke Herrn Prof. Dr. Roland Wiesendanger für die Möglichkeit, meine Promotion in seiner Forschungsgruppe unter hervorragenden Rahmenbedingungen durchführen zu können. Durch sein fortwährendes Vertrauen in meine Forschungen und meine Person erfuhr ich ein optimales Maß an Freiheit, Unterstützung und Förderung. Die in dieser Arbeit vorgestellten Experimente konnte ich so nicht nur erfolgreich durchführen, sondern diese auch auf internationalen Tagungen im wertvollen Austausch mit anderen Wissenschaftlern diskutieren.

Herrn Prof. Dr. Robert L. Johnson möchte ich ganz herzlich für die Übernahme des Gutachtens meiner Dissertation und Herrn Prof. Hans P. Oepen für die Übernahme des Gutachtens meiner Disputation danken.

Mein besonderer Dank gilt Herrn Dr. Stefan Krause für die kontinuierliche Betreuung sämtlicher Phasen meiner Promotion. Von seiner kompetenten Hilfe und Unterstützung sowie seinem kritischem Feedback profitierte ich sehr.

Meinem Kollegen Herrn Andreas Sonntag danke ich für seine experimentelle Unterstützung und für viele anregende Diskussionen. Das Forschen im Team des Labors 018 ist geprägt von außergewöhnlicher Kollegialität und einem sehr angenehmen Arbeitsklima. Dafür möchte ich mich zudem bei Herrn Johannes Friedlein, Herrn Jonas Harm, Herrn Jan Hermenau und meiner ehemaligen Kollegin Frau Dr. Gabriela Herzog bedanken.

Die gesamte Forschungsgruppe zeichnet sich durch ihre fachliche Diversität und ihren hohen Erfahrungsschatz aus. Ich danke allen Gruppenmitgliedern für die stetige Bereitschaft zur produktiven Diskussion und Hilfestellung. Mein besonderer Dank gilt Herrn Dr. André Kubetzka, Herrn Dr. Alexander Khajetoorians, Herrn Dr. Robert Wieser, Herrn Dr. Bruno Chillian und Herrn Dr. Alexander Schwarz, die mich in verschiedensten Situationen mit wertvollen Ratschlägen unterstützten.

Herrn Biedermann und dem Team der Elektronik-Werkstatt danke ich für die Vermittlung von fachspezifischem Know-how und für die Versorgung mit maßgeschneiderten elektronischen Schaltungen.

Meiner Familie und insbesondere meinem Ehemann Berend Schlenhoff danke ich für den steten Rückhalt und die uneingeschränkte Unterstützung meiner Promotion.